COERCIVITY AND EXCHANGE BIAS STUDY OF POLYCRYSTALLINE HOLLOW NANOPARTICLES

by

Mohamed Alpha Bah

A dissertation submitted to the Faculty of the University of Delaware in partial fulfillment of the requirements for the degree of Doctor of Philosophy in Materials Science and Engineering

Spring 2017

COERCIVITY AND EXCHANGE BIAS STUDY OF POLYCRYSTALLINE HOLLOW NANOPARTICLES

by

Mohamed Alpha Bah

Approved: ____
Darrin Pochan, Ph.D.
Chair of the Department of Materials Science and Engineering

Approved: ____
Babatunde Ogunnaike, Ph.D.
Dean of the College of Engineering

Approved: ____
Ann L. Ardis, Ph.D.
Senior Vice Provost for Graduate and Professional Education

I certify that I have read this dissertation and that in my opinion it meets the academic and professional standard required by the University as a dissertation for the degree of Doctor of Philosophy.

Signed: ____

Syed Ismat Shah, Ph.D.
Professor in charge of dissertation

I certify that I have read this dissertation and that in my opinion it meets the academic and professional standard required by the University as a dissertation for the degree of Doctor of Philosophy.

Signed: ____

Chaoying Ni, Ph.D.
Member of dissertation committee

I certify that I have read this dissertation and that in my opinion it meets the academic and professional standard required by the University as a dissertation for the degree of Doctor of Philosophy.

Signed: ____

Robert Opila, Ph.D.
Member of dissertation committee

I certify that I have read this dissertation and that in my opinion it meets the academic and professional standard required by the University as a dissertation for the degree of Doctor of Philosophy.

Signed: ____

John Xiao, Ph.D.
Member of dissertation committee

ACKNOWLEDGMENTS

First and foremost, I would like to express my sincere gratitude to my advisor Dr. Syed Ismat Shah. He offered me the opportunity to embark on this great journey. Because of him I have learned and gained so much throughout my time as a student.

I would like to acknowledge and thank Dr. Ghulam Hassnain Jaffari, for his friendship and mentorship both academically and personally. I thank him for his guidance, patience, and insight on the many topic discussed throughout my entire PhD process.

I would like to thank my committee members for their support and advisement throughout this process: Dr. Chaoying Ni, Dr. Robert Opila, and Dr. John Xiao.

I would like to thank all current and former members of the Shah group: Dr. Rory Murray, Dr. Inci Ruzbayev, Dr. Nopporn Rujisamphan, Dr. Emre Yassitepe, Zuhal Onuk, Zhiqiang Wang, and John Obamedo. They provided a fun and educational environment to work and learn. Their endless support was crucially in my success during this process.

So many people from the UD community have been critical in helping me achieve this feat, as well. It is difficult to list them all here, but special thanks go to Dr. Fei, Frank, and Dr. Jen Sloppy for microscopy, Robert Schmidt for all magnetic measurement and many other equipment troubleshooting, Jim and John from the electronic shop in Brown lab, Derrick Allen and Tom Reed from the physics machine shop, Jerry Poirier, Kevin Shreve for the countless help with troubleshooting the many systems I had trouble with, Charles Garbini for everything (from safety to ordering parts from McMaster Carr), and the Materials Science and Engineering front office for all the administrative help they provided over the years.

I would also like to take this moment to recognize all of those who have supported and mentored me from high school to now: Dr. Armando Caro, Dean Michael Vaughan, and Mrs. Marianne Johnson, the RISE office and by extension the Office of Academic Advisement and Student Development and Support. I would also like to recognize the Greater Philadelphia Region LSAMP Bridge to the Doctorate program for their financial support at the start of my graduate studies.

I would like to thank the BGSA community for always being there for me in many ways. I was truly blessed to be part of such a wonderful community of friends who support each other every day in this journey. Specifically, I would like to thank Dr. Okechukwu Ogbuu for being a great friend and colleague. Thank you for the countless days and nights of discussion on all topics. I would also like to thank Dr. Ashraf Rabiu-Bah for being a great friend and support.

To Ms. Mahlet Woldeyes, thank you so much for all the support you have offered during this process. Your friendship was truly invaluable.

To my family, to whom I dedicate this thesis, I would like to thank you for your endless sacrifice to make sure I received the best education possible. Your love, support, and advice helped me to get to this point. To all my siblings, you are my inspiration. Thank you for being the great and wonderful people you are.

TABLE OF CONTENTS

Appendix

LIST OF FIGURES

ABSTRACT

Magnetic nanoparticles (NPs) have the potential to be useful in a variety of applications such as biomedical instruments, catalysis, sensing, recording information, etc. These nanoparticles exhibit remarkably different properties compared to their bulk counter parts. Synthesis of magnetic NPs with the right morphology, phase, size and surface functionality, as well as their usage for specific applications are challenging in terms of efficiency and safety. Morphology wise, there have been numerous reports on magnetic nanoparticles where morphologies such as core/shell, hollow, solid, etc., have been explored. It has been shown that morphology affects the magnetic response. Achieving the right crystal structure with required morphology and the magnetic behavior of the nanoparticle phases determines the magnetic response of the structure. For example, in the case of core/shell NPs various ferromagnetic (FM), ferrimagnetic (FiM), and antiferromagnetic (AFM) core and shell combinations have been reported. In these cases, interesting and strikingly different features, such as unusually high spin glass transition temperature, large exchange bias, finite size effects, magnetic proximity effects, unusual trend of blocking temperature as function of average crystal size, etc., have been reported.

More specifically, the morphology of core/shell nanoparticles provides added degrees of freedom compared to conventional solid magnetic nanoparticles, including variations in the size, phase and material of the core and shell of the particle, etc. which helps enhance their magnetic properties. Similar to traditional core/shell nanoparticles, inverted core/shell having a FiM or FM order above the Curie temperature (T_C) of the shell has been reported where the Néel temperature (T_N) is

comparable with the bulk value and there is nonmonotonic dependence of the coercive field (H_C) and exchange bias (H_{EB}) on the core diameter.

In addition to the core/shell morphology, nanoparticles with hollow morphology are also of interest to the scientific community. For such cases, surface spin glass transition enhancements have been reported due to the presence of the additional inner surface. $CoFe_2O_4$, $NiFe_2O_4$ and γ-Fe_2O_3 hollow nanoparticles exhibit strikingly contrasting magnetic behavior compared to bulk and conventional solid particles; similar behavior was also observed in core/shell nanoparticles. Structurally, hollow polycrystalline nanoparticles are composed of multiple crystallographic domains. This random orientation of the crystallographic domains also causes randomization of the local anisotropy axes. Hence the overall effect of this morphology on the magnetic properties is exhibited through the high coercivity, relatively high temperature magnetic irreversibility, lack of magnetic saturation, high blocking temperature, etc.

Over the years, extensive work on core/shell nanoparticles have been carried out to understand their exchange bias phenomenon and the effect on coercivity. Recently, focus has been given to hollow polycrystalline nanoparticles for the reason mentioned above. This thesis investigates the root cause for the above-mentioned effects on the coercivity and exchange bias. Since hollow nanoparticles with polycrystalline structure have shown to exhibit different and improved magnetic behavior compared to bulk and other conventional solid particles, they will be the focus of our investigation. First, extensive field and temperature dependent magnetic study on polycrystalline hollow nickel ferrite ($NiFe_2O_4$) have revealed the effect of the presence of inner surface in a single oxide nanoparticle. Second, the effect of having multiple oxides with different magnetic properties (i.e. FM and AFM) in a single nanoparticle, while maintaining a hollow morphology was investigated by studying polycrystalline hollow γ-Mn_2O_3 and MnO nanoparticles. Studies on various conventional solid manganese oxide nanoparticles have already been reported. Therefore, focus was only made on the fabrication and magnetic study of hollow polycrystalline manganese oxide, with a comparison of the results to those from solid nanoparticles already available in literature. A conclusion was drawn to the importance of the coupling of different magnetic phases (i.e. FM and AFM, FiM and AFM, or SG and AFM), in contrast to just having one single oxide in the hollow nanoparticles. Finally, the importance of this coupling as compared to the increase of surface-to-volume ratio was evaluated in $CoO/Co_3O_4/CoFe_2O_4$ polycrystalline hollow nanoparticles by varying the AFM phase (CoO/Co_3O_4) in the nanoparticles and observing how the magnetic properties varied. This system helped address the effect of the coupling between different magnetic phases, super-exchange interaction, and proximity effect.

Chapter 1

INTRODUCTION

Magnetic nanoparticles (NPs) have the potential to be useful in a variety of applications such as biomedical instruments, catalysis, sensing, recording information, etc. These nanoparticles exhibit remarkably different properties compared to their bulk counter parts [1–9]. Synthesis of magnetic NPs with the right morphology, phase, size and surface functionality, as well as their usage for specific applications are challenging in terms of efficiency and safety. Morphology wise, there have been numerous reports on magnetic nanoparticles where morphologies such as core/shell, hollow, solid, etc., have been explored [10–19]. It has been shown that morphology affects the magnetic response [4,17,20–23]. Achieving the right crystal structure with required morphology and the magnetic behavior of the nanoparticle phases determines the magnetic response of the structure. For example, in the case of core/shell NPs various ferromagnetic (FM), ferrimagnetic (FiM), and antiferromagnetic (AFM) core and shell combinations have been reported [20,24–26]. In these cases, interesting and strikingly different features, such as unusually high spin glass transition temperature [2,24], large exchange bias [9,13,27–29], finite size effects [6,30–33], magnetic proximity effects [24], unusual trend of blocking temperature as function of average crystal size [20,31], etc., have been reported.

More specifically, the morphology of core/shell nanoparticles provides added degrees of freedom compared to conventional solid magnetic nanoparticles, including variations in the size, phase and material of the core and shell of the particle, etc., which helps enhance their magnetic properties [16,24,33–35]. Similar to traditional core/shell nanoparticles, inverted core/shell having a FiM or FM order above the Curie temperature (T_C) of the shell have been reported where the Néel temperature (T_N) is comparable with the bulk value [14,34,36] and there is nonmonotonic dependence of the coercive field (H_C) and exchange bias (H_{EB}) on the core diameter [37].

In addition to the core/shell morphology, nanoparticles with hollow morphology are also of interest to the scientific community. For such cases, surface spin glass transition enhancements have been reported due to the presence of the additional inner surface [8,15,16,20,38–40]. $CoFe_2O_4$, $NiFe_2O_4$ and γ-Fe_2O_3 hollow nanoparticles exhibit strikingly contrasting magnetic behavior compared to bulk and conventional solid particles; similar behavior was also observed in core/shell nanoparticles [8,15,17,39,40]. Structurally, hollow polycrystalline nanoparticles are composed of multiple crystallographic domains. This random orientation of the crystallographic domains also causes randomization of the local anisotropy axes. Hence the overall effect of this morphology on the magnetic properties is exhibited through the high coercivity, relatively high temperature magnetic irreversibility, lack of magnetic saturation, high blocking temperature, etc. [13,17,20,24,31,40].

Over the years, extensive work on core/shell nanoparticles have been carried out to understand their exchange bias phenomenon and the effect on coercivity. Recently, attention has been given to hollow polycrystalline nanoparticles for the reason mentioned above. This thesis investigates the root cause for the above-mentioned effects on the coercivity and exchange bias. Since hollow nanoparticles with polycrystalline structure have shown to exhibit different and improved magnetic behavior compared to bulk and other conventional solid particles, they will be the focus of our investigation. First, extensive field and temperature dependent magnetic study on polycrystalline hollow nickel ferrite ($NiFe_2O_4$) have revealed the effect of the presence of inner surface in a single oxide nanoparticle. Second, the effect of having multiple oxides with different magnetic properties (i.e. FM and AFM) in a single nanoparticle, while maintaining a hollow morphology was investigated by studying polycrystalline hollow γ-Mn_2O_3 and MnO nanoparticles. Studies on various conventional solid manganese oxide nanoparticles have already been reported. Therefore, focus was only on the fabrication and magnetic study of hollow polycrystalline manganese oxide, with a comparison of the results to those from solid nanoparticles already available in the literature. A conclusion was drawn to the importance of the coupling of different magnetic phases (i.e. FM and AFM, FiM and AFM, or SG and AFM), in contrast to just having one single oxide in the hollow nanoparticles. Finally, the importance of this coupling as compared to the increase of surface-to-volume ratio was evaluated in $CoO/Co_3O_4/CoFe_2O_4$ polycrystalline hollow nanoparticles by varying the AFM phase (CoO/Co_3O_4) in the nanoparticles and observing how the magnetic properties varied. This system helped address the effect of the coupling between different magnetic phases, super-exchange interaction, and proximity effect.

How and why these systems were selected to study their respective parameters is addressed in chapter 2. Chapter 2 provides a theoretical explanation of magnetism in nanoparticles, and the influence of different morphologies on the magnetic properties of magnetic nanoparticles. Chapter 2 introduces and expands on the concept of exchange bias. An extensive introduction of the different systems chosen to be studied is also discussed in this chapter. Chapter 3 discusses the growth process for these systems and introduces the different techniques used in the crystallographic, morphological, and magnetic studies of these system. In chapter 4, the first system, $NiFe_2O_4$ nanoparticles, is discussed in detail with extensive field and temperature dependent magnetic study. Evidence of strong coupling between a stabilized disordered surface spins and the ferromagnetic phase is presented as seen high coercivity and exchange bias values at low temperatures. Magnetic irreversibility is shown to persist at low temperatures. The effect of ferrimagnetic and antiferromagnetic coupling, in addition to hollow morphology, is discussed in Chapter 5. In Chapter 5, temperature and cooling field study on the magnetic properties reveals that the strong coupling between the magnetic phases further enhances the magnetic properties of the nanoparticles. Vertical loop shift is reported in this chapter. How exactly the coupling between the two magnetic phases (FM and AFM) in addition to morphology affects the magnetic property is the subject for Chapter 6. In Chapter 6, increasing the cobalt concentration from a 50:50 Co:Fe initial ratio leads to polycrystalline hollow NPs with different concentrations of CoO, Co_3O_4, and $CoFe_2O_4$. Co_3O_4 concentration increases with cobalt concentration. Magnetic studies as a function of cobalt concentration shows increased anisotropy constant in low magnetic field, decreased magnetization in both the low and high magnetization curves, decrease in irreversibility and blocking temperature, decrease in coercivity, however, a nonmonotonic relation exist for exchange bias. A brief summary and future recommendations are provided in chapter 7.

REFERENCES

[1] A.-H. Lu, E.L. Salabas, F. Schüth, Magnetic nanoparticles: synthesis, protection, functionalization, and application, Angew. Chem. Int. Ed. Engl. 46 (2007) 1222–44. doi:10.1002/anie.200602866.

[2] R.H. Kodama, A.E. Berkowitz, E.J. McNiff, Jr., S. Foner, Surface Spin Disorder in NiFe2O4 Nanoparticles, Phys. Rev. Lett. 77 (1996) 394–397. doi:10.1103/PhysRevLett.77.394.

[3] M. Estrader, A. López-Ortega, S. Estradé, I. V Golosovsky, G. Salazar-Alvarez, M. Vasilakaki, et al., Robust antiferromagnetic coupling in hard-soft bi-magnetic core/shell nanoparticles., Nat. Commun. 4 (2013) 2960. doi:10.1038/ncomms3960.

[4] M. Estrader, A. López-Ortega, I. V. Golosovsky, S. Estradé, A. G. Roca, G. Salazar-Alvarez, L. López-Conesa, D. Tobia, E. Winkler, J. D. Ardisson, W. A. A. Macedo, A. Morphis, M. Vasilakaki, K. N. Trohidou, A. Gukasov, I. Mirebeau, O. L. Makarova, R. D. Zysler, F. Peiró, M. D. Baró, L. Bergström, J. Nogués, Origin of the large dispersion of magnetic properties in nanostructured oxides: FexO/Fe3O4 nanoparticles as a case study., Nanoscale. 7 (2015). doi:10.1039/c4nr06351a.

[5] P. Ayyub, M. Multani, M. Barma, Size-induced structural phase transitions and hyperfine properties of microcrystalline Fe2O3, J. Phys. C …. 21 (1988) 2229–2245. http://iopscience.iop.org/0022-3719/21/11/014 (accessed March 12, 2015).

[6] F. T. Parker, M. W. Foster, D. T. Margulies, A. E. Berkowitz, Spin canting, surface magnetization, and finite-size effects in γ-Fe2O3 particles, Phys. Rev. B. (1993). doi:10.1103/PhysRevB.47.7885.

[7] T. Theivasanthi, M. Alagar, Anti-bacterial Studies of Silver Nanoparticles, Arxiv Prepr. arXiv1110.1372. (2011). http://arxiv.org/abs/1110.1372 (accessed July 3, 2012).

[8] G.H. Jaffari, A. Ceylan, C. Ni, S. I. Shah, Enhancement of surface spin disorder in hollow NiFe2O4 nanoparticles, J. Appl. Phys. 107 (2010) 13910. doi:10.1063/1.3277041.

[9] V. Skumryev, S. Stoyanov, Y. Zhang, Beating the superparamagnetic limit with exchange bias, Nature. 423 (2003) 19–22. doi:10.1038/nature01750.1.

[10] H. Zeng, J. Li, Z.L. Wang, J.P. Liu, S. Sun, Bimagnetic Core / Shell FePt / Fe3O4 Nanoparticles, (2004) 3–6.

[11] A. H. Habib, C. L. Ondeck, P. Chaudhary, M. R. Bockstaller, M. E. McHenry, Evaluation of iron-cobalt/ferrite core-shell nanoparticles for cancer thermotherapy, J. Appl. Phys. 103 (2008) 07A307. doi:10.1063/1.2830975.

[12] J. M. Soares, O. L. A. Conceição, F. L. A. Machado, A. Prakash, S. Radha, A. K. Nigam, Magnetic couplings in CoFe2O4/FeCo–FeO core–shell nanoparticles, J. Magn. Magn. Mater. 374 (2015) 192–196.

doi:10.1016/j.jmmm.2014.08.015.
[13] C. Liu, J. Cui, X. He, H. Shi, Large exchange bias with remarkable thermostability in an inverted quasi core/shell CoO/γ-Fe2O3 granular system, J. Nanoparticle Res. 16 (2014) 2320. doi:10.1007/s11051-014-2320-7.
[14] G. Salazar-Alvarez, J. Sort, S. Suriñach, M. D. Baró, J. Nogués, Synthesis and size-dependent exchange bias in inverted core-shell MnO|Mn3O4 nanoparticles., J. Am. Chem. Soc. 129 (2007) 9102–8. doi:10.1021/ja0714282.
[15] Z. Nemati, H. Khurshid, J. Alonso, M. H. Phan, P. Mukherjee, H. Srikanth, From core/shell to hollow Fe/ γ-Fe2O3 nanoparticles: evolution of the magnetic behavior, Nanotechnology. 26 (2015) 405705. doi:10.1088/0957-4484/26/40/405705.
[16] A. Cabot, A. Alivisatos, V. Puntes, L. Balcells, Ò. Iglesias, A. Labarta, Magnetic domains and surface effects in hollow maghemite nanoparticles, Phys. Rev. B. 79 (2009) 94419. doi:10.1103/PhysRevB.79.094419.
[17] G. H. Jaffari, A. Ceylan, H. P. Bui, T. P. Beebe, S. Ozcan, S. I. Shah, Non-equilibrium cation distribution and enhanced spin disorder in hollow CoFe2O4 nanoparticles., J. Phys. Condens. Matter. 24 (2012) 336004. doi:10.1088/0953-8984/24/33/336004.
[18] M. S. Seehra, A. Punnoose, Particle size dependence of exchange-bias and coercivity in CuO nanoparticles, Solid State Commun. 128 (2003) 299–302. doi:10.1016/j.ssc.2003.08.029.
[19] L. Zhao, H. Zhang, Y. Xing, S. Song, S. Yu, W. Shi, X. Guo, J. Yang, Y. Lei, F. Cao, Studies on the magnetism of cobalt ferrite nanocrystals synthesized by hydrothermal method, J. Solid State Chem. 181 (2008) 245–252. doi:10.1016/j.jssc.2007.10.034.
[20] G. Hassnain Jaffari, S. Rizwan Ali, S.K. Hasanain, G. Güntherodt, S. Ismat Shah, Stabilization of surface spin glass behavior in core-shell Fe67Co33/CoFe2O4 nanoparticles, J. Appl. Phys. 108 (2010) 63921. doi:10.1063/1.3478738.
[21] A. Ceylan, C. C. Baker, S. K. Hasanain, S. Ismat Shah, Effect of particle size on the magnetic properties of core-shell structured nanoparticles, J. Appl. Phys. 100 (2006) 34301. doi:10.1063/1.2219691.
[22] Z. H. Wang, D. Y. Geng, Y. J. Zhang, Z. D. Zhang, Morphology, structure and magnetic properties of single-crystal Mn3O4 nanorods, J. Cryst. Growth. 310 (2008) 4148–4151. doi:10.1016/j.jcrysgro.2008.06.025.
[23] J. M. Soares, V. B. Galdino, O. L. A. Conceição, M. A. Morales, J. H. de Araújo, F. L. A. Machado, Critical dimension for magnetic exchange-spring coupled core/shell CoFe2O4/CoFe2 nanoparticles, J. Magn. Magn. Mater. 326 (2013) 81–84. doi:10.1016/j.jmmm.2012.08.040.
[24] I. Golosovsky, G. Salazar-Alvarez, A. López-Ortega, M. González, J. Sort, M. Estrader, S. Suriñach, M. Baró, J. Nogués, Magnetic Proximity Effect Features in Antiferromagnetic/Ferrimagnetic Core-Shell Nanoparticles, Phys. Rev. Lett. 102 (2009) 247201. doi:10.1103/PhysRevLett.102.247201.

[25] M. Y. Khan, C. B. Wu, W. Kuch, Pinned magnetic moments in exchange bias: Role of the antiferromagnetic bulk spin structure, Phys. Rev. B. 89 (2014) 94427. doi:10.1103/PhysRevB.89.094427.
[26] J.A. González, J.P. Andrés, J.A. De Toro, P. Muñiz, T. Muñoz, O. Crisan, C. Binns, J. M. Riveiro, Co–CoO nanoparticles prepared by reactive gas-phase aggregation, J. Nanoparticle Res. 11 (2009) 2105–2111. doi:10.1007/s11051-008-9576-8.
[27] P. Z. Si, D. Li, J. W. Lee, C. J. Choi, Z.D. Zhang, D. Y. Geng, E. Brück, Unconventional exchange bias in oxide-coated manganese nanoparticles, Appl. Phys. Lett. 87 (2005) 133122. doi:10.1063/1.2072807.
[28] M. Kiwi, J. Mejia-Lopez, R. D. Portugal, R. Ramirez, Exchange bias theory: The role of interface structure and of domains in the ferromagnet, Phys. LOW Dimens. Syst., 2001: pp. 295–300. doi:0-306-46566-3.
[29] D. De, Ò. Iglesias, S. Majumdar, S. Giri, Probing core and shell contributions to exchange bias in Co/Co3O4 nanoparticles of controlled size, Phys. Rev. B. 94 (2016) 184410. doi:10.1103/PhysRevB.94.184410.
[30] X. Batlle, A. Labarta, Finite-size effects in fine particles: magnetic and transport properties, J. Phys. D. Appl. Phys. 35 (2002) R15–R42. doi:10.1088/0022-3727/35/6/201.
[31] R. J. Tackett, A.W. Bhuiya, C. E. Botez, Dynamic susceptibility evidence of surface spin freezing in ultrafine NiFe2O4 nanoparticles., Nanotechnology. 20 (2009). doi:10.1088/0957-4484/20/44/445705.
[32] H. Ahmadvand, S. R. Safdari, A. Nozad Golikand, P. Dasgupta, A. Poddar, H. Salamati, Exchange bias in Co/CoO/Co3O4 nanostructures, J. Magn. Magn. Mater. 377 (2015) 19–23. doi:10.1016/j.jmmm.2014.10.021.
[33] J. Nogués, J. Sort, V. Langlais, V. Skumryev, S. Suriñach, J.S. Muñoz, M. D. Baró, Exchange bias in nanostructures, Phys. Rep. 422 (2005) 65–117. doi:10.1016/j.physrep.2005.08.004.
[34] A. Berkowitz, G. Rodriguez, J. Hong, K. An, T. Hyeon, N. Agarwal, D. Smith, E. Fullerton, Antiferromagnetic MnO nanoparticles with ferrimagnetic Mn3O4 shells: Doubly inverted core-shell system, Phys. Rev. B. 77 (2008) 24403. doi:10.1103/PhysRevB.77.024403.
[35] A. E. Berkowitz, G. F. Rodriguez, J. I. Hong, K. An, T. Hyeon, N. Agarwal, D. Smith, E. Fullerton, Monodispersed MnO nanoparticles with epitaxial Mn3O4 shells, J. Phys. D. Appl. Phys. 41 (2008) 134007. doi:10.1088/0022-3727/41/13/134007.
[36] J. Sort, S. Suriñach, J. Muñoz, M. Baró, J. Nogués, G. Chouteau, V. Skumryev, G. Hadjipanayis, Improving the energy product of hard magnetic materials, Phys. Rev. B. 65 (2002) 174420. doi:10.1103/PhysRevB.65.174420.
[37] A. López-Ortega, D. Tobia, E. Winkler, I. V Golosovsky, G. Salazar-Alvarez, S. Estradé, M. Estrader, J. Sort, M. A. González, S. Suriñach, J. Arbiol, F. Peiró, R. Zysler, M. D. Baró, J. Nogués, Size-dependent passivation shell and magnetic properties in antiferromagnetic/ferrimagnetic core/shell MnO

nanoparticles, J. Am. Chem. Soc. 132 (2010) 9398–407. doi:10.1021/ja1021798.
[38] G. Hassnain Jaffari, H.-Y. Lin, C. Ni, S. Ismat Shah, Physiochemical phase transformations in Co/CoO nanoparticles prepared by inert gas Condensation, Mater. Sci. Eng. B. 164 (2009) 23–29. doi:10.1016/j.mseb.2009.06.007.
[39] H. Khurshid, P. Lampen-Kelley, Ò. Iglesias, J. Alonso, M.-H. Phan, C.-J. Sun, M.-L Saboungi, H. Srikanth, Spin-glass-like freezing of inner and outer surface layers in hollow γ-Fe2O3 nanoparticles., Sci. Rep. 5 (2015) 15054. doi:10.1038/srep15054.
[40] H. Khurshid, W. Li, M.H. Phan, P. Mukherjee, G. C. Hadjipanayis, H. Srikanth, Surface spin disorder and exchange-bias in hollow maghemite nanoparticles, Appl. Phys. Lett. 101 (2012) 1–6. doi:10.1063/1.4733621.

Chapter 2

BACKGROUND

2.1 Magnetism in Nanoparticles

Origin of all interesting phenomena exhibited by magnetic nanoparticles (NPs) can be explained in terms of their intrinsic properties such as crystal structure, size distribution, finite-size effects and the inter/intra particle interactions [1]. Out of these, the magnetic behavior of individual NPs is mainly dominated by the finite-size effects and is a size dependent property. Since the size of the NPs are proportional to their anisotropy energy [1], most studies of finite-size effects have been in superparamagnetic regime. In NPs, surface gives rise to magnetic disorder with behavior that ranges from that of a dead magnetic layer to that of a spin-glass (SG) like layer [1]. The competition between the core and this disordered layer greatly impacts the magnetic response of NPs. Around the ferromagnetic (FM) and superparamagnetic (SPM) transition, it has been observed that there exists field irreversibility, high saturation fields, extra anisotropy contribution, and shifted loops after field cooling (FC) processes [1]. These contrasting differences from bulk materials have been attributed to a coupling between different behavior of spins at the core and the surface of the NPs. It is known that surface brings about defects, which break the atomic coordination of the core and surface, resulting in a more disorder spin orientation at the surface.

2.1.1 Superparamagnetic regime

We first start our discussion by explaining effect of size on magnetization. In bulk systems, it is known that domains sizes, which are not uniform and are distributed throughout the bulk material and is limited by domain walls (DWs). Reduction of the magnetic NPs below average domain size leads to formation of single domain NPs. The exchange energy, magnetostatic and anisotropy energies of the overall system are all optimized as the size of the system is reduced [1]. At a certain size limit, the function that governs the size distribution inside the magnetic system becomes narrow and is approximated by the ratio of the domain wall energy per unit area over the square of the saturation magnetization [1]. At this size limit, the system is a single domain system.

The magnetic energy that govern the system has been given by the Stoner-Wohlfarth model, equation 2.1. This model assumes non-interacting magnetic nanoparticles, where the particles are in thermal equilibrium and the total energy is minimized by orientation of spins toward the easy axis. The minimized energy along the easy axis is the anisotropy energy, which depends on the volume (V) of the particles and the angle (θ) between the anisotropy axis and magnetization, the applied magnetic field (H), the spontaneous magnetization (M_S), and the angle between H and the easy axis (Φ) is the angle between the applied field and the easy axis.

$$E = KV\sin^2\theta + HM_S\cos(\theta - \phi) \tag{2.1}$$

It follows from this equation that as V of the system decreases so does the energy of the system; and the system follows H more readily. Overall the anisotropy energy of the system is lower for materials with lower anisotropy constants (K), and these materials have smaller energy barriers (ΔE). ΔE depends on H as well as KV and is a function of θ and ϕ [2]. ΔE determines the spins orientation preference for ferromagnetic (FM) materials. It takes more energy to reorder spins of FM materials at an angle other than their easy axis. For NPs, thermal effects (k_BT), also disturbs the alignment of the spins. For systems with small K, the spins behave like paramagnetic systems with saturation, SPM. At this size regime, increase in T leads k_BT to be comparable to ΔE. The equilibrium temperature is known as the blocking temperature (T_B). T_B is defined below, where v_o is the attempt frequency and v the measured frequency.

$$T_B = \frac{\Delta E}{k_B \ln\left({}^{v_o}/_{v}\right)} \tag{2.2}$$

At temperatures above T_B, thermal excitation leads to rapid fluctuations of spins as compared to observation time. This time dependent phenomenon was first introduced by Néel where he assumed that particle spins are rigidly coupled and reverse as a whole [1]. The characteristic time (τ) was given by equation 2.3, and is proportional to the Boltzmann constant (k_B). In equation 2.3, $\tau_0$is the attempt timescale and is in the order of 10-12 sec. This suggest that experimental time plays a role when investigating systems close to their SPM state, and the temperature at which the investigation is done.

$$\tau = \tau_0 \exp\left(-\frac{KV}{k_B T}\right) \tag{2.3}$$

For instance, moments of a single domain particle remain blocked for an experiment with a characteristic time window much shorter than τ at a fixed temperature. In fact, a critical volume (V_{SP}) for SPM behavior for a 100 s experimental time and considering τ_0 to be 10^{-9} s is given as:

$$V_{sp} = 25kT/K \tag{2.4}$$

An applied field will modify equation 2.4 and give equation 2.5, where it can be observed that the applied field leads to a lower energy barrier, which shift T_B to lower temperatures.

$$25k_B T = KV\left(1 - \frac{H_C M_S}{2K}\right)^2 \tag{2.5}$$

The coercivity (H_C) of single domain particles in this size regime can be obtained by rearranging equation 2.5. The lack of domain walls in single domain particles mean that the magnetization reversal occurs by the rotation of the entire spin structure. However, in multidomain particles domain wall motion dictate the magnetic reversal. Therefore, the coercivity of single domain particles are larger compared to multidomain particles, which is depicted in figure 2-1. In the single domain region of small non-interacting particles, where H_C is highest, the rotation of the magnetization happens coherently.

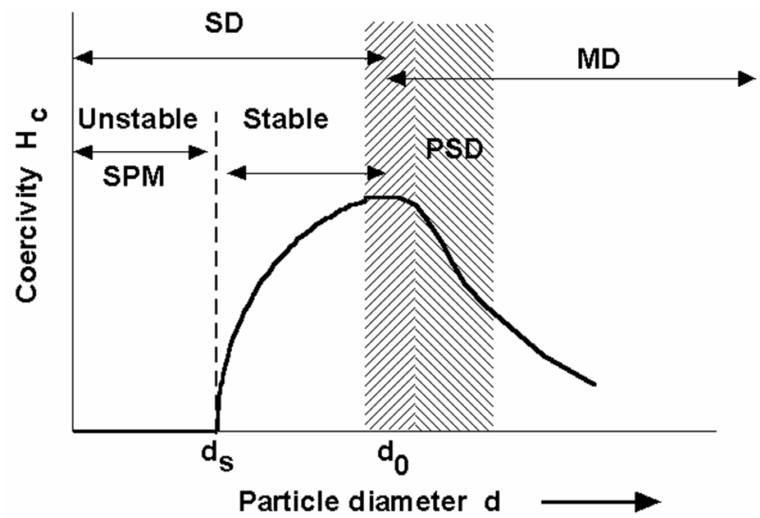

Figure 2-1 : Size dependence of coercivity. SD: Single Domain, MD: Multi-Domain, SPM superparamagnetic, PSD: Pseudo Single Domain [3]

2.1.2 Surface and finite size effects

Particle interaction plays a substantial role in the overall magnetization of NPs assemblies [1,3]. Of the different interactions that exist in finite particles, dipole-dipole interaction is the most obvious since it always exists; other interactions to be considered include exchange interactions of NPs in close proximity, and exchange interactions of NPs through different mediums. Interactions through different mediums are called super exchange interactions, since magnetic NPs interact with one another through an insulating matrix.

The effect on the overall magnetization of NPs assemblies from interactions has been reported both experimentally [4–8] and theoretically[7–9]. Shtrikmann and Wohlfarth updated the Néel-Brown model to reflect weak interactions [9]; whereas Dormann *et al.* subsequently updated it for a more general system [10]. In the experimental model by Dormann *et al.*, it was observed that T_B increased with increasing strength of the dipole interactions [1]. However, Morup and Tronc have predicted that there is an opposite correlation to T_B with increasing dipole interactions in the case for weak interactions, which they confirmed by Mossbauer spectroscopy on γ-Fe_2O_3 NPs [12]. Therefore, they suggested that in fine particle, T_B affects the magnetic regime in two different ways at high temperatures – T_B decreases with increased interactions for weak interaction but increases with increased interaction for strong interaction. In the latter case, the response of T_B can be attributed to the freezing process, therefore increases with increasing interactions, where spins are more readily affected by nearby spins and therefore are not *un*-blocked easily [1,5].

This ensemble movement of spins in the glassy state are characterized as the ageing effect in memory. Although ageing effects have been observed in other ensembled glassy systems, where a true phase transition is not observation as is the case in the situation described above with spins going from a blocked state to a none-frozen state [13]. This has been explained by looking at the strong temperature dependence in the case of the collective state, as well as the fact that non-finite particle tend to be blocked in all time scales and therefore not taking part in the collective state of the system [1]. Zero field cooled (ZFC) and field cooled (FC) magnetization versus temperature studies show that non-finite sized particle have a higher T_B [14,15]. It has been revealed, also, that SG is highly dependent on the applied external magnetic field [13,16–18].

The complexity to the magnetic properties of NPs systems is further enhanced when surface effects are considered, which one must consider in this size limit since surface increase significantly as the volume of the NPs is reduced. Enhancement of the magnetic properties is not straightforward to understand since surface effects and finite-size effects are mixed and can be in competition to the overall magnetic properties since surface results in more defects. Therefore, it is worth defining both effects – finite size effects is the effect that comes from the cut off of the characteristic length since the volume of the particles are being restricted; surface effects comes from the broken bonds and defects that comes due to these broken bonds resulting in surface spins disorder and frustration [1].

The result of surface spins disorder and frustration is the effect on the structural relaxation of spins, and creation of strains. Strains have been known to induce additional anisotropy, as is the case of lattice mismatching in lattice constants at the interface between thin-films and substrate. However, this effect has been found to be negligible in NPs. Therefore, focus is only given to two other type of anisotropy that prevalent in NPs, e.g. bulk anisotropy and surface anisotropy. Bulk anisotropy (K_b) refers to the core of the NPs; whereas, surface anisotropy (K_s) considers limit where surface effect is prevalent inside the NPs. The resulting anisotropy constant is termed as effective anisotropy (K_{eff}) and is given by equation 2.6. Where, d is the diameter of the NPs. Therefore, one can observe that the surface effect increase with decreasing particle size.

$$K_{eff} = K_b + \frac{6}{d} K_s \tag{2.6}$$

Similarly, on how surface affect the overall anisotropy in NPs, experimental observation has been made on their effect on M_S. In NPs, it has been observed that M_S decreases as a function of particle size. Coey et al in 1971, while studying γ -

Fe_2O_3 ferrimagnetic NPs, found reduction in M_S, and attributed the reduction to random canting of surface spins [19]. Their claim has been subsequently verified by many other studies for different oxides by employing different techniques to measure M_S, namely Mossbauer spectroscopy [20–22], polarized [23] and inelastic [24] neutron scattering, and FM resonance [25]. In contrast to the observation of spin canting in oxides, none has been found in metallic FM NPs, thereby supporting the claim that the competition of the frustrated antiferromagnetic (AFM) interactions is to be credit with the origin of spin misalignment [1].

High field irreversibility has been observed at low temperature, 4.2 K, for both FM and AFM NPs, as well as lack of saturation of hysteresis loops [26–28]. Therefore, suggesting that spin canting is indeed prevalent in this size limit, since anisotropy energies alone cannot be responsible of the blocking at very high fields. Other than very high field irreversibility at low temperature, a shift of the loop is observed after FC, as well as irreversibility between FC and ZFC loops [26,28,29]. The loop shifts are, however, seen to decrease with increase in temperature until completely vanishing [26,28,30]. Actually, all the properties that have been mentioned so far to be effected by this size reduction are seen to vanish at a certain temperature, given as spin freezing temperature (T_f) [1]. Therefore, a model representing a magnetically ordered core surrounded by a surface layer of canted spins has been proposed [1,27,28]. In this model, the layer surrounding the core, which has broken bonds and canted spins has been referred to as a SG surface, when at a $T < T_f$ creates an exchange coupling field on the core of the NPs. This coupling results in a shift of magnetic loop. One of the characteristic of this coupling is its field dependence on T_f, $\delta T_f \propto H^{2/3}$ [1]. Kodama and Berkowitz have produced model and studies, and concluded that the non-saturation of the hysteresis loop comes from the shell (SG layer), surface anisotropy [22,30,31].

2.1.3 Exchange Bias

The shift of the hysteresis loop, from the exchange coupling of core and the SG layer, has been referred to as exchange bias (EB). EB therefore manifest itself as a source of anisotropy. This added source anisotropy makes EB a very important to the information storage industry, where high information storage capacity in small areas requires small particle size. EB has been extensively investigated since Meiklejohn and Bean discovered it while working on a Co/CoO system in 1956 [32]. In many models [33–38], EB has been investigated for magnetic NPs. However, the origin of EB is still not well understood to date but has been attributed to the interaction between the coupling at the interface of FM and AFM phases. A schematic of this coupling and how it affects the behavior of hysteresis loop is shown figure 2-2, below. Figure 2-2 shows the different steps involved during EB, mainly how the coupling between the two different magnetic phases leads to the shift of the hysteresis loop.

In figure 2-2, showing a bilayer film, where the bottom (dark grey) layer is FM and the top layer (light grey) is AFM. Here, multiples steps are noted. First, the hysteresis loop is shown when recorded at a temperature above the Néel temperature (T_N) but below the Curie temperature (T_C). The resulting loop is observed to be centered and symmetric. In this temperature regime, the AFM layer plays no role and is in PM state, and the magnetic response solely comes from the FM layer. After cooling the layer below T_N while applying a field, the FM spins get aligned along with the field. Then, if a hysteresis loop is recorded, the resulting loop is observed to be shifted to the left.

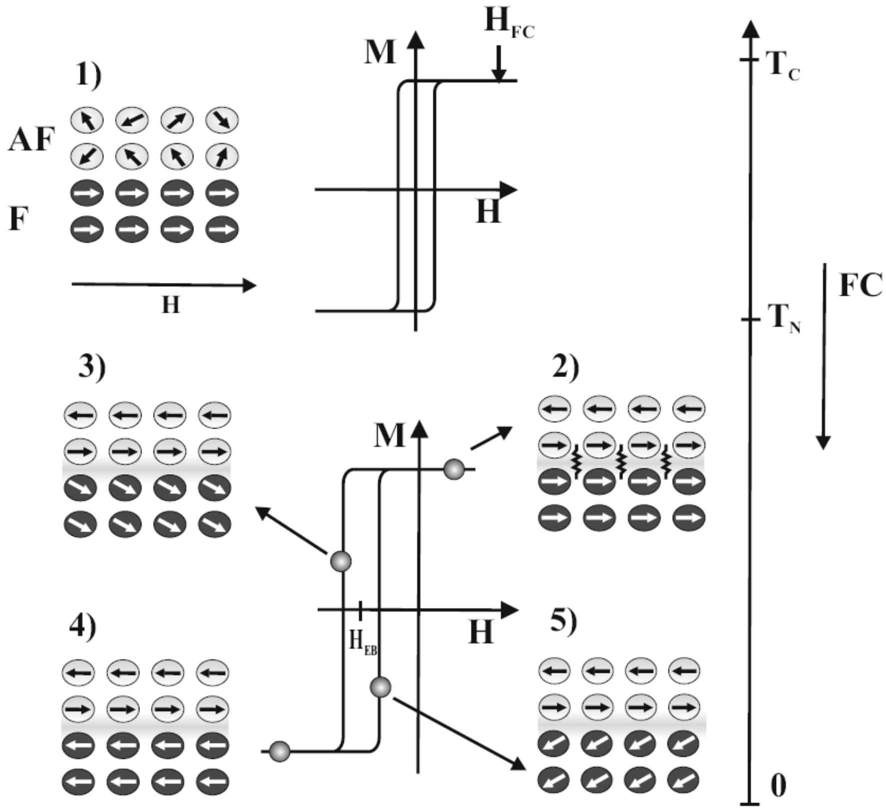

Figure 2-2: Schematic description of exchange bias for an FM/AFM bilayer [39]

The shift arises due to the torque experienced from the FM spins interacting with AFM spins at the interface when the FM spins are to be aligned in the manner shown in part 2) of figure 2-2. Here, FM spins encounter some resistance from spins of the AFM layer right next to them. To overcome this force, a larger field is required and the curve crosses the x-axis at H_{C^-}. H_{C^-} is the coercivity field (H_C) needed in the negative field direction to overcome the microscopic torque. Furthermore, the field dependence from the unidirectional anisotropy, where less field is required to flip the spins along the direction of the positive (easy axis), leads the hysteresis loop to shift.

The curve crosses the x-axis at H_{C^+}. Therefore, EB can be mathematically calculated from the difference of the H_C in the negative and positive direction, $EB = \frac{H_{C^-} - H_{C^+}}{2}$. Again, this illustration is a simple model to help visualize the hysteresis shift in a bilayer FM/AFM thin film. It does not however explain the interface structure of the system, the interface magnetic coupling direction, cooling field intensity dependence, H_C, nor the enhancement of the shift.

Meiklejohn calculated the rotational hysteresis, energy, and loss at the interface of the proposed bilayer, where it was assumed that there's a single domain AFM that is weakly coupled to a single domain FM layer. In his calculation, Meiklejohn assumed, using a vector model, that the anisotropy constant of the AFM layer is much greater than that of the FM layer. The resulting expression is given:

$$EB = \frac{J_{F/AF}}{a^2 M_F t_F} \tag{2.7}$$

In equation 2.7, $J_{F/AF}$ is the interfacial exchange constant, a the lattice parameter, M_F the FM saturation magnetization, and t_F the thickness of FM layer. The values of EB obtained from this model were found to be significantly different than experimental values. The difference in the experimental values and those from this model comes from the assumption mentioned above and lack of consideration of the important structural parameters.

Many models, since, have been developed to better reflect experimental values of the bilayer thin films, with each new model getting better at approximating experimental values. Nèel considered a weakly anisotropic uncompensated AFM interface layer that is ferromagnetically coupled to a FM layer [34], assuming that the magnetization in both the FM and AFM layer was uniform within the layer parallel to the interface [40]. A model proposed by Malozemoff significantly improved the estimation of the EB. In his model, which is based on randomness in the exchange interactions at the FM/AFM, Malozemoff decreased the EB by a factor of $2a / \sqrt(A / K)$, where A is the exchange stiffness [36,40]. This model still falls short since there's no consideration of the defects in the film, which is unrealistic. A model that has been successful at predicting the EB of FM/AFM systems such as Ni/NiO and Co/CoO systems was proposed by Mauri et al. However, this models fails to explain other systems such as EB that requires AFM coupling of the interface spins, including systems where large EB are observed in the compensated interfaces rather than the uncompensated ones [40]. In their model, Mauri et al. assumed an infinitely thick AFM layer and a restricted FM layer that is still a single domain [41]. Systems with large anisotropy constant of the AFM layer have been considered by Kiwi et al., where they also considered unfavorable domain walls. This model introduced the idea of frozen interfaces was introduced, with the first layer of the AFM layer freezes into displaced spins (canted spins) configuration [42,43]. By introducing defects in the AFM layer, Nowak et al. proposed a model where domain states are formed in the AFM layer. They argue that dilution in the AFM layer promote the formation domain state by causing domain wall formation through nonmagnetic sites. Their model have been consistent in predicting experimental results, when exploring EB as a function of AFM thickness and temperature [40].

Experiments such as creation of defects in Co/CoO by introducing nonmagnetic Mg or by oxidation of the AFM layer has supported models by Nowak et al. mentioned above [40]. In the experiments, FM/AFM interface, interface coupling direction, layer thickness (t_{AF}), temperature dependence etc. effect on EB were investigated. These experiments found that domain formation in the AFM layer led to the enhancement of EB by a factor of 3 or 4 [40]. Vertical shift of the hysteresis loop was also reported in these experiments due to excess magnetization from the domain formation in the AFM layer [40]. Pinned spins that do not follow external field yield a shift to the hysteresis loop along the magnetization axis. Noguès et al. first reported this shift in FeF_2/Fe and MnF_2/Fe systems [44]. They attributed the direction of the loop shift to the structure of the layer in small cooling fields (H_{CF}) but shifts upward in the case of large H_{CF}. Downward shift is attributed to AFM coupling at the interface, while FM coupling results in an upward shift. This suggested the existence of a correlation between positive EB and the nature of the FM/AFM coupling. Investigating t_{AF} revealed that too thin of a FM layer leads to no EB, believed to be caused by the broken continuity in the layer [40]. EB was also observed to reduce when domain states are increases in the AFM layer, which can be explained by the suppression of the AFM order when domain state increases. As far as temperature effect, EB has been found to vanish above T_B [40].

In thin films $T_{B,}$ has been shown to vary with the grain size of the AFM layer. These later models developed for the magnetic bilayer were found to be very similar to the models, already discussed above, for magnetic NPs, with notable difference. In magnetic NPs, no saturation of the hysteresis loop is observed. Also, the increase in surface of NPs greatly affect its EB, the reversal of the particle moment is strongly influenced by the reduced atomic coordination and disorder at the surface. And since there are more atoms at the surface of NPs, it is easy to see that EB and many other magnetic properties are enhanced compared to thin films of the same materials [1,40].

In addition to the already cited work above, many other studies have been done on magnetic NPs to investigate how finite-size, interaction, and surface effects affect their basic properties, including enhanced and tailored properties for specific applications [1,45–50]. Morphologies such as core/shell structures [51–57] and hollow NPs [58–61] are among those investigated for the influence that both morphology and interactions have on the basic properties of magnetic NPs. However, no work has been systematically done to help address how exactly these different parameters comes together and influence these parameters, which is the focus of this thesis. In this thesis, materials will be selected appropriately to investigate these effects: polycrystalline hollow single oxide, $NiFe_2O_4$, will be used to study effect of surface; bi-magnetic (FiM and AFM) polycrystalline hollow NPs, γ-Mn_2O_3 and MnO, will be used to study the combined effect of morphology and interaction on the magnetic properties; and finally, effect of magnetic phase interaction will be studied for bi-magnetic polycrystalline hollow NPs, Co_2O_3 and $CoFe_2O_4$, by changing the ratio of FM to AFM phase.

2.2 Materials Selection

2.2.1 Nickel iron oxide

Nickel iron oxide ($NiFe_2O_4$) has a spinel structure, precisely an inverted spinel structure [2,40,62]. A Spinel is defined as a structure that is made of a face centered cubic (fcc) unit cell of 32 oxygen anions surrounded by 96 interstitials metallic cations in the manner of AB_2O_4. In AB_2O_4, A and B are divalent (A^{2+}) and trivalent (B^{3+})

cations, respectively. In this structure, the divalent cations accounts for 64 interstitials, in a tetrahedral structure, while the trivalent cations account for the other 32 interstitials sites, in an octahedral the structure. Figure 2-3 shows a schematic of such a structure. $NiFe_2O_4$ has the inverted structure of $[B]_X[AB]_YO_4$, where X and Y represent tetrahedral and octahedral sites, respectively. Here, Ni^{2+} occupy octahedral sites, and Fe^{3+} are equally distributed between the octahedral and tetrahedral sites of the oxygen anions [62].

In the compact unit cell of $NiFe_2O_4$, with a lattice constant a = 8.35 Å, there are 56 atoms, among which 24 atoms are magnetic transition metals. The exchange interaction among the magnetic atoms yield a ferrimagnetic structure, with a moment measure to be between 1.5 to 2.4 μ_B. In said interaction, there's a negative interaction between A and B sites, and the oxygen atoms are linked to three metallic cations, in an octahedral structure, and to one metallic cation in the tetrahedral site, shown in figure 2-4.

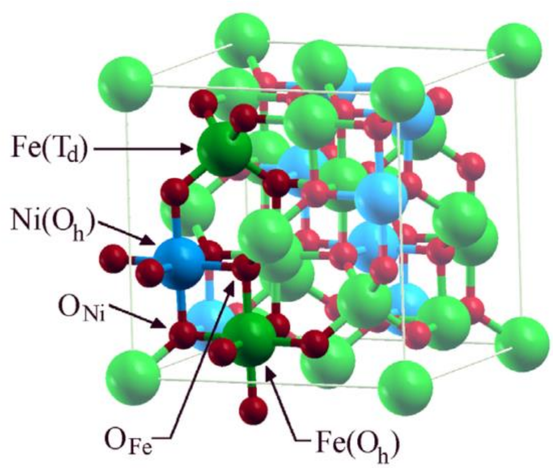

Figure 2-3: $NiFe_2O_4$ spinel unit cell, with blue spheres representing nickel atoms, while green and red spheres represents iron atoms and oxygen atoms, respectively [62].

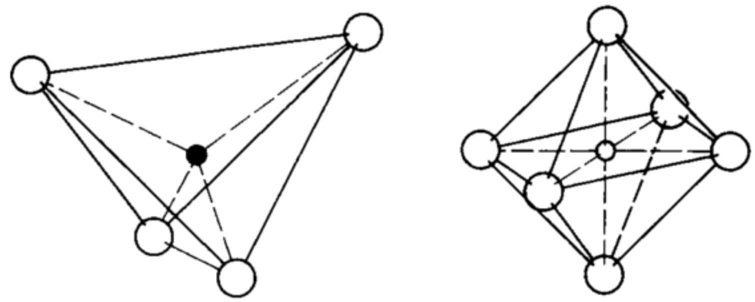

Figure 2-4: Depiction of the oxygen position in the tetrahedral and octahedral sub-lattices for a spinel structure, with the dark small ball representing cations in the tetrahedral sites, non-shaded small spheres representing cations in the octahedral sites, and the non-shaded big spheres representing the oxygen anions [2].

2.2.2 Manganese oxide

Manganese can have three different cations, Mn^{2+}, Mn^{3+}, and Mn^{4+}, which means that it can form many different oxides. There are four stable oxides with many metastable mixed states (e.g. MnO, Mn_2O_3, Mn_3O_4, and MnO_2) [63,64]. All the stable oxides of manganese occur naturally [63]. Two of the stable oxide of manganese list, MnO and MnO_2, have cubic structures, while the other two, Mn_2O_3 and Mn_3O_4, have a spinel structure. In MnO, Mn^{2+} and O^{2-} ions are found at the lattice sites, where they make a rocksalt structure, shown in figure 2-5. In figure 2-5, the oxygen ions are represented by grey spheres, while the white sphere represent the manganese ions. MnO lattice constant is 4.44 Å, which each unit cell containing four manganese and oxygen atoms. MnO_2, on the other, has a simple tetragonal rutile structure and is shown in figure 2-6, with its lattice parameters being, a = b = 4.4 Å and c = 2.87 Å [63]. In figure 2-6, the dark grey sphere represents the oxygen ions, and light grey spheres representing the manganese ions [65]. In figure 2-6, manganese atoms are surrounded by six oxygen ions in a tetrahedral structure, and vice-versa. Mn_2O_3 is a naturally occurring stable compound with two different polymorphs, α-Mn_2O_3 or α-kurnakite and β-Mn_2O_3 or β-kurnakite/bixbyite. β-Mn_2O_3 being the one found naturally. Similarly, Mn_3O_4, β-Mn_3O_4 is the naturally occurring polymorph of Mn_3O_4, also known as hausmannite. The main difference between Mn_2O_3 and Mn_3O_4 is that Mn_3O_4 has a distorted spinel structure at ambient temperature [65]. In figure 2-7, an illustration of the $Mn^{2+}[Mn_2^{3+}]O_4^{2-}$ structure is shown, with the Mn^{2+} cations occupying the tetrahedral sites and the Mn^{3+} the octahedral sites. In figure 2-7, the oxygen ions are represented by the large white spheres, the Mn^{3+} by the darker grey shaded spheres, and the Mn^{2+} by the lighter grey shaded spheres. Figure 2-7, also, shows how the cations are bound to the oxygen in both the tetrahedral and octahedral sites.

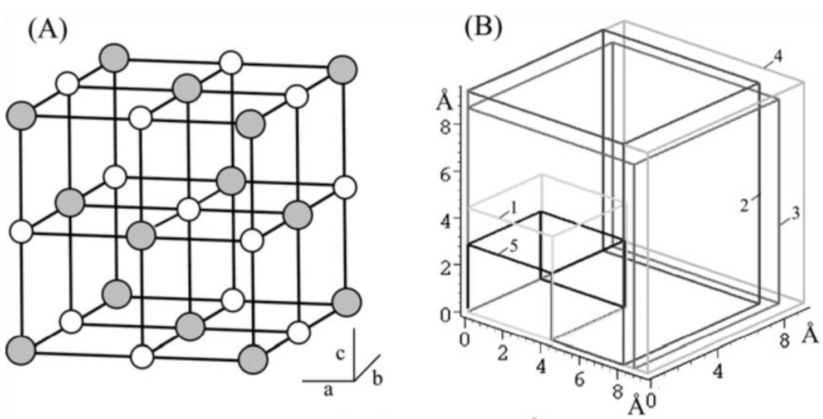

Figure 2-5: (A) Schematic of the rocksalt structure, where the oxygen ions are represented by the grey spheres and the white spheres are for the metallic ions. (B) Illustration of the unit cell dimensions of stable manganese oxides [65].

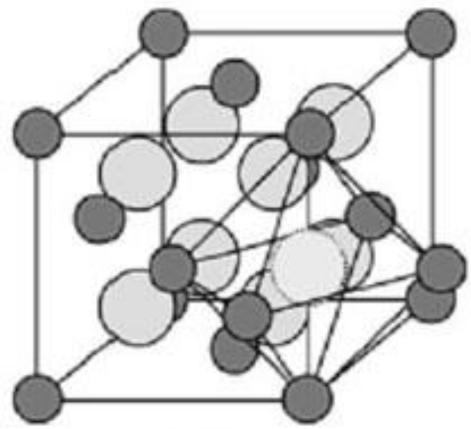

Figure 2-6: Schematic of a simple tetragonal rutile structure, where the darker spheres represent the oxygen ions and the lighter spheres represent the metallic ions [66].

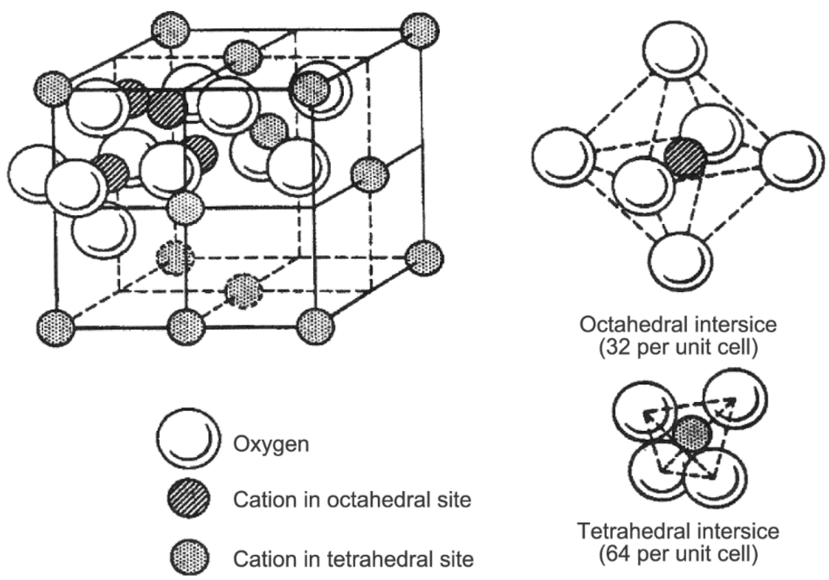

Figure 2-7: Schematic of a spinel structure.

2.2.3 Cobalt oxide and cobalt iron oxide

Cobalt, like manganese, has three cations, Co^{2+}, Co^{3+}, and Co^{4+} [66]. However, cobalt has two readily available oxides, CoO and Co_3O_4 [67]. The structure of these oxides is similar to those given in previous section for manganese. CoO (Co^{2+} oxidation state) has a rock salt structure, see figure 2-5. In CoO, Co^{2+} are octahedrally coordinated to the O^{2-} in the lattice. CoO lattice constant is 4.25 Å [67]. Co_3O_4 (Co^{2+} and Co^{3+}), the thermodynamically stable form of cobalt oxide at room temperature and pressure, has a spinel structure with Co^{2+} at the tetrahedral sites and the Co^{3+} at the octahedral sites, see figure 2-7. Co_3O_4 has a lattice constant of 8.38 Å. Although, CoO and Co_3O_4 are the stable oxides of cobalt, Co_2O_3 has been successfully prepared as impurity or with other chemical complexes [67]. $CoFe_2O_4$ has a crystal structure similar to that of $NiFe_2O_4$ discussed in section 2.2.1, a spinel ferrite. However, $CoFe_2O_4$, unlike other spinel ferrites, has an orbital moment that is not completely quenched leading to deviation from the Néel model's prediction of the saturation magnetization [2].

REFERENCES

[1] X. Batlle, A. Labarta, Finite-size effects in fine particles: magnetic and transport properties, J. Phys. D. Appl. Phys. 35 (2002) R15–R42. doi:10.1088/0022-3727/35/6/201.

[2] Morphological, magnetic and electronic structural studies of nanostructured spinel ferrites by Ghulam Hassnain Jaffari A dissertation submitted to the Faculty of the University of Delaware in partial fulfillment of the requirements for the degree of Doct, (2012).

[3] J. L. Dormann, D. Fiorani, E. Tronc, Magnetic relaxation in fine-particle systems, in: Adv. Chem. Phys., 1997: pp. 282–494. doi:10.1002/9780470141571.ch4.

[4] J. L. Dormann, F. D'Orazio, F. Lucari, E. Tronc, P. Prené, J.P. Jolivet, Thermal variation of the relaxation time of the magnetic moment of γ-Fe_2O_3 nanoparticles with interparticle interactions of various strengths, Phys. Rev. B. 53 (1996) 14291–14297. doi:10.1103/PhysRevB.53.14291.

[5] J. L. Dormann, R. Cherkaoui, L. Spinu, M. Noguès, F. Lucari, F. D'Orazio, From pure superparamagnetic regime to glass collective state of magnetic moments in γ-Fe_2O_3 nanoparticle assemblies, J. Magn. Magn. Mater. 187 (1998) L139–L144. doi:10.1016/S0304-8853(98)00135-8.

[6] W. Luo, S. R. Nagel, T. F. Rosenbaum, R. E. Rosensweig, Dipole interactions with random anisotropy in a frozen ferrofluid, Phys. Rev. Lett. 67 (1991) 2721–2724. doi:10.1103/PhysRevLett.67.2721.

[7] J. Zhang, C. Boyd, W. Luo, Two Mechanisms and a Scaling Relation for Dynamics in Ferrofluids, Phys. Rev. Lett. 77 (1996) 390–393. doi:10.1103/PhysRevLett.77.390.

[8] E. Vincent, Y. Yuan, J. Hammann, H. Hurdequint, F. Guevara, Glassy dynamics of nanometric magnetic particles, J. Magn. Magn. Mater. 161 (1996) 209–219. doi:10.1016/S0304-8853(96)00021-2.

[9] S. Shtrikman, and E. P. Wohlfarth, The theory of the vogel-fulcher law of spin glasses, Phys. Lett. 85 (1981) 467–470. doi:http://dx.doi.org/10.1016/0375-9601(81)90441-2.

[10] J. L. Dormann, L. Bessais, D. Fiorani, A dynamic study of small interacting particles: superparamagnetic model and spin-glass laws, J. Phys. C Solid State Phys. 21 (1988) 2015. doi:10.1088/0022-3719/21/10/019.

[11] J.L. Dormann, L. Spinu, E. Tronc, J. Jolivet, F. Lucari, F. D'Orazio, Effect of interparticle interactions on the dynamical properties of γ-Fe_2O_3 nanoparticles, J. Magn. Magn. Mater. 183 (1998) L255–L260. doi:10.1016/S0304-8853(97)01123-2.

[12] S. Mørup, E. Tronc, Superparamagnetic relaxation of weakly interacting particles, Phys. Rev. Lett. 72 (1994) 3278–3281. doi:10.1103/PhysRevLett.72.3278.

[13] A. Labarta, R. Rodrguez, L. Balcells, J. Tejada, X. Obradors, F.J. Berry,

Noncritical behavior and remanent magnetization in magnetically frustrated FeSbO4, Phys. Rev. B. 44 (1991) 691–698. doi:10.1103/PhysRevB.44.691.
[14] G. Hassnain Jaffari, T. Ekiert, K.M. Unruh, S. Ismat Shah, Effect of particle size distribution on the magnetic properties γ-Fe_2O_3 nanoparticles, Mater. Sci. Eng. B. 177 (2012) 935–941. doi:10.1016/j.mseb.2012.04.016.
[15] G. Hassnain Jaffari, S. Rizwan Ali, S. K. Hasanain, G. Güntherodt, S. Ismat Shah, Stabilization of surface spin glass behavior in core-shell $Fe_{67}Co_{33}$–$CoFe_2O_4$ nanoparticles, J. Appl. Phys. 108 (2010) 63921. doi:10.1063/1.3478738.
[16] H. Mamiya, I. Nakatani, Dynamic study of iron-nitride fine particle system: field dependence of the blocking temperature, J. Magn. Magn. Mater. 177–181 (1998) 966–967. doi:10.1016/S0304-8853(97)00572-6.
[17] P.E. Jönsson, J.L. García-Palacios, Relaxation time of weakly interacting superparamagnets, Europhys. Lett. 55 (2001) 418–424. doi:10.1209/epl/i2001-00430-0.
[18] A. Ceylan, S.K. Hasanain, S. Ismat Shah, Experimental observations of field-dependent activation of core and surface spins in Ni-ferrite nanoparticles, J. Phys. Condens. Matter. 20 (2008) 195208. doi:10.1088/0953-8984/20/19/195208.
[19] J.M.D. Coey, Noncollinear Spin Arrangement in Ultrafine Ferrimagnetic Crystallites, Phys. Rev. Lett. 27 (1971) 1140–1142. doi:10.1103/PhysRevLett.27.1140.
[20] S. Linderoth, P. V. Hendriksen, F. Bo/dker, S. Wells, K. Davies, S.W. Charles, et al., On spin-canting in maghemite particles, J. Appl. Phys. 75 (1994) 6583–6585. doi:10.1063/1.356902.
[21] K. Haneda, H. Kojima, A.H. Morrish, P.J. Picone, K. Wakai, Noncollinearity as a size effect of CrO_2 small particles, J. Appl. Phys. 53 (1982) 2686–2688. doi:10.1063/1.330893.
[22] R.H. Kodama, A.E. Berkowitz, E.J. McNiff, Jr., S. Foner, Surface Spin Disorder in $NiFe_2O_4$ Nanoparticles, Phys. Rev. Lett. 77 (1996) 394–397. doi:10.1103/PhysRevLett.77.394.
[23] D. Lin, A.C. Nunes, C.F. Majkrzak, A.E. Berkowitz, Polarized neutron study of the magnetization density distribution within a $CoFe_20_4$ colloidal particle II, J. Magn. Magn. Mater. 145 (1995) 343–348.
[24] F. Gazeau, E. Dubois, M. Hennion, R. Perzynski, Y. Raikher, Quasi-elastic neutron scattering on γ-Fe_2O_3 nanoparticles, Europhys. Lett. 40 (1997) 575–580. doi:10.1209/epl/i1997-00507-2.
[25] F. Gazeau, J. Bacri, F. Gendron, R. Perzynski, Y.. Raikher, V.. Stepanov, Magnetic resonance of ferrite nanoparticles:, J. Magn. Magn. Mater. 186 (1998) 175–187. doi:10.1016/S0304-8853(98)00080-8.
[26] M. García del Muro, X. Batlle, A. Labarta, Erasing the glassy state in magnetic fine particles, Phys. Rev. B. 59 (1999) 13584–13587. doi:10.1103/PhysRevB.59.13584.

[27] R.H. Kodama, S.A. Makhlouf, A.E. Berkowitz, Finite Size Effects in Antiferromagnetic NiO Nanoparticles, Phys. Rev. Lett. 79 (1997) 1393–1396. doi:10.1103/PhysRevLett.79.1393.
[28] B. Martínez, X. Obradors, L. Balcells, A. Rouanet, C. Monty, Low Temperature Surface Spin-Glass Transition in γ-Fe_2O_3 Nanoparticles, 80 (1998).
[29] R.H. Kodama, A.E. Berkowitz, Atomic-scale magnetic modeling of oxide nanoparticles, Phys. Rev. B. 59 (1999) 6321–6336. doi:10.1103/PhysRevB.59.6321.
[30] R.H. Kodama, A.E. Berkowitz, E.J.M. Jr, S. Foner, Surface spin disorder in ferrite nanoparticles (invited) Surface spin disorder in ferrite nanoparticles (invited), J. Appl. Phys. 5552 (1997) 3–9. doi:10.1063/1.364659.
[31] Ò. Iglesias, A. Labarta, Finite-size and surface effects in maghemite nanoparticles: Monte Carlo simulations, Phys. Rev. B. 63 (2001) 184416. doi:10.1103/PhysRevB.63.184416.
[32] W.H. Meiklejohn, C.P. Bean, New Magnetic Anisotropy, Phys. Rev. 102 (1956) 1413–1414. doi:10.1103/PhysRev.102.1413.
[33] U. Nowak, K. Usadel, J. Keller, P. Miltényi, B. Beschoten, G. Güntherodt, Domain state model for exchange bias. I. Theory, Phys. Rev. B. 66 (2002) 14430. doi:10.1103/PhysRevB.66.014430.
[34] L. Neel, Ferro-antiferromagnetic coupling in thin layers, Ann. Phys. Paris. 2 (1967).
[35] L. Néel, Antiferromagnetism and Ferrimagnetism, Proc. Phys. Soc. Sect. A. 65 (1952) 869–885. doi:10.1088/0370-1298/65/11/301.
[36] A.P. Malozemoff, Random-field model of exchange anisotropy at rough ferromagnetic-antiferromagnetic interfaces, Phys. Rev. B. 35 (1987) 3679–3682. doi:10.1103/PhysRevB.35.3679.
[37] A. Hoffmann, Symmetry Driven Irreversibilities at Ferromagnetic-Antiferromagnetic Interfaces, Phys. Rev. Lett. 93 (2004) 97203. doi:10.1103/PhysRevLett.93.097203.
[38] A. Aharoni, Introduction to the Theory of Ferromagnetism, Oxford Sci. Publ. I (2007) 303. doi:10.1063/1.881916.
[39] J. Nogués, I.K. Schuller, Exchange bias, J. Magn. Magn. Mater. 192 (1999) 203–232. doi:10.1016/S0304-8853(98)00266-2.
[40] Core/shell structured magnetic nanoparticles synthesized by inert gas condensation by Abdullah Ceylan A dissertation submitted to the Faculty of the University of Delaware in partial fulfillment of the requirements for the degree of Doctor of Philosophy, (2007).
[41] R.W. Chantrell, M. El-Hilo, K. O'Grady, Spin-glass behavior in a fine particle system, IEEE Trans. Magn. 27 (1991) 3570–3578. doi:10.1109/20.102929.
[42] R. Kiwi, M., Mejía-López, J., Portugal, R.D., Ramírez, Exchange bias model for Fe / FeF_2 : Role of domains in the ferromagnet, Europhys. Lett. 48 (1999) 573–579.
[43] M. Kiwi, J. Mejia-Lopez, R.D. Portugal, R. Ramirez, Exchange-bias systems

with compensated interfaces, Appl. Phys. Lett. 75 (1999) 3995–3997. doi:10.1063/1.125517.
[44] J. Nogués, I.K. Schuller, Exchange bias, J. Magn. Magn. Mater. 192 (1999) 203–232. doi:10.1016/S0304-8853(98)00266-2.
[45] C.L. Chien, Granular magnetic solids (invited), J. Appl. Phys. 69 (1991) 5267–5272. doi:10.1063/1.348946.
[46] B. Abeles, P. Sheng, M.D. Coutts, Y. Arie, Structural and electrical properties of granular metal films, Adv. Phys. 24 (1975) 407–461. doi:10.1080/00018737500101431.
[47] S. Stavroyiannis, I. Panagiotopoulos, D. Niarchos, J.. Christodoulides, Y. Zhang, G.. Hadjipanayis, Investigation of CoPt/M (M=Ag, C) films for high density recording media, J. Magn. Magn. Mater. 193 (1999) 181–184. doi:10.1016/S0304-8853(98)00501-0.
[48] S. Ohnuma, H. Fujimori, S. Mitani, T. Masumoto, High-frequency magnetic properties in metal–nonmetal granular films (invited), J. Appl. Phys. 79 (1996) 5130. doi:10.1063/1.361531.
[49] T. Morikawa, M. Suzuki, Y. Taga, Soft magnetic properties of CoCrO granular films, J. Appl. Phys. 83 (1998) 6664. doi:10.1063/1.367654.
[50] S. Mitani, H. Fujimori, K. Takanashi, K. Yakushiji, J.-G. Ha, S. Takahashi, Tunnel-MR and spin electronics in metal - nonmetal granular systems, J. Magn. Magn. Mat. 198–199 (1999) 179.
[51] Z. Nemati, H. Khurshid, J. Alonso, M. H. Phan, P. Mukherjee, H. Srikanth, From core/shell to hollow Fe/ γ-Fe_2O_3 nanoparticles: evolution of the magnetic behavior, Nanotechnology. 26 (2015) 405705. doi:10.1088/0957-4484/26/40/405705.
[52] C. Liu, J. Cui, X. He, H. Shi, Large exchange bias with remarkable thermostability in an inverted quasi core/shell CoO/γ-Fe2O3 granular system, J. Nanoparticle Res. 16 (2014) 2320. doi:10.1007/s11051-014-2320-7.
[53] A. Ceylan, C.C. Baker, S.K. Hasanain, S. Ismat Shah, Effect of particle size on the magnetic properties of core-shell structured nanoparticles, J. Appl. Phys. 100 (2006) 34301. doi:10.1063/1.2219691.
[54] S. Wei, Q. Wang, J. Zhu, L. Sun, H. Lin, Z. Guo, Multifunctional composite core-shell nanoparticles., Nanoscale. 3 (2011) 4474–502. doi:10.1039/c1nr11000d.
[55] E.L. Jr, E.L. Winkler, D. Tobia, H.E. Troiani, R.D. Zysler, E. Agostinelli, Bimagnetic CoO Core/$CoFe_2O_4$ Shell Nanoparticles: Synthesis and Magnetic Properties, Chem. Mater. 24 (2012) 512−516. doi:10.1021/cm2028959.
[56] I. Golosovsky, G. Salazar-Alvarez, A. López-Ortega, M. González, J. Sort, M. Estrader, S. Suriñach, M. Baró, J. Nogués, Magnetic Proximity Effect Features in Antiferromagnetic/Ferrimagnetic Core-Shell Nanoparticles, Phys. Rev. Lett. 102 (2009) 247201. doi:10.1103/PhysRevLett.102.247201.
[57] D. De, Ò. Iglesias, S. Majumdar, S. Giri, Probing core and shell contributions to exchange bias Co/Co_3O_4 nanoparticles of controlled size, Phys. Rev. B. 94

(2016) 184410. doi:10.1103/PhysRevB.94.184410.
[58] H. Khurshid, W. Li, M.H. Phan, P. Mukherjee, G.C. Hadjipanayis, H. Srikanth, Surface spin disorder and exchange-bias in hollow maghemite nanoparticles, Appl. Phys. Lett. 101 (2012) 1–6. doi:10.1063/1.4733621.
[59] G.H. Jaffari, A. Ceylan, C. Ni, S.I. Shah, Enhancement of surface spin disorder in hollow $NiFe_2O_4$ nanoparticles, J. Appl. Phys. 107 (2010) 13910. doi:10.1063/1.3277041.
[60] H. Khurshid, P. Lampen-Kelley, Ò. Iglesias, J. Alonso, M.-H. Phan, C.-J. Sun, M.-L Saboungi, H. Srikanth, Spin-glass-like freezing of inner and outer surface layers in hollow γ-Fe_2O_3 nanoparticles., Sci. Rep. 5 (2015) 15054. doi:10.1038/srep15054.
[61] A. Cabot, A. Alivisatos, V. Puntes, L. Balcells, Ò. Iglesias, A. Labarta, Magnetic domains and surface effects in hollow maghemite nanoparticles, Phys. Rev. B. 79 (2009) 94419. doi:10.1103/PhysRevB.79.094419.
[62] H. Perron, T. Mellier, C. Domain, J. Roques, E. Simoni, R. Drot, et al., Structural investigation and electronic properties of the nickel ferrite $NiFe_2O_4$: a periodic density functional theory approach, J. Phys. Condens. Matter. 19 (2007) 346219. doi:10.1088/0953-8984/19/34/346219.
[63] A. N. Grundy, B. Hallstedt, L.J. Gauckler, Assessment of the Mn-O system, J. Phase Equilibria. 24 (2003) 21–39. doi:10.1007/s11669-003-0004-6.
[64] H.C.W. Skinner, R.W. Fitzpatrick, Biomineralization: processes of iron and manganese : modern and ancient environments, Catena Verlag, 1992. http://books.google.com/books/about/Biomineralization.html?id=-hsaAQAAIAAJ&pgis=1 (accessed October 28, 2014).
[65] R. Tsybukh, A comparative study of platinum nanodeposits on HOPG (0001), MnO (100) and MnO_x/MnO (100) surfaces by STM and AFM after heat treatment in UHV, O_2, CO and H_2, 2010.
[66] B.D. Cullity, C.D. Graham, Introduction to Magnetic Materials, John Wiley & Sons, Inc., Hoboken, NJ, USA, 2008. doi:10.1002/9780470386323.
[67] J. BERGSTRÖM, Oxidation of Cobalt Nanocrystals: Investigation of the Role of Nanocrystallinity, Self-Ordering and Nanocrystal Size, PhD Thesis. (2013). http://publications.lib.chalmers.se/records/fulltext/179402/179402.pdf.

Chapter 3

EXPERIMENTATION

The numerous benefit of magnetic NPs, namely their versatility to be used in many different applications, e.g. high density data storage, have been made possible by the development of new measuring techniques over the years, as well as improvement in growth techniques, which allows for a more controlled growth at the nanometer scale [1–5]. Physical evaporations growth techniques such as thermal evaporation have an advantage over other growth techniques such as chemical routes since the later techniques that may require the use of surfactants to make sure NPs do not agglomerate [2]. NPs with surfactants reduces some of the interactions of the NPs discussed in the previous chapter which, as was stated, enhance magnetic properties of NPs. Therefore, having surfactant at the surface of the NPs will lead to lost magnetic enhancement. Therefore, thermal evaporation techniques are specifically necessary to grow magnetic NPs.

There are many different types of thermal evaporation techniques, here we will employ an inert gas condensation (IGC) system, since this system produces particles with a narrow particle size distribution [2,3,6]. IGC have four different parameters that can be tuned to control the size of the NPs: chamber temperature, chamber pressure, proper selection of inert gas, and inert gas circulation rate. As already mentioned, development of such growth systems as well as new characterization techniques are what lead to the surge of NPs synthesis and research in the recent decades. Along with the IGC system, x-ray diffraction (XRD), x-ray photoelectron spectroscopy

(XPS), high resolution transmission microscopy (HRTEM), and physical property measurement system (PPMS) are the main characterization techniques used in this thesis and their introduction will be the subject of this chapter.

3.1 Inert Gas Condensation

In 1930, in the search of a new technique to growth bismuth-black to be used in radiometric devices, which required minimization of black mass, Pfund et al. evaporated bismuth with the help of a hot tungsten spiral at a moderated pressure [7]. This process allowed for a new way to obtained desired clustered metallic particles, where volatized monomers aggregate into clusters by first decomposing bulk metals into a monomer population with the used a heating source (tungsten based heating source), followed by a cooling of the monomer when they lose thermal energy after collision with inert gas atoms, and subsequently growth of the clusters with addition of monomers to individual clusters and by aggregation of different clusters [8,9]. This process has come to be known as inert gas condensation (IGC) and has been used since its refinement by Geilbert's group to evaporate metallic NPs. Many different iterations of this system have since been developed, from the methods of loading the metal into the evaporating system, to the collection of the resulting NPs. Loading methods vary from wire feed to directly placing metal chunks on the heating source (e.g. boat or crucible).

To set up the condition desired for the NPs growth in the IGC chamber, we first evacuated the chamber to 10^{-3} Torr with the help of a mechanical pump followed by high vacuum pumping with a turbo-molecular pump, which brought the chamber to a pressure of 5 x10^{-6} Torr over a period of 24 hours. After the chamber reached the high vacuum, the inert gas (e.g. helium) was introduced into the system to the desired growth pressure, which highly impact the size and shape of the NPs. After the desired pressure is reached, the inert gas is circulated with the help of a roots blower, where the rate of the circulation also influences the characteristics of the NPs. With growth pressure stabilized with the gas being circulated the heating source is slowly brought to a temperature above the melting temperature of the metal being evaporated. The temperature is controlled by power source, which resistively heats a tungsten boat by adjusting the power of the power supply. The temperature at the heating source is recorded by an infrared gun pointed at the source. Once the critical temperature is reached, where the metal starts forming vapors, the vapors are swept away by the circulating inert gas toward a metallic sieved filter that is at a significantly lower temperature then the heating source. Due to the high thermal conductivity of the inert gas, the metallic vapors are cooled quickly as they are swept away from heating source and the process described above takes place.

The chamber pressure, circulation rate, type of inert gas and evaporation temperature all effect the size of the resulting NPs. Helium is the gas used since it has the highest heat capacity of all the noble gases. The circulated gas must be inert since we interested in obtaining NPs of the evaporated materials. The effect of pressure on the size of NPs is a complex and is the most important effect. Diffusion rates (nucleation and growth) and partial pressure (collision probability) compete in controlling the size of the NPs. Diffusion is the main transport phenomenon for the metallic vapors; whereas the partial pressure of the inert gas dictates the collision probability of the nuclei and, subsequently, of clusters with each other and with the inert gas. It was determined that it is the partial pressure that contributes the most in controlling the particle size [10,11]. Increase in pressure allows for higher probability of nuclei to coalesce to form bigger particles [10,11]. Evaporation temperature also has a positive effect on the size of the particles, increase in temperature results in increase in size, since kinetic energy increase with temperature which is correlated to the higher activity from both the nuclei and inert gas [12].

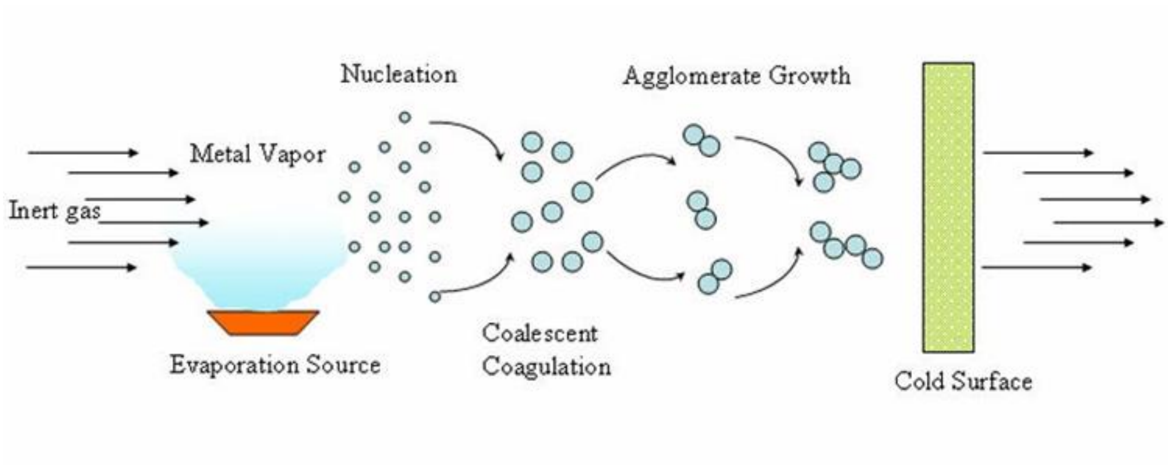

Figure 3-1: Schematic diagram of the particles growth process [10].

In the schematic diagram shown in figure 3-1, we present the three stages that particles follow after evaporation to metallic vapors to the finally obtained NPs in an IGC system: nucleation, coalescent/coagulation, agglomeration. During nucleation stage, metallic vapor supersaturates as they are swept away with the inert gas where temperature decreases as the gas moves away from the heating source. The overall pressure of the chamber is raised by the addition of the newly evaporated metal, this leads to the increase of number of the nuclei. With the decrease of thermal energy nucleation rate decreases with the decrease of thermal energy, however the kinetic energy is high enough for the recently form nuclei to coalesce to each other upon collision to other nuclei – this is the coalescence stage. Increase in size of the coalesced particles further increase the probability of collision and subsequently leading to bigger particles, which is highly affect by the vapor pressure in the chamber and the amount of time the coalesced particle must hit each other in a temperature zone. The last stage is where thermal energy is low enough that coalescence is no longer favorable and particles only agglomerate after inelastic collision before being collected to the metallic sieved filter.

The exact set up of the IGC system used for the samples preparation is shown in figure 3-2. The different components of the system, which have already been introduced and discussed above are clearly labeled. Most of the samples that were grown were evaporated by introducing metallic wires with the desired stoichiometry, however the manganese oxide NPs were grown from manganese pieces that were directly placed on the alumina coated tungsten boat filled with and resistively heated with a high current supply. A molybdenum sieved sheet with pore size around 1 mm was placed on top of the boat to keep the metal pieces from flying off before they were completely melted. A similar set up, where manganese pieces where evaporated to form NPs, had already been used by M. B. Ward [13].

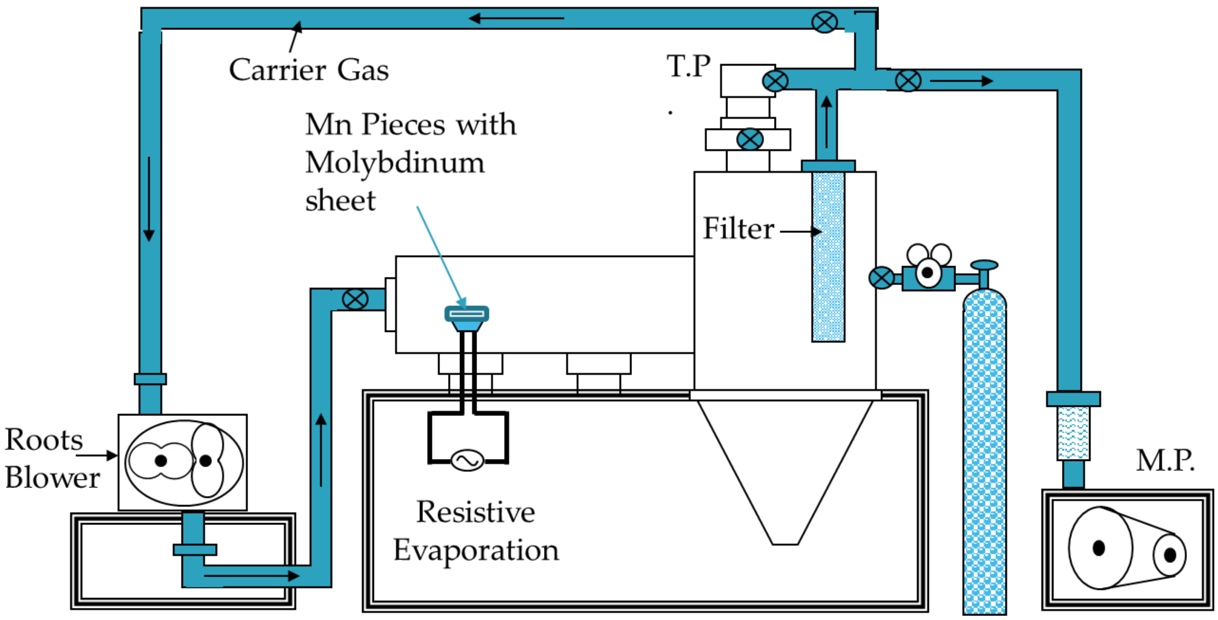

Figure 3-2: Schematic diagram of IGC system with metal pieces feed setup [10].

All NPs collected from the IGC system were heat treated, except for the manganese oxide NPs since manganese completely oxidized easily during the growth even though the system was evacuated to 2 x 10^{-6} Torr before being filled to 500 mTorr of working pressure with helium gas. After the NPs were heat treated to desired conditions, the crystallographic, morphology, and magnetic properties were investigated. The techniques involved in those investigations are discussed below.

3.2 X-ray Diffraction

X-rays, which have wavelength in the order comparable to atomic dimensions (e.g. Cu K_α = 0.15406 nm) are used to probe the crystal structure of the obtained NPs.

This probing utilizes x-ray diffraction (XRD) technique. Since the x-rays utilized are at the atomic dimension, they are used to investigate the interatomic distances, which leads to the identification of the crystal structure, lattice spacing, crystal size, texturing, etc. It was in 1912 that Bragg first used collected diffracted x-rays to determine the crystal structure of materials. From his results, Bragg derived equation 3.1 to explain the generation of diffraction pattern in a sample under X-rays exposure.

$$n\lambda = 2dsin\theta_{hkl} \tag{3.1}$$

Equation 3.1, known as Bragg's law, says that when a monochromatic x-ray beam of wavelength (λ) is incident on a crystalline material at an angle (θ), diffraction patterns are observed when there's constructive interference of the various planes in the crystalline sample. The resulting observed planes are known as d-spacing which are formed when the reflected x-rays are a whole number (n) apart. The ($h\ k\ l$) refer to the notation method employed in crystallography to identify planes in crystal lattices, referred to as Miller indices.

The resulting X-ray pattern can be used to deduce additional information, other than how far apart crystal plane are to each other – d-space, which satisfies the Bragg's law. Crystallite size can also be deduced, by analyzing the breadth of the obtained peaks. Scherer used the broadening of the resulting peaks to help determine the average particle size by deriving equation 3.2.

$$D = \frac{0.9\lambda}{\beta cos\theta} \tag{3.2}$$

Equation 3.2 states that the particle size, in other word crystallite size (D) is dependent on λ, θ and the full width at half maximum (FWHM) of the peak in radians (β), where the coefficient 0.9 refers to spherical particles. FWHM is, however, a bit complicated since instrumentations also introduce their own FWHM (β_0), this must be correct for each instrument before the application of equation 3.2 can be used to determine D. Even though β_0 can be removed from the peak breadth of the patterns, particle size and other morphological changes such as strain highly effect the peak broadening. To take these different effects into consideration equation 3.3 must be used as the FWHM into equation 3.2. In equation 3.3, ε is the strain. It's worth noting, though, that the spectral broadening is still not considered, which has been observed to be dominant at $2\theta > 50^o$ [14].

$$\beta_t^2 \approx \left[\frac{0.9\lambda}{Dcos\theta}\right]^2 + (4\varepsilon tan\theta)^2 + \beta_0^2 \qquad (3.3)$$

3.3 X-ray Photoelectron Spectroscopy

Other x-ray sources are also used to probe the chemical makeup of the grown NPs, namely Al Kα with an energy of 1487 eV. Here, the binding energy of core electrons of compounds of the NPs are investigated by collecting resulting electrons after being displaced from their binding from an incident electron beam, the system that allow such probing is called x-ray photoelectron spectroscopy (XPS). XPS has become a very popular technique in recent years due to its ability in probing chemical state of materials. It was first developed by Siegbahn et al. in the 1950s, when they used it to investigate the electronic structure of different materials [15]. In their experiment, they used a focus beam of photons to irradiate a sample, then consequently collected emitted electrons. This was based on a theory first proposed by Einstein, where he predicted the equation below.

$$K.E. = h\nu - E_B \tag{3.4}$$

Where he showed that the kinetic energy (K.E.) of an ejected photoelectron is the difference of the incident beam ($h\nu$) and the binding energy (E_B) of the electron in the k^{th} orbital of the specimen.

Resulting electrons are collected and analyzed by an electron energy analyzer or detector. An energy spectrum as a function of the number of electrons having a specific energy is then produced - a graph of the intensity of the photoelectron, the electron count per second and the E_B. From the graph, peaks with finite breadth are observed; these peaks have different shape and breadth and correspond to the transition of the different core electrons levels of the samples, for example for 2p, 3s, and 3p electrons. These peaks are due to electrons that escape the sample without any inelastic collisions with other atoms [15]. Other than the already mentioned peaks, a continuously increasing background is observed as well, which is a result of different interaction of the electrons. Due to the multiple interaction of electrons after being emitted make this technique a little complicate to understand in term of deconvoluting the spectra, specifically in explaining or modeling the background. Any attempt at mathematically model the background can be problematic.

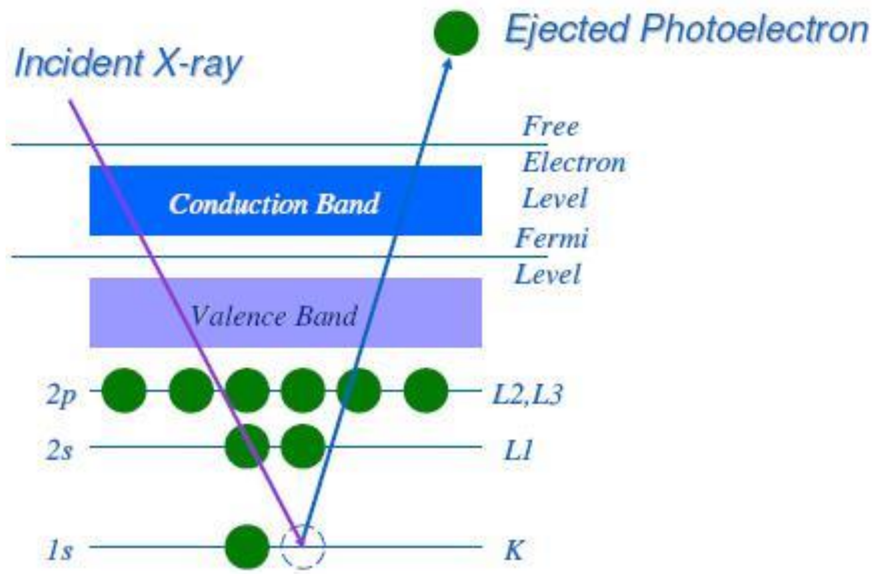

Figure 3-3: Principle of electron emission from an incident X-ray.

Figure 3-3 shows a schematic representation of the proposed theory by Einstein, where the incident photons eject electrons to be collected and analyzed. This illustration clearly visualizes that the resulting peaks in the spectrum are related to the density of the electronic states. In the illustration, quantized and discrete bands are shown. It is known that electronic states in metals and semimetals are quantized and consist of discrete bands. Therefore, this technique is a great way of determining the electronic structure of metals and semiconductors since it collects kinetic energy of emitted electrons from specific core electrons. Phenomena, such as plasmon losses, multiplet splitting, etc., add a degree of difficulty in the analysis of the resulting spectra.

Figure 3-4 shows a typical set up of an XPS system. The schematic divides the set up in three distinct parts: the energy source, the hemispherical energy analyzer, and the analyzer control. Both the energy source and the hemispherical energy analyzer are maintained in a very high vacuum system. An ultrahigh vacuum is used since there's a need to collect electrons that least interactions with other molecules to correctly probe the kinetic energy of the emitted electrons as well as obtain a reasonably clean surface for analyses. Having an ultrahigh vacuum allows the emitted electrons to reach the analyzer without much scattering, which results in an energy loss at each collision [15].

The x-ray source can vary from an x-ray tube to a monochromators source. Of the source listed here, monochromator sources have an advantage, as they improve the incident beam resolution. Synchrotron sources are used as well to help increase the intensity of the incident beam. It's worth noting here, that only electrons from few nanometers deep (~15 nm) in the sample can escape and subsequently be collected, even though the incident source can penetrate deep inside the sample. Therefore, this makes XPS a surface analysis technique. The exact escape depth can be determined from equation 3.5, which provides the probability of the distance ($P(x)$) that can be traveled by a photoelectron without encountering inelastic scattering (x). In equation 3.5, k is a normalizing constant and λ is the attenuation length of the photoelectrons. λ is electronic state dependent, since it represents the inelastic mean free path that an electron can travel before it loses energy [15,16].

$$P(x) = ke^{\frac{x}{\lambda}} \tag{3.5}$$

The hemispherical energy analyzer is made of two concentric hemispheres and an electrostatic lens system. After the electrons are ejected from the sample, a set of lenses are used to direct the electrons toward the tow concentric hemispheres. The use of the optical lenses help improve the spatial and angular resolution. Once at the concentric hemispheres, the electrons are accelerated around a curve by a constant applied voltage, which helps filter electrons that have high energy to pass through the system and reach the collector plate. The applied energy is varied as to select which electrons get to pass to the analyzer at any given time. This helps reduce the signal to noise ratio, therefore increasing the resolution of the collected spectrum. The down fall of this system is the loss of sensitivity by reduction of slower moving electrons, even with the employment of focusing lenses.

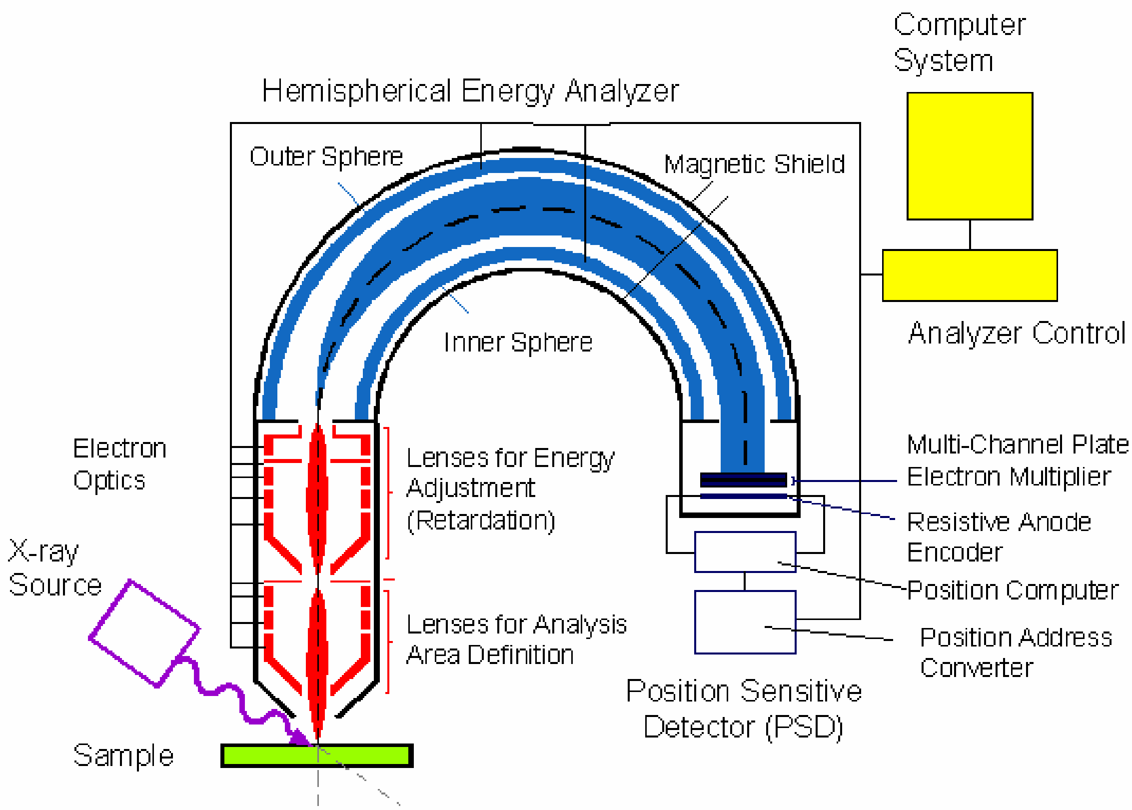

Figure 3-4: Schematics of XPS analyzer [17].

The resulting spectra collected by the hemisphere is observed with the help of a computer system. The computer system, also, controls the applied voltage at the hemisphere. Information such as pass energy, which is the energy of the electrons entering the analyzer, is controlled here. From the pattern collected at the computer information of chemical composition can be deduced by using standard binding energies.

Resolution is a very important parameter. It is related to the peak breadth and is comprised of the broadening from choice of X-ray, width of the analyzer energy window which is due to the physical setting of the detector, and the natural line width of the atomic orbital [17]. X-ray source is typically a fixed parameter once a measuring system is chosen. Monochromatic and synchrotron sources, which have FWHM of 0.3-0.4 eV, could be used in the place of the Al Kα (0.85 eV) source used in this this thesis. Therefore, adjustment of the resolution is limited to the detector. The detector parameters offer a tradeoff between higher resolution and lower intensity, by changing the noise to signal ratio. Noise to signal ratio can be adjusted by changing the parameter of the lens mentioned above.

3.4 High Resolution Transmission Electron Microscopy

In addition to the crystal structure and chemical makeup of grown NPs, the morphology of NPs greatly affect their magnetic properties which has been discussed in chapter 2. Transmission electron microscope (TEM) allows the observation of materials in micro and submicron ranges. Therefore, it is utilized here to explore the morphology of the NPs, which will help greatly in understanding magnetic measurement results. High resolution transmission electron microscopy (HRTEM) is used when exploring NPs at the 5 nm size range. In the case of the magnetic materials, a correlation between magnetic behavior, particle agglomeration and morphology needs to be understood. It helps identify polymorph structures that might be shown on XRD as simple amorphous material, or further show amorphous material that might be masked by crystalline phases. This is especially important for core/shell nanoparticles where the core and shell will have different crystalline phases.

In contrast to optical microscope, which uses a light source to explore the structure of materials, TEM uses electrons. The use of electrons as a source greatly increases the resolution of the microscope, where the smaller wavelength produced by the electrons help distinguish very small features that are equal size length to the wavelength of the electron beam. The increase in resolution (R) by using an electron source compared to that of a light source. Equation 3.6, below, shows how the two different sources could yield very different resolution, with the electron source having a R in the order of thousand better than that of the light source. Therefore, TEM has become a very attractive tool for probing small length scales materials. Resolution is usually denoted as d however here we use R to avoid confusion since d has already been assigned to the distance between crystal plans.

$$R = \frac{0.61\lambda_e}{\mu sin\varphi} \tag{3.6}$$

In equation 3.6, μ is the refractive index of the viewing medium and is usually approximated to be 1, φ is the semi-angle of collection of the magnifying lens, which is only a few degrees, and λ_e the wavelength of the electron beam (in nm), not to be confused with the λ given above for the wavelength of the X-ray source. Typically in

TEM, the source is given in terms of accelerating voltage (in kV), and it ranges from 100 kV and 400 kV. V is related to λ_e by equation 3.7.

$$\lambda_e \approx \frac{\mathrm{h}}{\sqrt{2m_0E\left(1+\frac{E}{2m_0c^2}\right)}} \approx \frac{1.22}{\sqrt{V}} \tag{3.7}$$

In equation 3.7, h is the Planck's constant; E is the energy of the accelerated voltage; m_0 is the rest mass of an electron; and c is the speed of light. It can be deduced from this equation that λ_e is 0.27 nm when employing an accelerating voltage of 200 kV.

The first microscope to use electrons as source was first constructed by Knoll and Ruska in 1931. However, it was not until 1938 that the electron microscope was able to have a resolution higher than that of light microscopes; this microscope was constructed by Siemens. The increase in resolution was made possible by the implementation of magnetic lenses. A schematic description of a typical TEM is given in figure 3-5, along with its components. A typical TEM can be broken down into three distinct components: electron source (production and acceleration of electrons), focusing of electrons (lenses, deflection coils, stigmators, apertures), and the collection of and manipulation of gathered transmitted signals into an image of the probed material. These three different components will be further discussed by starting with the generation and acceleration of electrons. In TEM, an electron beam with λ_e is usually emitted from a thermionic filament (e.g. tungsten, LaB_6) or field emission electron gun. The second stage where the emitted gets focused and accelerated is made of a condenser system, objective lenses, diffraction/intermediate lenses, projective lenses, and an image observation screen. Two condenser lenses are used to condense the electron beam. The objective, intermediate and projector lens are used to focus an image or the diffraction of specimen on the screen; the objective lens is probably the most important lens since it generates the first intermediate image. After the focused and accelerated electron beam interact with the sample, different modes of imaging are utilized to obtain an image of interest from the numerous resulting. From the interaction, both elastic and inelastic scattering of the electron beam happens, and results in backscattered electrons and secondary electrons. The different modes of imaging available to TEM use these electrons to do elemental analyses, topographical imaging, and compositional analyses. From the scattered electrons, an image is formed by inserting an aperture into the back focal plane of the objective lens, thereby blocking most of the diffracted pattern except those of interest. When the directly reflected beam is chosen, the image is said to a bright field (BF) image, whereas the image is said to be dark field (DF) when any other scattered electrons are used to form the image. The two different modes are used to obtain different contrast of the image, where BF image is obtained from the center beam and the DF image is obtained from other scattered electrons.

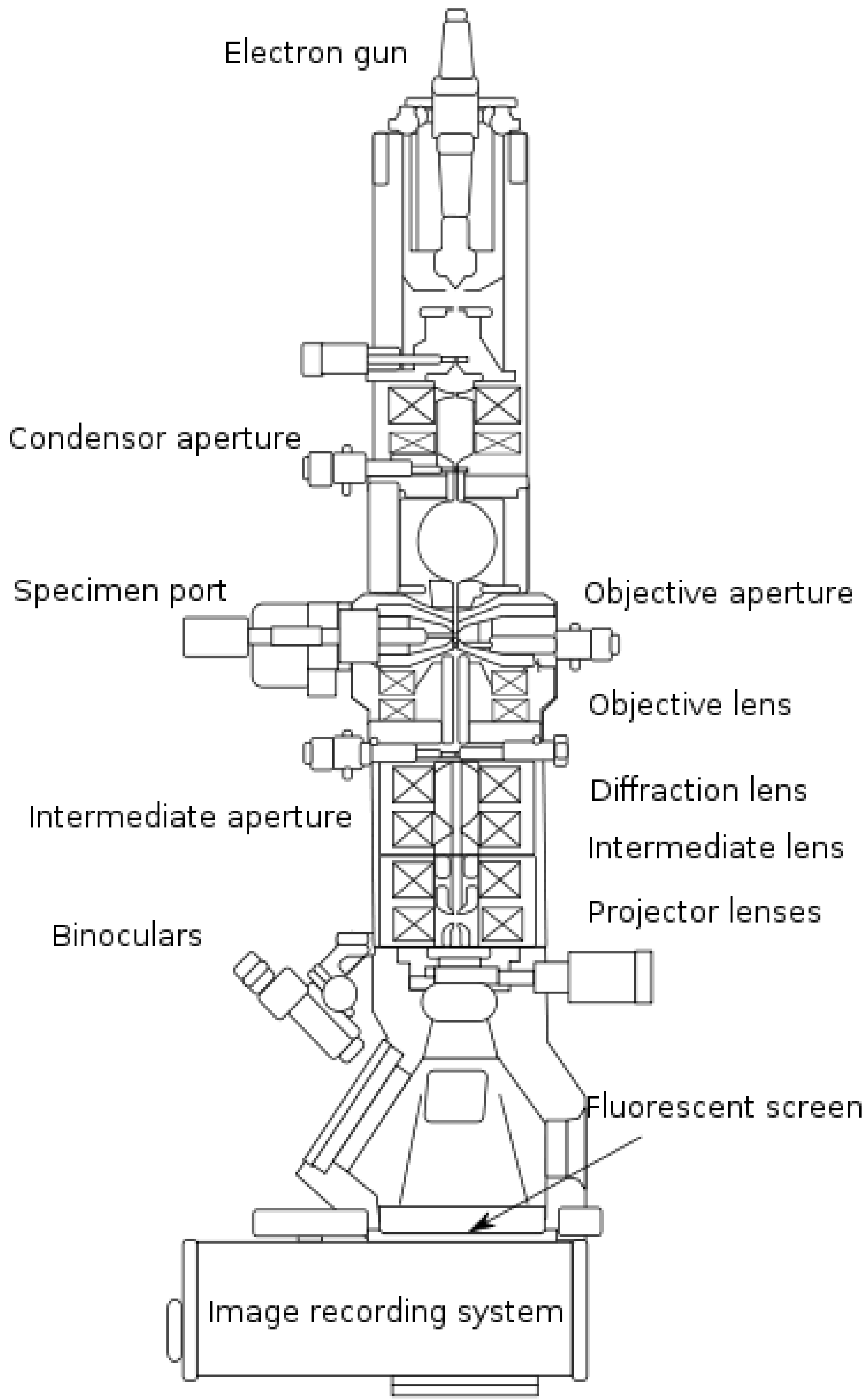

Figure 3-5: Typical basic outlining of a TEM system along with its component [18].

For this thesis, the JEOL 2010FX TEM with a 200 kV accelerating voltage was used to study the morphology of the grown NPs. The system was used to obtain very high resolution images where elemental analyses, topographical imaging, etc., were made possible. It helped shed light on the morphology of the samples, core/shell composition, and the particle size range.

3.5 Physical Property Measurement System

The magnetic properties of the grown NPs were recorded with a Physical Property Measurement System (PPMS). The PPMS, from Quantum Design, can do both AC susceptibility and DC magnetization measurements. Where AC measurements are nearly three orders of magnitude more sensitive that DC measurements [2]. To consider, only, the noncompaction contribution of the grown sample, DC measurements of the pressed NPs on a Kapton® tape were carried out by mounting onto a PPMS DC extraction magnetometer. The measurements included hysteresis study at different constant temperatures starting at 5 K up to 300 K with different increment of temperature, where different cycling of cooling field was carried for both Zero Field Cooled (ZFC) and Field Cooled (FC). Temperature effect on the magnetization was also explored for both FC and ZFC conditions from 5 K to 350 K. AC susceptibility at different frequency as function of temperature was also carried out to explore spins behavior.

$$emf = -\frac{d\varphi_B}{dt} = -A\frac{dB_\perp}{dt} \tag{3.8}$$

Magnetic measurement with PPMS is made possible by employing Faraday's law, which state that time rate of change of magnetic flux ($\frac{d\varphi_B}{dt}$) is equal to the measurements the electromotive force (emf) induced in a circuit [17]. This relation is given in equation 3.8, where $B_{\perp}$ is the component of the magnetic field perpendicular to the loop and A is the area of a loop wire. Therefore, to record the magnetic response of the prepared NPs, the Kapton ® which contains pressed NPs is vibrated inside the system which contains coils. From the constant frequency and amplitude of the Kapton ® inside the system, *emf* is generated and converted to magnetic flux readings – magnetizing forces. Samples with known values of correlation between magnetic flux and voltage reading are used to calibrate the system before measurement. With the system calibrated, the magnetic behavior of the grown NPs was recorded. The specific sequencing of the magnetic measurements is discussed in the individual section of each of the following chapters.

REFERENCES

[1] X. Batlle, A. Labarta, Finite-size effects in fine particles: magnetic and transport properties, J. Phys. D. Appl. Phys. 35 (2002) R15–R42. doi:10.1088/0022-3727/35/6/201.

[2] A. Ceylan, Core/shell structured magnetic nanoparticles synthesized by inert gas condensation by Abdullah Ceylan A dissertation submitted to the Faculty of the University of Delaware in partial fulfillment of the requirements for the degree of Doctor of Philosophy, (2007).

[3] A. Ceylan, C.C. Baker, S.K. Hasanain, S. Ismat Shah, Effect of particle size on the magnetic properties of core-shell structured nanoparticles, J. Appl. Phys. 100 (2006) 34301. doi:10.1063/1.2219691.

[4] G. Hassnain Jaffari, S. Rizwan Ali, S.K. Hasanain, G. Güntherodt, S. Ismat Shah, Stabilization of surface spin glass behavior in core-shell $Fe_{67}Co_{33}$–$CoFe_2O_4$ nanoparticles, J. Appl. Phys. 108 (2010) 63921. doi:10.1063/1.3478738.

[5] X. Liu, B. Geng, Q. Du, J. Ma, X. Liu, Temperature-controlled self-assembled synthesis of CuO, Cu_2O and Cu nanoparticles through a single-precursor route, Mater. Sci. Eng. A. 448 (2007) 7–14. doi:10.1016/j.msea.2006.08.104.

[6] G.H. Jaffari, A. Ceylan, C. Ni, S.I. Shah, Enhancement of surface spin disorder in hollow $NiFe_2O_4$ nanoparticles, J. Appl. Phys. 107 (2010) 13910. doi:10.1063/1.3277041.

[7] A.H. Pfund, Bismuth black and its applications, Rev. Sci. Instrum. 1 (1930) 397–399. doi:10.1063/1.1748708.

[8] H. Gleiter, Nanocrystalline materials, 33 (1990) 223–315.

[9] H. Hahn, Gas phase synthesis of nanocrystalline materials, Nanostructured Mater. 9 (1997) 3–12. doi:10.1016/S0965-9773(97)00013-5.

[10] C.G. Granqvist, R.A. Buhrman, Ultrafine metal particles, J. Appl. Phys. 47 (1976) 2200–2219. doi:10.1063/1.322870.

[11] A. Thölén, On the formation and interaction of small metal particles, Acta Metall. (1979). http://www.sciencedirect.com/science/article/pii/0001616079900907.

[12] S. Yatsuya, S. Kasukabe, R. Uyeda, Formation of ultrafine metal particles by gas evaporation technique. I. aluminium in helium, Jpn. J. Appl. Phys. 12 (1973) 1684. doi:10.1143/JJAP.12.1675.

[13] M.B. Ward, R. Brydson, R.F. Cochrane, Mn nanoparticles produced by inert gas condensation, J. Phys. Conf. Ser. 26 (2006) 296–299. doi:10.1088/1742-6596/26/1/071.

[14] R. Delhez, T.H. de Keijser, E.J. Mittemeijer, The X-ray diffraction line broadening due to the diffractometer condition as a function of 2θ, J. Phys. E. 11 (1978) 649–652. doi:10.1088/0022-3735/11/7/015.

[15] N. Winograd, S.W. Gaarenstroom, X-Ray Photoelectron Spectroscopy, in: Phys. Methods Mod. Chem. Anal., Elsevier, 1980: pp. 115–169.

doi:10.1016/B978-0-12-430802-2.50007-5.
[16] S. Hüfner, Photoelectron spectroscopy: principles and applications, Springer Ser. Solid-State Sci. 82. (1996) 1 online resource (xiv, 516 pages). http://purl.oclc.org/DLF/benchrepro0212%5Cnhttp://ezproxy.library.arizona.edu/login?url=http://dx.doi.org/10.1007/978-3-662-03209-1.
[17] Morphological, magnetic and electronic structural studies of nanostructured spinerl ferrites by Ghulam Hassnain Jaffari A dissertation submitted to the Faculty of the University of Delaware in partial fulfillment of the requirements for the degree of Doct, (2012).
[18] D.B. Williams, C.B. Carter, Transmission Electron Microscopy: A Textbook for Materials Science, 2009. doi:10.1007/978-1-61779-415-5_23.

Chapter 4

HOLLOW POLYCRYSTALLINE $NiFe_2O_4$ NANOPARTICLES: STUDY OF SURFACE EFFECT ON THE EXCHANGE BIAS AND MAGNETIC IRREVERSIBILITY

4.1 Abstract

This chapter explores the effect of the presence of inner surface on polycrystalline hollow single oxide nanoparticles of $NiFe_2O_4$. The chapter first discusses the successful synthesis of polycrystalline $NiFe_2O_4$ nanoparticles by inert gas condensation and their characterization. It then reports on extensive field and temperature dependent magnetic measurements. Hollow morphology is obtained by post-synthesis annealing of $Ni_{33}Fe_{67}/NiFe_2O_4$ core/shell particles, prepared in an inert gas condensation system. The high coercivity and exchange bias values obtained at low temperatures are attributed to the strong coupling between the ferrimagnetic (FiM) phase and its surround disordered surface spins that arises due to enhancement in the surface to volume ratio associated with the morphology of the particles.

4.2 Introduction

Reducing the size of magnetic nanoparticles (NPs) have been the subject of intense research and the effect of this reduction on the magnetic properties has made magnetic NPs useful in various fields such as medicine, sensors, recording media, etc. [1–9]. This effect was discussed in chapter 2, where it was shown that morphology strongly effects the magnetic response. In hollow nanoparticles, enhanced contribution from the surface SP transition has been reported due to the presence of additional inner surface and hence high surface to volume ratio [5–7]. In polycrystalline nanoparticles, where single NPs are composed of multiple randomly oriented crystallographic domains, higher coercivity, relatively high temperature magnetic irreversibility, lack of magnetic saturation, high blocking temperature, exchange bias, etc., have been reported and compared with properties of the core/shell nanoparticles and the bulk material [10–13]. Changes in morphology from solid to core/shell to hollow NPs reduces the magnetization of magnetic NPs [7,14,15], however effective anisotropy and EB effect increase [16]. Effect on the EB and overall effective anisotropy of the system have been attributed to the presence of disordered spins located both at the inner and outermost surfaces of the hollow nanoparticles and at the interfaces between crystallographic domains. This chapter provides conclusive work on temperature dependence of coercivity field (H_C), exchange bias (H_C) and magnetic irreversibility temperatures of polycrystalline hollow magnetic $NiFe_2O_4$ NPs. Presence of large spin disorder has been observed and discussed in detail.

4.3 Experimental Section

Synthesis of hollow NPs was discussed in chapter 3. Briefly, an inert gas condensation (IGC) system produces metallic $Ni_{33}Fe_{67}$ NPs surrounded by a thin oxide layer, $NiFe_2O_4$, when resistively evaporating a bimetallic NiFe wire are slowly exposed to atmosphere. Post-synthesis annealing in an oxygen environment at 300°C for 0.5 hours produced $NiFe_2O_4$ NPs with hollow morphology. The annealing condition were optimized to produce polycrystalline hollow nanoparticles [15].

4.4 Structural and Morphological Studies

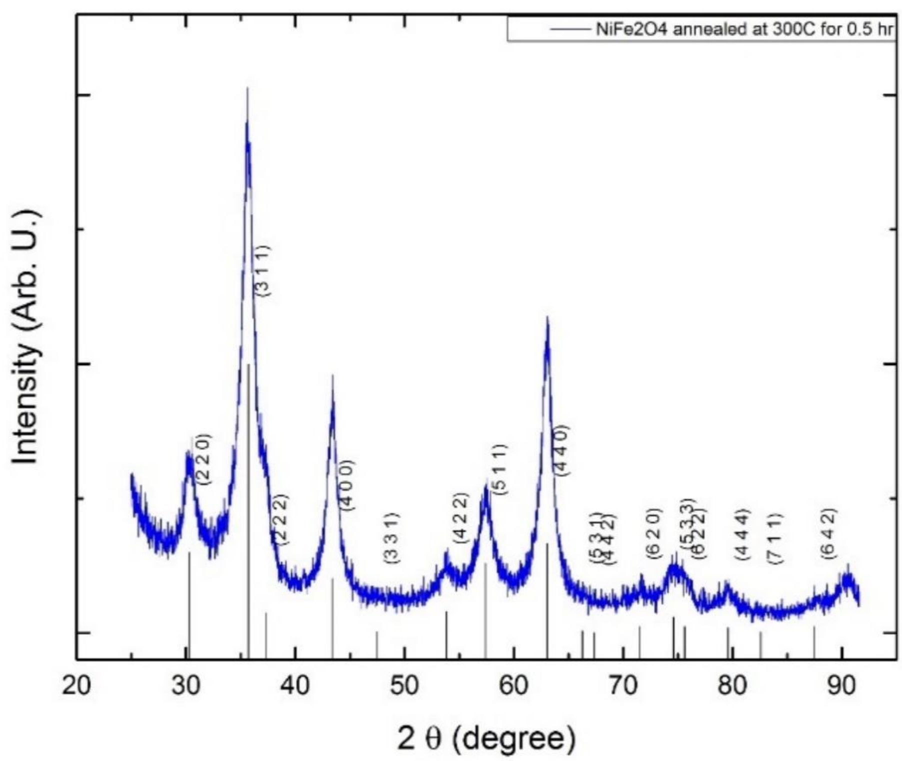

Figure 4-1: X-ray diffraction pattern of $NiFe_2O_4$ NPs grown in IGC system and annealed at 300°C for 0.5 hours, with matched standard pattern, JCPDF #74-2081.

X-ray diffraction pattern of synthesized $NiFe_2O_4$ NPs is shown in figure 4-1. Post synthesis in-situ annealing at 300°C for 0.5 hours led to the formation of single phase $NiFe_2O_4$ structure that matched well with the standard JCPDF card 74-2081. Reflections associated with different crystal planes are marked. Peaks are broad which is a manifestation of small average crystal size. Average crystallite size was extracted from the obtained XRD patterns using Scherrer's formula. The average crystallite size was 12 nm. In the calculation of the size of the crystallites, 0.9 was used for the shape factor and the most intense peak was used (35.69°). It was determined from the pattern that the sample fully oxidized as no $Ni_{33}Fe_{67}$ related peak was observed in the obtained pattern.

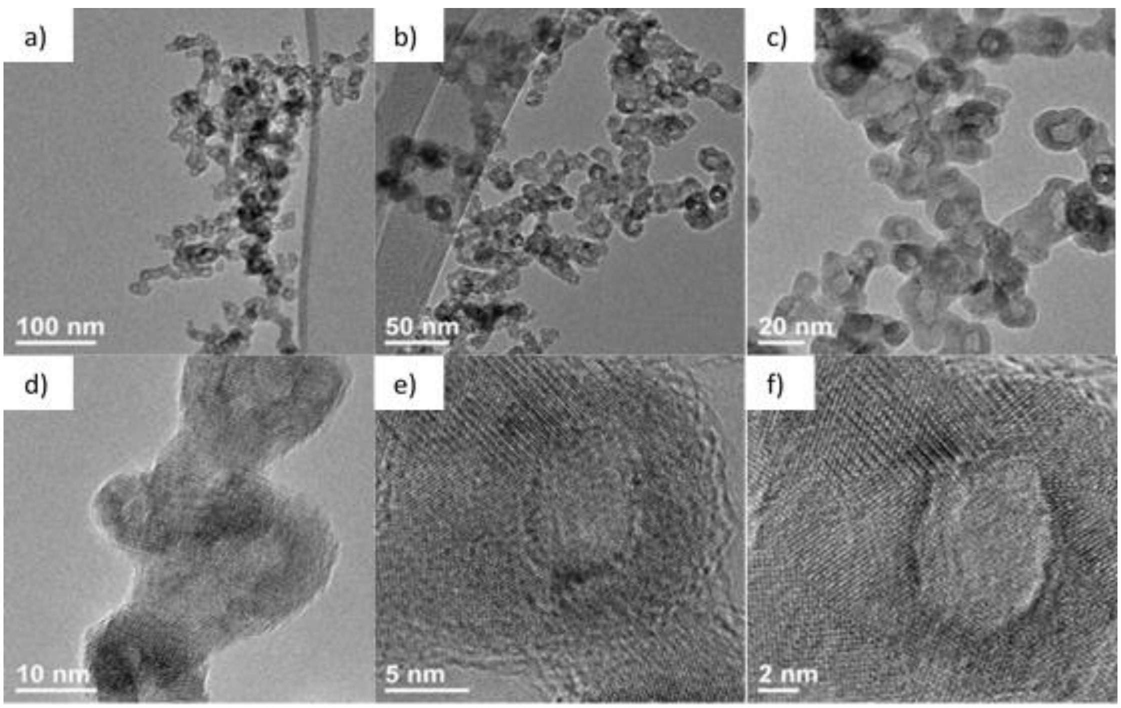

Figure 4-2: High resolution Transmission Electron Microscopy of $NiFe_2O_4$ NPs grown in IGC and annealed at 300°C for 0.5 hours at different resolutions: a), b), and c) low magnification bright field micrographs of the sample show hollow nanoparticles with varying sizes and void diameters; d), e), and f) high magnification bright field micrographs confirm polycrystallinity of the nanoparticles.

Figure 4-2 shows low and high resolution bright field TEM micrographs. The observed NPs particles were hollow, as shown in figure 4-2 (a, b, c). Moreover, high resolution images revealed that NPs were polycrystalline, as also seen in figure 4-2 (d, e, f). Both particle size and voids exhibited size distributions, with particle size varying from 15 to 25 nm. The mechanism by which the voids were formed in the sample annealed at 300^{o}C for 0.5 hours, is known as the Kirkendall effect [15]. Kirkendall stated that two materials of different diffusivities lead to the creation of voids in the material with the highest diffusion rates. In the $Ni_{33}Fe_{67}/NiFe_2O_4$ core/shell NPs, these materials were the metallic alloy, $Ni_{33}Fe_{67}$, from the core and O ions from the surface. Post ex-situ heat treatment was performed to obtain single phase $NiFe_2O_4$ phase. Here, the rate of the inward diffusion of oxygen during the annealing process was much lower than that of the outward diffusion of $Ni_{0.33}Fe_{0.67}$ [15]. Mismatch in the diffusivity led to the formation of hollow morphology.

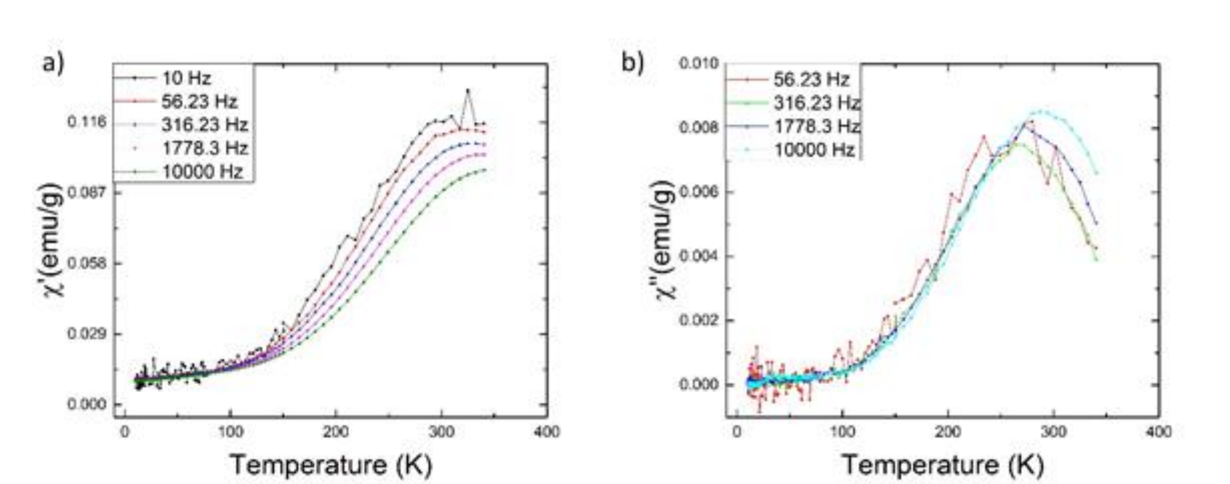

Figure 4-3: AC susceptibility taken at different frequencies for the in-phase, χ', (10 Hz to 10 kHz) and out-phase, χ'', (56.23 Hz to 10 kHz) as a function of temperature, with a 5 Oe applied AC field.

4.5 Magnetic Properties

AC susceptibility (ACS) measurements were carried out. Both the in-phase (χ') and out-of-phase part (χ'') of ACS are shown in figure 4-3 (a) and (b), respectively. The χ' as a function of temperature was measured in AC field with frequency ranging from 10 Hz to 10 kHz and a magnitude of 5 Oe whereas for χ'' the frequency ranged from 56.23 Hz to 10 kHz. For both cases a shift in the peak, which lies around room temperature, was observed with applied frequency. The shift was more pronounced for χ''. The frequency dependence shift of the peak has been reported to be present in NPs exhibiting SPM to ferromagnetic (FM) transition [14,17,18] and SG transition [7,14,17,19]. The broad nature of these peaks indicates a size distribution of crystals integrated in the particles, as observed in the TEM measurements. In addition to size distribution, dipolar and exchange interaction between them also contributes to the peak broadening.

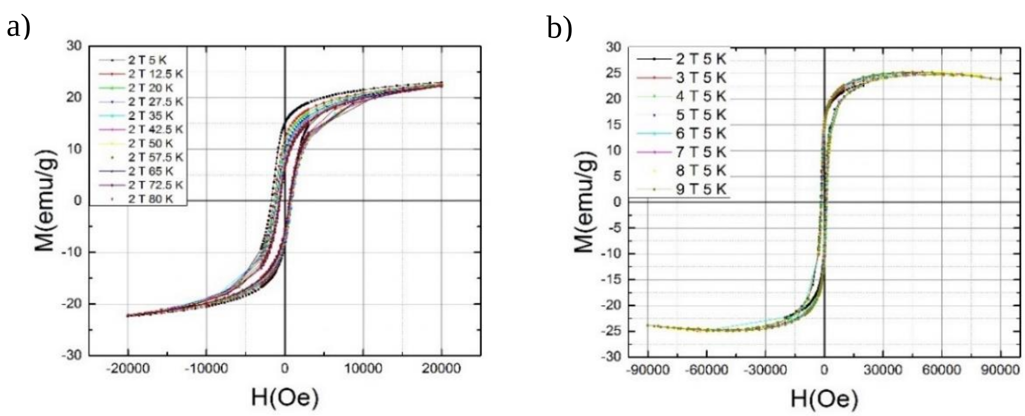

Figure 4-4: Hysteresis loops of NiF_2O_4 NPs recorded at a) different temperatures with a cooling field of 2 T, and b) at different cooling fields at 5 K.

Figure 4-4, shows field cooled (FC) hysteresis loops. FC hysteresis loops recorded in cooling field (H_{CF}) of 2 T and measured at temperatures (5 to 80 K), are shown in figure 4-4(a). To observe the effects of H_{CF} on coercivity (H_C) and EB, FC loops were also recorded at 5 K while changing H_{CF} from 2 T to 9 T. From the temperature dependent loops (figure 4-4(a)), relatively high H_C was observed. Furthermore, the NPs lacked magnetic saturation. The lack of saturation of the loops observed was an obvious evidence of the presence of disordered surface spins [14,32,33]. This can be explained by the surface truncation and broken bonds which causes the system to lack bulk-like spins arrangement [15]. The interaction between the disordered surface spins and FiM phase gave rise to higher H_C and EB. EB rises in magnetic systems where FiM phase is coupled to the SG [7,32,33] or AFM phases [14]. In the higher H_{CF}, figure 4-4(b), decreasing trend in the magnetization was due to the increase in the background diamagnetic signal. To further analyze these changes, H_C and EB values were extracted and plotted in figure 4-5.

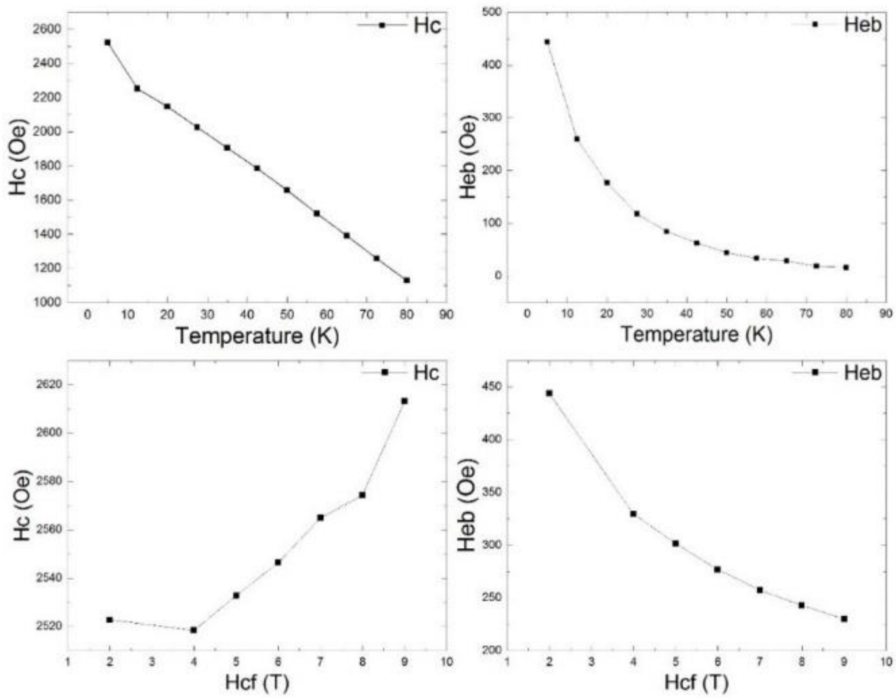

Figure 4-5: Extracted coercivity and exchange bias values from the recorded hysteresis loops. The top left plot shows the coercivity fields of the loops at different temperatures after the sample was cooled to the said temperature in the presence of a 2 T field; top right plot shows the exchange bias of the loops at different temperatures after the sample was cooled to the said temperature in the presence of a 2 T field; the bottom left plot shows the coercivity field of the loops at different cooling fields while at 5 K; and the bottom right plot shows the exchange bias of the loops under different cooling fields while at 5 K.

In figure 4-5, it was observed that H_C decreased linearly with increasing temperature, from 2522 Oe to 1128 Oe as temperature increased from 5 to 80 K, in H_{CF} which was 2 T. The EB also decreased almost exponentially from 444 Oe to 16 Oe as the temperature increased from 5 to 80 K. The fact that both H_C and EB decreased with increasing temperature indicated a weakening of coupling between the FiM and the disordered surface spins, as the disordered surface spins became less stable at high temperatures. Also, the EB did not completely vanish even at 80 K, which indicated presence of stabilized disordered surface spins, compare to other studies where the EB have been seen to vanishes above 50 K [5,20]. Hence these findings indicated a presence of robust disordered surface spins which were particularly more stable in particles with hollow morphology.

H_C was observed to have an opposite trend in the case of the changes in H_{CF}. H_C increased from 2522 Oe to 2613 Oe as H_{CF} increased from 2 T to 9 T. EB decreased from 444 Oe to 230 Oe as H_{CF} increased from 2 T to 9 T. Decrease in EB with H_{CF} can be due to the increased degree of alignment of the disordered surface spins as a function of H_{CF} [11]. While increase in H_C with H_{CF} arises due to the increase in the spin alignment at the integrated crystal interfaces within the particles.

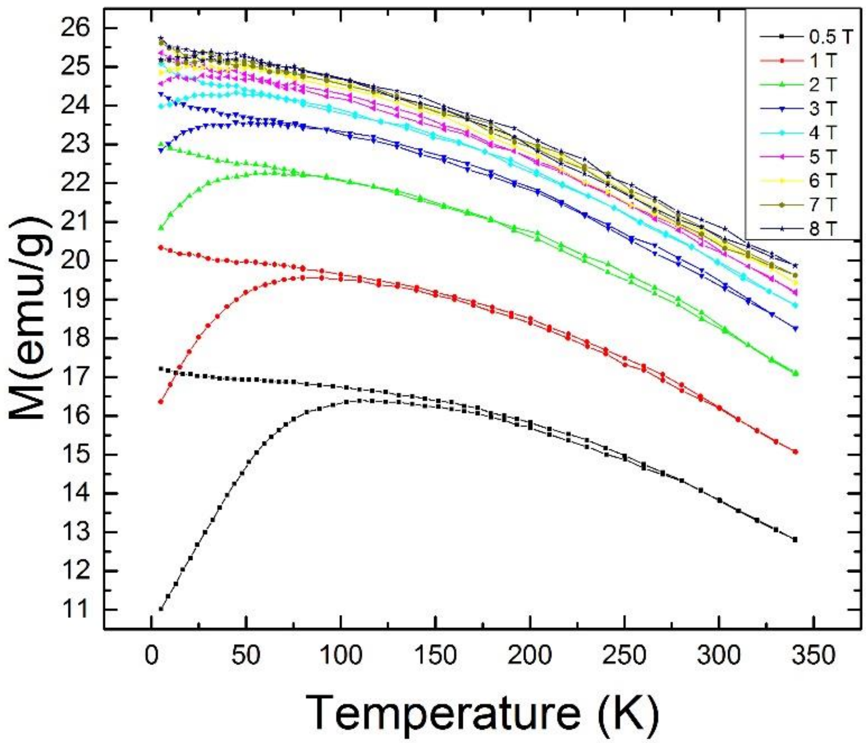

Figure 4-6: Magnetization as a function of temperature at different cooling field of the $NiFe_2O_4$ NPs annealed 300°C for 0.5 hours.

Zero field cooled (ZFC) and FC temperature dependent measurements in wide range of cooling fields (from 0.5 T to 8 T) were carried out. Figure 4-6 shows the ZFC and FC curves that were obtained by first cooling the sample from room temperature to 5 K in the absence of a field and measuring the magnetic dependence from 5 K to 300 K. Once at 300 K, the sample was cooled back down in the presence of a field (starting with 0.5 T) to 5 K, before recording the magnetization as temperature was increased to 300 K, again. This process was repeated for all the different collected magnetization dependent measurements, up to 8 T. In the case of bulk $NiFe_2O_4$, irreversibility in the FC and ZFC curves are known to be wiped away in few hundred Oe of fields [20]. From figure 4-6, as the H_{CF} was increased, the irreversibility temperature was observed to decrease form 110 K at 0.5 T to about 14 K at 5 T, and then remained fairly constant up to 8 T, and irreversibility remained non-zero up to the highest H_{CF}. These observations indicate presence of a disordered surface spins whose interaction with the FiM components yielded irreversibility and system behaved differently compared to the bulk counterpart. These findings are consistent with the reported irreversibility observed in magnetic NPs arising due to the strong coupling between FiM and disordered surface spins [7,13,14,27,32,33,39].

The morphology of the $NiFe_2O_4$ sample annealed at 300°C for 0.5 hours, which was observed to be hollow and polycrystalline in nature with varying particle and void size, has been attributed to the reason behind the magnetic properties described above. In hollow NPs, the addition of inner surface increased the surface to volume ratio, which led to non-vanishing irreversibility at high cooling field. In contrast to solid NPs of $NiFe_2O_4$, the EB and H_C persisted up to 80 K in the hollow polycrystalline NPs. The persistence of these two parameters as temperature was increased can be linked to the morphology of the sample as well [14]. The polycrystallinity, in addition to hollow structure, of the sample add an extra coupling at the interface of FiM and the disordered surface spins [5,32,33,40].

4.6 Conclusion

Detailed magnetic response of hollow polycrystalline $NiFe_2O_4$ nanoparticles is presented. The particles exhibit size distribution, which is manifested in the broad blocking/unblocking transition, as observed using AC susceptibility measurements. Polycrystalline nature and additional inner surface in the hollow nanoparticles led to the observation of drastically different magnetic response, in comparison with the bulk counterpart. These results were explained in terms of enhanced stabilized disordered surface spins. The presence of disordered surface spins led to high coercivity, exchange bias and high field magnetic irreversibility. Extracted coercivity and exchange bias values from temperature and cooling field dependent loops indicated strong ferrimagnetic and disordered surface spins coupling. Coercivity decreased from 2522 Oe to 1128 Oe when the temperature was varied from 5 K to 80 K in a 2 T field. However, the coercivity increased from 2522 Oe at 2 T to 2613 kOe at 9 T. The exchange bias was found to decrease in both the temperature and field dependent measurements where the trend was opposite from the trend of the coercivity. For the temperature dependent measurement, the exchange bias decreased from 444 Oe to 16 Oe when the temperature was varied from 5 K to 80 K whereas it only decreased to 230 Oe when the field was changed to 9 T at 5 K. Irreversibility was found to persist at low temperature as the cooling field was changed from 0.5 T to 8 T. The increase in coercivity as the cooling field was increased, the lack of vanishing coercivity with changing temperature, the non-vanishing of the exchange bias as temperature was increased to 80 K, and the non-vanishing irreversibility of the sample, are all indicative of a strong coupling between the ferrimagnetic phase and the disordered surface spins.

REFERENCES

[1] R.. Kodama, Magnetic nanoparticles, J. Magn. Magn. Mater. 200 (1999) 359–372. doi:10.1016/S0304-8853(99)00347-9.

[2] S. Sun, C.B. Murray, D. Weller, L. Folks, A. Moser, Monodisperse FePt nanoparticles and ferromagnetic FePt nanocrystal superlattices, Science (80-.). 287 (2000) 1989–92. doi:10.1126/science.287.5460.1989.

[3] T. Theivasanthi and M. Alagar, Anti-bacterial Studies of Silver Nanoparticles, Arxiv Prepr. arXiv1110.1372. (2011). http://arxiv.org/abs/1110.1372 (accessed July 3, 2012).

[4] P. Tartaj, P. Morales, S. Veintemillas-verdaguer, T. Gonz, The preparation of magnetic nanoparticles for applications in biomedicine, 36 (2003).

[5] V. Skumryev, S. Stoyanov, Y. Zhang, Beating the superparamagnetic limit with exchange bias, Nature. 423 (2003) 19–22. doi:10.1038/nature01750.1.

[6] M.E. Mchenry, Nano-scale materials development for future, 48 (2000).

[7] R.H. Kodama, A.E. Berkowitz, E.J. McNiff, Jr., S. Foner, Surface Spin Disorder in $NiFe_2O_4$ Nanoparticles, Phys. Rev. Lett. 77 (1996) 394–397. doi:10.1103/PhysRevLett.77.394.

[8] S. Wei, Q. Wang, J. Zhu, L. Sun, H. Lin, Z. Guo, Multifunctional composite core-shell nanoparticles., Nanoscale. 3 (2011) 4474–502. doi:10.1039/c1nr11000d.

[9] T. Gaudisson, R. Sayed-Hassan, N. Yaacoub, G. Franceschin, S. Nowak, J.-M. Grenèche, On the exact crystal structure of exchange-biased Fe_3O_4–CoO nanoaggregates produced by seed-mediated growth in polyol, CrystEngComm. 18 (2016) 3799–3807. doi:10.1039/C6CE00700G.

[10] G. Hassnain Jaffari, S. Rizwan Ali, S.K. Hasanain, G. Güntherodt, S. Ismat Shah, Stabilization of surface spin glass behavior in core-shell $Fe_{67}Co_{33}$–$CoFe_2O_4$ nanoparticles, J. Appl. Phys. 108 (2010) 63921. doi:10.1063/1.3478738.

[11] M.A. Bah, G.H. Jaffari, F.A. Khan, S.I. Shah, Surfaces and their effect on the magnetic properties of polycrystalline hollow γ-Mn_2O_3 and MnO nanoparticles, Appl. Surf. Sci. 375 (2016) 136–143. doi:10.1016/j.apsusc.2016.02.145.

[12] H. Khurshid, W. Li, M.H. Phan, P. Mukherjee, G.C. Hadjipanayis, H. Srikanth, Surface spin disorder and exchange-bias in hollow maghemite nanoparticles, Appl. Phys. Lett. 101 (2012) 1–6. doi:10.1063/1.4733621.

[13] H. Khurshid, P. Lampen-Kelley, Ò. Iglesias, J. Alonso, M.-H. Phan, C.-J. Sun, M.-L Saboungi, H. Srikanth, Spin-glass-like freezing of inner and outer surface layers in hollow γ-Fe_2O_3 nanoparticles., Sci. Rep. 5 (2015) 15054. doi:10.1038/srep15054.

[14] R.J. Tackett, A.W. Bhuiya, C.E. Botez, Dynamic susceptibility evidence of surface spin freezing in ultrafine NiFe2O4 nanoparticles., Nanotechnology. 20 (2009). doi:10.1088/0957-4484/20/44/445705.

[15] G.H. Jaffari, A. Ceylan, C. Ni, S.I. Shah, Enhancement of surface spin disorder

in hollow NiFe2O4 nanoparticles, J. Appl. Phys. 107 (2010) 13910. doi:10.1063/1.3277041.

[16] Z. Nemati, H. Khurshid, J. Alonso, M. H. Phan, P. Mukherjee, H. Srikanth, From core/shell to hollow Fe/ γ-Fe_2O_3 nanoparticles: evolution of the magnetic behavior, Nanotechnology. 26 (2015) 405705. doi:10.1088/0957-4484/26/40/405705.

[17] S.D. Tiwari, K.P. Rajeev, Signatures of spin-glass freezing in NiO nanoparticles, Phys. Rev. B. 72 (2005) 104433. doi:10.1103/PhysRevB.72.104433.

[18] O. Ni, A. Bajpai, A. Banerjee, Superparamagnetism in polycrystalline Li 0.5 Ni 0.5 O samples: Low-field susceptibility measurements, 62 (2000) 8996–9004.

[19] M. Coşkun, M. Korkmaz, T. Fırat, G.H. Jaffari, S.I. Shah, Synthesis of SiO_2 coated $NiFe_2O_4$ nanoparticles and the effect of SiO_2 shell thickness on the magnetic properties, J. Appl. Phys. 107 (2010) 09B523. doi:10.1063/1.3359426.

[20] R.H. Kodama, A.E. Berkowitz, E.J.M. Jr, S. Foner, Surface spin disorder in ferrite nanoparticles (invited) Surface spin disorder in ferrite nanoparticles (invited), J. Appl. Phys. 5552 (1997) 3–9. doi:10.1063/1.364659.

[21] M. Kiwi, J. Mejia-Lopez, R.D. Portugal, R. Ramirez, Exchange bias theory: The role of interface structure and of domains in the ferromagnet, in: J.L. MoranLopez (Ed.), Phys. LOW Dimens. Syst., 2001: pp. 295–300. doi:0-306-46566-3.

[22] B. Martínez, X. Obradors, L. Balcells, A. Rouanet, C. Monty, Low Temperature Surface Spin-Glass Transition in γ-Fe_2O_3 Nanoparticles, 80 (1998).

[23] P. Ayyub, M. Multani, M. Barma, Size-induced structural phase transitions and hyperfine properties of microcrystalline Fe_2O_3, J. Phys. C 21 (1988) 2229–2245. http://iopscience.iop.org/0022-3719/21/11/014.

Chapter 5

POLYCRYSTALLINE HOLLOW γ-Mn_2O_3 AND MnO NANOPARTICLES: STUDY OF COUPLING BETWEEN FiM AND AFM PHASES IN ADDITION TO SURFACE EFFECT ON THE EXCHANGE BIAS AND MAGNETIC IRREVERSIBILITY

5.1 Abstract

Magnetic properties of polycrystalline hollow γ-Mn_2O_3 and MnO are presented. Strong coupling between γ-Mn_2O_3 and MnO phases along with the additional inner surface of the nanoparticles lead to large coercivity (H_C) and exchange bias (EB) fields, up to 11 kOe and 7 kOe, respectively, below the order temperatures. H_C and EB were found to increase and decrease, respectively, as a function of cooling field. Both H_C and EB were found to decrease monotonically as the temperature approached paramagnetic phase transition of the ferrimagnetic component.

5.2 Introduction

There have been several reports on magnetic nanoparticles where morphologies, such as core/shell, hollow, solid etc., were varied and their effect on the magnetic response was studied [1–6]. Core/shell nanoparticles with various ferromagnetic (FM), ferrimagnetic (FiM) and antiferromagnetic (AFM) core and shell combinations have been reported [1,4,5]. In these cases, interesting and strikingly different features, such as unusually high spin glass transition temperature [4], large exchange bias [4,6], finite size effects [5], magnetic proximity effects [7], and unusual trend of blocking temperature as a function of average crystal size [1] , have been reported. The spin glass (SG) and AFM components play an important role in spintronic devices [1,8] where their presence likely helps to overcome the superparamagnetic limit in recording media and/or enhance the coercivity of ferromagnets [2,9–11]. Specifically, core/shell morphology provides added degrees of freedom, including size, phase and material of the core and shell of the particle, etc. [4,5,12–14]. In the case of inverted core/shell morphology, FiM order above the Curie temperature (T_C) of the shell have been reported where the Néel temperature (T_N) is comparable with the bulk value [7,15,16] with a nonmonotonic dependence of the coercive field and exchange bias on the core diameter [14].

In addition to the core/shell morphology, nanoparticles with hollow morphology are also of interest. These particles have been shown to have drastic enhancement in their catalytic properties [17–19], unique behavior as colloid particle suspension in electrorheological fluids [20], and enhanced performance as electrodes [21]. In the case of magnetic properties, surface spin glass transition enhancements have been reported due to the presence of the additional inner surface [1,22]. $NiFe_2O_4$ and γ-Fe_2O_3 hollow nanoparticles exhibited strikingly contrasting magnetic behavior compared to bulk and conventional solid particles [1,22]. Structurally, hollow polycrystalline nanoparticles are composed of multiple crystallographic domains. This random orientation of the crystallographic domains also causes randomization of the local anisotropy axes. Hence the overall effect of this morphology on the magnetic properties is exhibited through the high coercivity, relatively high temperature magnetic irreversibility, lack of magnetic saturation, high blocking temperature, etc. [1,4,22]. Over the years, Fe and Co based core/shell nanostructures were studied extensively for their exchange bias phenomenon. Various manganese oxide (Mn-oxide) core/shell nanoparticles have also been studied and their inverted core/shell structure, large coercivities, exchange bias or enhanced anisotropy, bulk Néel temperatures of the core and the proximity effects have been reported [7,14–16]. However, there is almost negligible amount of results reported on the synthesis and magnetic behavior of hollow nanoparticles of Mn-oxide system.

This chapter presents results of the study of hollow Mn-oxide nanoparticles where particles are polycrystalline and have both MnO (AFM), and γ-Mn_2O_3 (FiM) crystallites coexisting within these particles forming a nanocomposite with overall hollow nanoparticle morphology. Various techniques, including X-ray diffraction (XRD), high resolution transmission electron microscopy (HRTEM), X-ray photoelectron spectroscopy (XPS), AC susceptibility and DC magnetometry were employed to characterize these particles.

5.3 Experimental Section

Mn-oxide nanoparticles were synthesized in an inert gas condensation (IGC) system. Nanoparticle growth by IGC was discussed in chapter 2. Briefly, manganese pieces were placed in an aluminum oxide (Al_2O_3) coated tungsten boat and held in place with a perforated molybdenum sheet with holes to help keep the manganese pieces in place and still allow the evaporated vapors to escape. The boat was then resistively heated by slowly increasing the power from the heating source. The system was first evacuated to a base pressure of about 5 x 10^{-6} Torr, then pressurized to 50 Torr with helium, which was then circulated inside the chamber by a rootsblower pump during evaporation. Helium is used as the carrier gas to carry the evaporated particles to a collecting filter, which was kept at room temperature. Helium has the highest thermal conductivity compared to the other noble gases, which helps in the fast cooling of the vapors which leads to a more uniform particle size. After the synthesis, the system was slowly brought to the atmospheric pressure by back-flowing ambient air, which causes oxidation of manganese (Mn) nanoparticles. X-ray diffraction (XRD) and high resolution transmission electron microscopy (HRTEM) were used to study the structural properties of the prepared Mn-oxide nanoparticles. The Bruker D8 Discover X-ray diffractometer with a Cu K_{α} radiation source was used for the XRD analyses, while the JEOL 2010FX electron microscope with an accelerating voltage of 200 kV was used for the HRTEM studies. Magnetic properties of the nanoparticles were investigated using the physical property measurement system (PPMS) from Quantum Design. X-ray photoelectron spectroscopy (XPS) with an Al K_{α} X-ray source, 0.85 eV resolution, from Omicron was utilized to investigate the chemical nature of the prepared sample. The chemical peaks obtained were corrected with respect to the C 1s peak at 284.6 eV to account for charging.

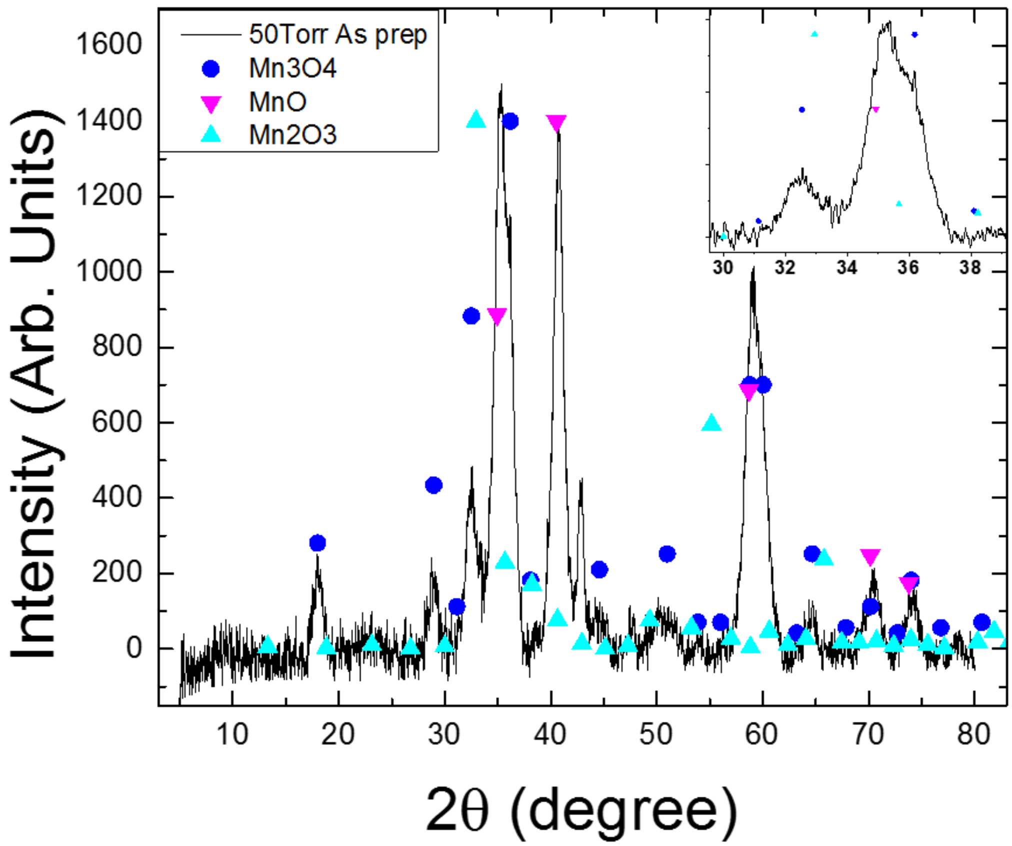

Figure 5-1: X-ray diffraction patter of Mn-oxide nanoparticles.

5.4 Structural and Morphological Studies

The crystal structure and phase analyses were carried out by XRD. A typical diffraction pattern is shown in figure 5-1 obtained from the as-prepared Mn-oxide nanoparticles. The XRD pattern revealed that the powdered sample has a polycrystalline structure with the presence of multiple phases, as identified by using different crystal structures of the phases. Four of the most stable Mn-oxides PCPDF cards (01-075-6876, 00-002-0567, 00-076-0150 and 00-002-0567) were matched against the obtained pattern of the prepared Mn-oxide nanoparticles. Mn-oxide exhibits multiple phases, of which MnO, Mn_3O_4, γ-Mn_2O_3, and MnO_2 are the most stable due to the presence of various valence states of manganese ions, i.e. Mn^{+2}, Mn^{+3} and Mn^{+4} [24]. Peak positions and their relative intensities were analyzed and all the possible oxides are labeled on the XRD pattern in figure 5-1 where it is shown that only three of the four oxides matched the collected Mn-oxide pattern. Previously, it had been reported that the presence of a particular oxide depends on the synthesis procedure [25–27]. As shown in figure 5-1, the most dominant phases are MnO and γ-Mn_2O_3/ Mn_3O_4, since their PCPDF cards match with the collected Mn-oxide pattern. The most intense expected peaks of MnO_2 were not observed in the XRD pattern of the prepared Mn-oxide sample, therefore MnO_2 was counted out as a possible oxide. However, it is not possible to distinguish between Mn_3O_4 and γ-Mn_2O_3 phases from XRD alone due to the proximity of their peak positions combined with the broad nature of the peaks of the prepared Mn-oxide nanoparticles. XPS was used to distinguish between Mn_3O_4 and γ-Mn_2O_3.

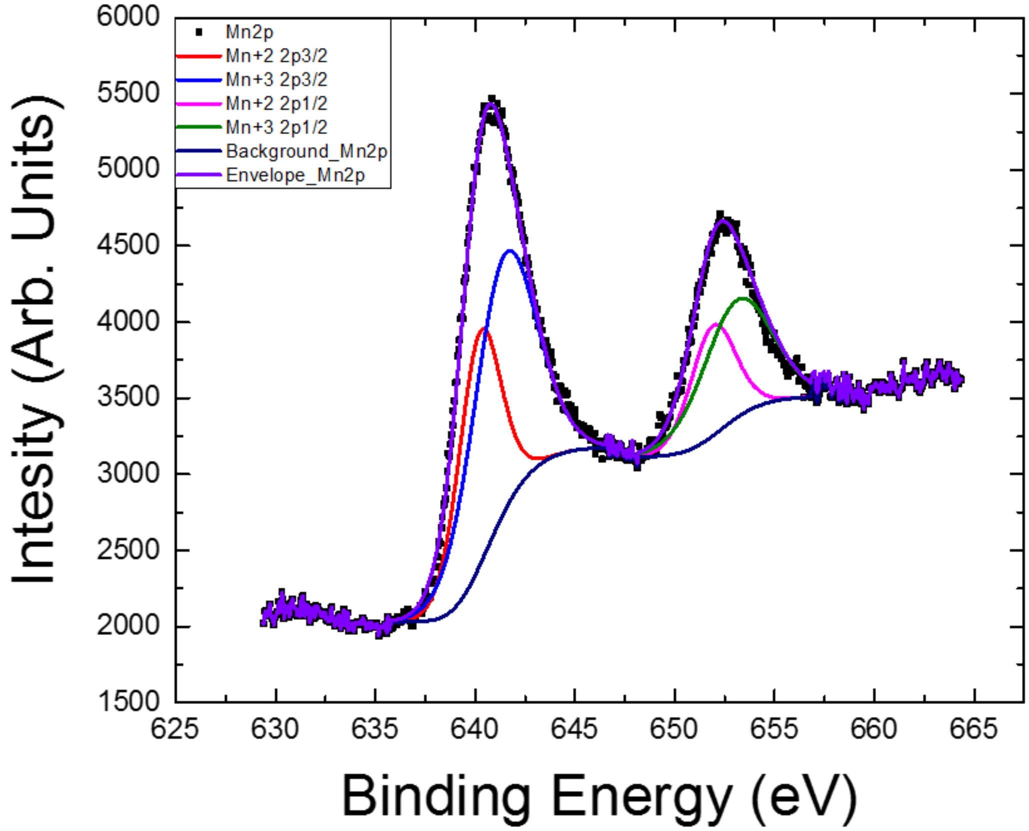

Figure 5-2: X-ray photoelectron spectrum of Mn-oxide nanoparticles showing the high resolution 2p region of Mn.

Figure 5-2 shows the X-ray photoelectron spectrum of the high resolution 2p region of Mn. The deconvolution of the spectrum in figure 5-2 yielded peaks located at 640.2 eV and 641.4 eV. These binding energies are well within ranges of values reported for the +2 and +3 valence states of manganese [28–31]. The presence of Mn^{2+} from the deconvolution of the XPS 2p regions confirms the presence of MnO, whereas the presence of Mn^{3+} is indicative of γ-Mn_2O_3. The quantification of the data was done with a Shirley background correction. From the quantitative analysis, it was calculated that Mn^{3+} is the dominant oxidation state with a concentration of 62.4% and the second most dominant state, Mn^{2+}, at a concentration of 37.6%. The lack of Mn^{4+} indicates that there is no MnO_2, as also concluded from XRD results described earlier. Because Mn_3O_4 has mixed valency, Mn^{3+} and Mn^{4+}, we can conclude that there's no Mn_3O_4 in the sample. Therefore, γ-Mn_2O_3 is the oxide present in the prepared Mn-oxide sample.

Figure 5-3 shows high resolution transmission electron micrographs of the prepared Mn-oxide sample. Various magnifications of the bright field images confirmed the hollow structure of the prepared sample, where hollow nanoparticles ranged from 15 nm to 30 nm in diameter with different void sizes (figures 5-3a and 5-3b). Figure 5-3c shows a high magnification bright field image of the prepared Mn-oxide sample, highlighting the hollow nanoparticles of different diameters. From high resolution images, nanoparticles are found to be polycrystalline, since the observed crystallites are short and randomly oriented. Post-deposition oxidation of these particles stabilizes more than one phase with inward diffusion of oxygen occurring at slower rate compared to the faster outward diffusion of metal. This mechanism is known as the Kirkendall effect [1,22]. Both factors lead to the formation of polycrystalline hollow nanoparticles. The orientation and the spacing of the planes are highlighted in figure 5-3d. The lattice spacing measurements show that there are MnO (0.49 nm lattice spacing) and γ-Mn_2O_3 (0.27 nm lattice spacing) phases present in the sample [14,32]. These findings agree with the XRD and XPS measurements. However, distinction between the γ-Mn_2O_3 and Mn_3O_4 phases is still unclear and will be discussed further later. It should be noted that although single phase polycrystalline γ-Fe_2O_3 [22] and $CoFe_2O_4$ hollow nanoparticles have previously been reported [6]. Here, we have polycrystalline multiphase hollow nanoparticles where particles themselves form a FiM and AFM nanocomposite. The size of crystallites within individual particles is less than 10 nm.

5.5 Magnetic Properties

MnO and MnO_2 are AFM with a bulk AFM transition temperature (Néel temperature (T_N)) of 116 K and 92 K, respectively. However, in the case of small nanoparticles it has been shown that T_N values, that are typically higher than the bulk T_N values, decrease as a function of particle size[32]. The reported T_N values ranging from 139 K to 126 K with particle size change from 4.3 nm to 3.8 nm for MnO. Bulk γ-Mn_2O_3 and Mn_3O_4 are FiM and have bulk transition temperature (Curie temperature (T_C)) of 39 K and 42 K, respectively [33].

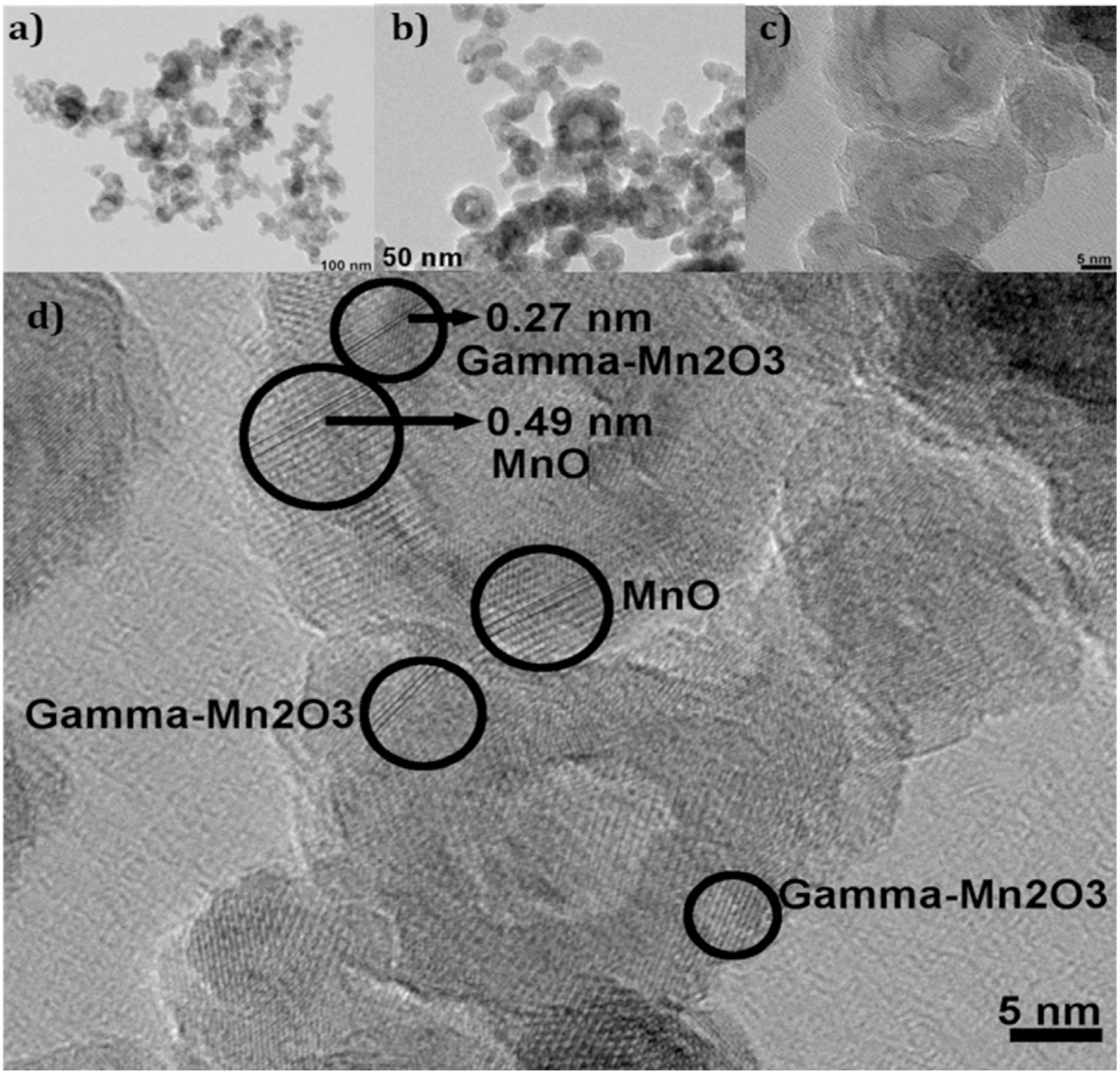

Figure 5-3: High resolution transmission electron micrographs of Mn-oxide nanoparticles: a) and b) show multiple hollow nanoparticles ranging from 15 nm to 30 nm in size with a distribution in void sizes, c) high magnification bright field micrographs highlighting the hollow polycrystalline structure of the nanoparticles with various diameters, and d) highlights the orientation, spacing and size of the different phases.

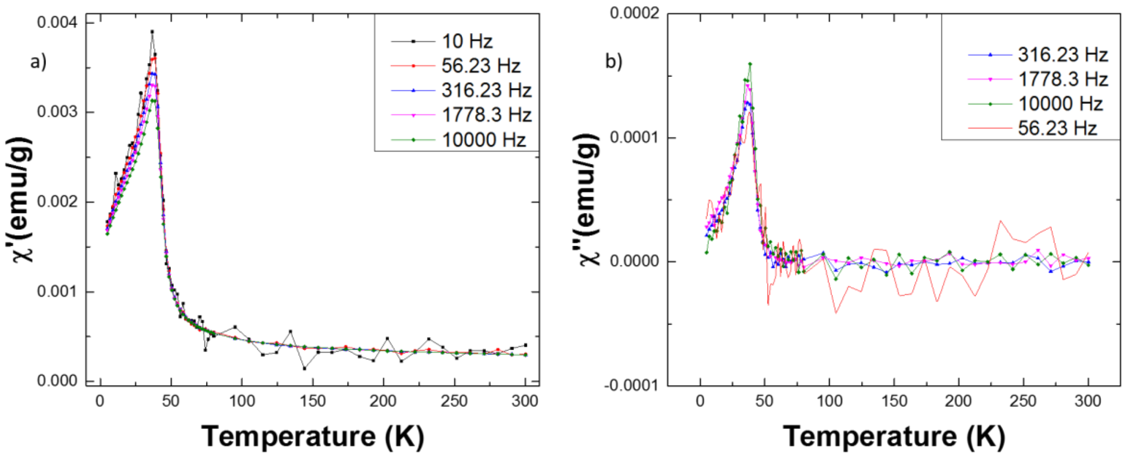

Figure 5-4: Temperature dependence of a) in-phase, χ', and b) out-of-phase, χ'', AC susceptibility at difference frequencies.

Figure 5-4 shows the real ($\chi^{'}$) and imaginary ($\chi^{''}$) part of the susceptibility measured at different frequencies (from 56.23 Hz to 10000 Hz) while applying an AC field of 10 Oe on the prepared Mn-oxide sample. A transition peak at 38 K, near the T_C of γ-Mn_2O_3 for both $\chi^{'}$ and $\chi^{''}$ was observed, indicating the transition is thermodynamic [33,34]. Lopez-Ortega et al. reported reorientation temperature around 20 K and 36 K [33] for different core/shell sizes. We did not observe transitions associated with the reorientation temperature. These reorientation transitions have been reported in single crystal Mn_3O_4 [35]. Therefore, we can conclude that ferrimagnetism mainly comes from γ-Mn_2O_3 rather than Mn_3O_4. Similar conclusions were drawn by Lopez-Ortega et al. where they proved it using more sophisticated techniques such as electron energy lost spectroscopy (EELS) and neutron diffraction. The lack of reorientation transitions at 20 K and 36 K support claims already made from XPS measurement that only γ-Mn_2O_3 is present in our prepared Mn-oxide sample.

The magnetic behavior of the sample as a function of temperature, both for the zero field cooled (ZFC) and field cooled (FC) branches measured in different cooling fields (H_{CF}), are shown in figure 5-5. It is observed from figure 5-5 that the maximum of the ZFC curve occurs around 33 K for the lowest H_{CF} (0.1 T), which marks the onset of thermal activation overcoming the energy barrier. This temperature is referred to as T_{max}. The behavior shown here agrees with results presented by Lopez-Ortega et al. and Seo et al. [33,36]. They reported the same behavior with a T_{max} between 33 K and 41 K for core/shell particles with size ranging from 5 nm to 10 nm for the AFM phase (MnO) and about 5 nm for the FiM phase. These critical transitions take place below 50 K for the sample cooled at various H_{CF} from 0.1 T to 6 T field (more specifically below the T_C of γ-Mn_2O_3, 39 K). At the higher H_{CF}, the T_{max} decreases, reaching 6 K at 6 T H_{CF}. At low temperature, below the T_C (38 K), it is observed that the irreversibility vanishes around 5 T H_{CF}. This is seen in figure 5-5, where the difference in magnetization between the FC and ZFC measurements vanishes. As the H_{CF} increases the irreversibility temperature, where FC and ZFC curves separate, decreases. For 5 T and 6 T H_{CF}, the irreversibility vanishes. The persistence of the magnetization above the T_C is consistent with the proximity effect [7,15], where it is said that the FiM and the AFM phases are coupled well above the T_C. The observed irreversibility at low temperature has been attributed to spin freezing at high H_{CF}

[37,38]. Therefore, the increase in extra inner surfaces in hollow nanoparticles play a major role in the irreversibility which remain intact in significantly high fields.

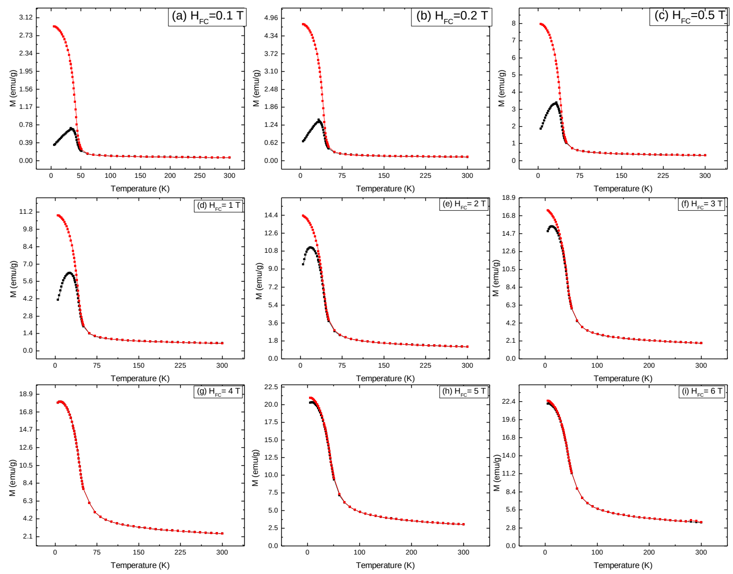

Figure 5-5: Magnetization vs temperature curves of the Mn-oxide nanoparticles at different applied and cooling field.

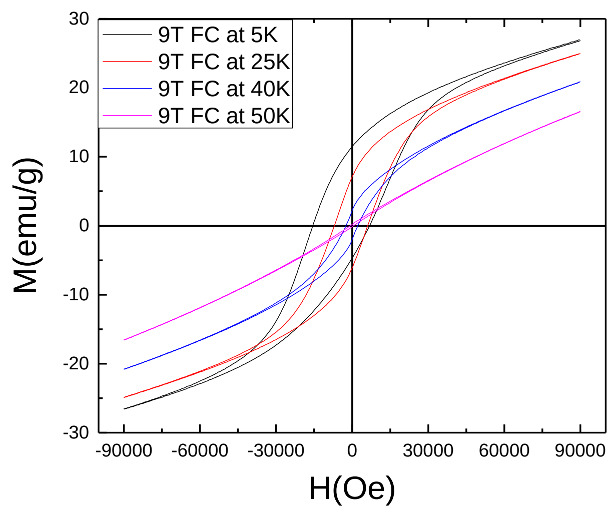

Figure 5-6: Hysteresis loops of Mn-oxide nanoparticles at different temperatures with a cooling field of 9 T.

Hysteresis loops measured from 5 K to 50 K cooled from 300 K in the presence of 9 T H_{CF} are shown in figure 5-6. The observed high saturation magnetization (M_s) of 27 emu/g is much closer to the M_s found in bulk γ-Mn_2O_3, 28 emu/g, rather than the M_s bulk value of Mn_3O_4, 32 emu/g [33]. The absence of peaks associated with reorientation temperature around 20 K and 38 K for Mn_3O_4 and the proximity of the high saturation magnetization value to γ-Mn_2O_3 agrees with our XRD and XPS results. This again confirms that the FiM response arises due to γ-Mn_2O_3. It has also been theoretically shown that the saturation magnetization reduces due to spin freezing as well as finite size effect from experimental studies [39–41]. Here, we observed a gradual decrease in the value of the coercive field (H_C) from 22 kOe to zero as the temperature increases from 5 K to 50 K. Hence at 50 K, paramagnetic behavior is observed. Elsewhere a value of 2.8 kOe was reported as the H_C of the FiM phase [29], nearly a 10^{th} of the aforementioned, 22 kOe H_C, and about a 4^{th} of other reported values [14,29,33,42,43].

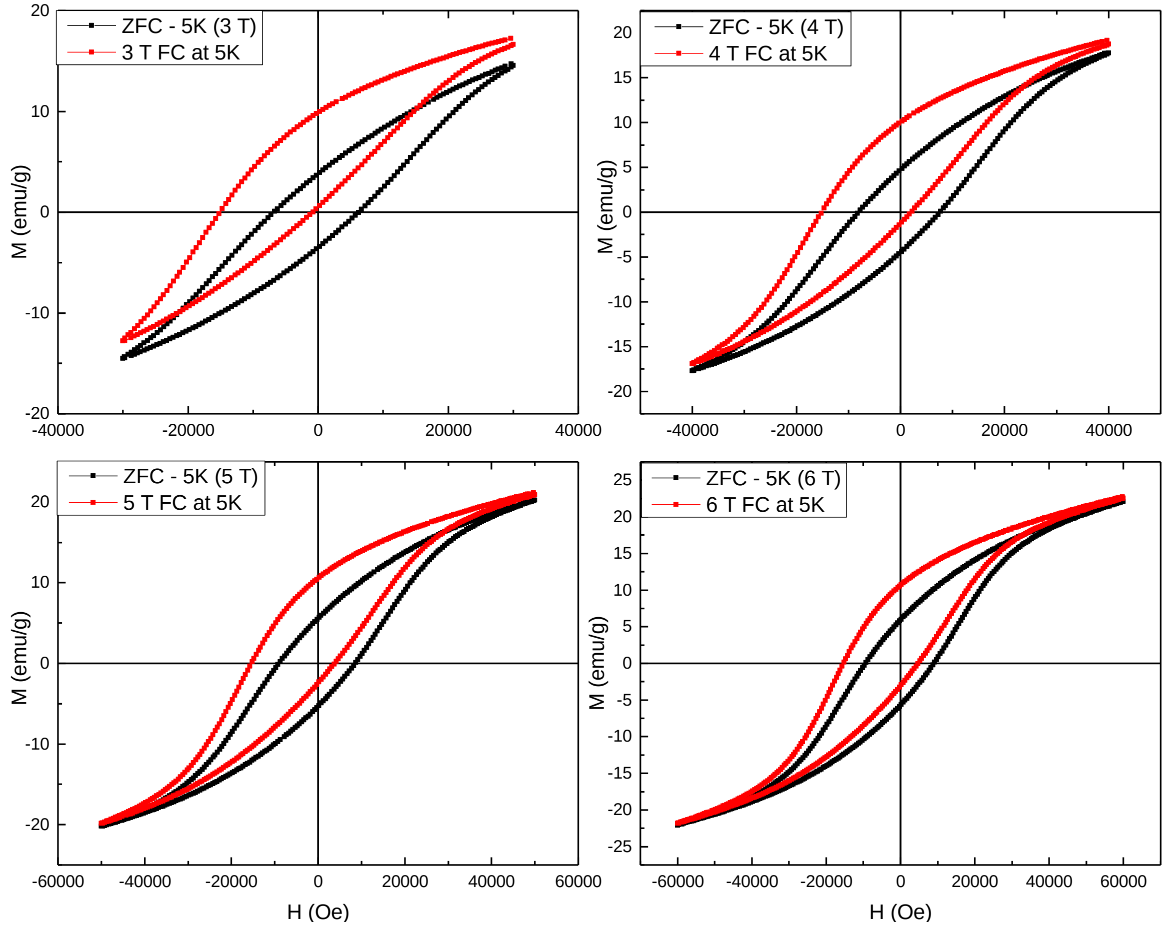

Figure 5-7: Magnetic hysteresis loops of sample at 5 K with different cooling fields along with ZFC loops after cooling the sample to 5 K in a zero applied field from 300 K.

Figure 5-7 shows ZFC and FC hysteresis loops at 5 K with different H_{CF}. Here the sample is first cooled to 5 K in a zero applied field, followed by ZFC loop measurement from 5 K to 300 K to a maximum desired field, i.e. 1 T, then the sample is cooled to 5 K, again while maintaining the field at the aforementioned field, followed by a FC loop measurement from 5 K to 300 K. The field is zeroed again after the FC loop measurement and the sample cooled to 5 K right away, and a ZFC loop is measured to 300 K to a maximum applied field of 1 T higher than the field previously used to record the last FC loop, i.e. 2 T. Therefore, in the case of ZFC, H_{CF} refers to the previous maximum applied field for which the FC loop was recorded. FC loops exhibited noticeable coercivity increase compared to the ZFC loops. This indicates growth of the FiM component due to the presence of H_{CF} while cooling the sample from temperatures larger than the ordering temperature of the FiM phase. The exchange bias EB decreases with increase in the H_{CF}.

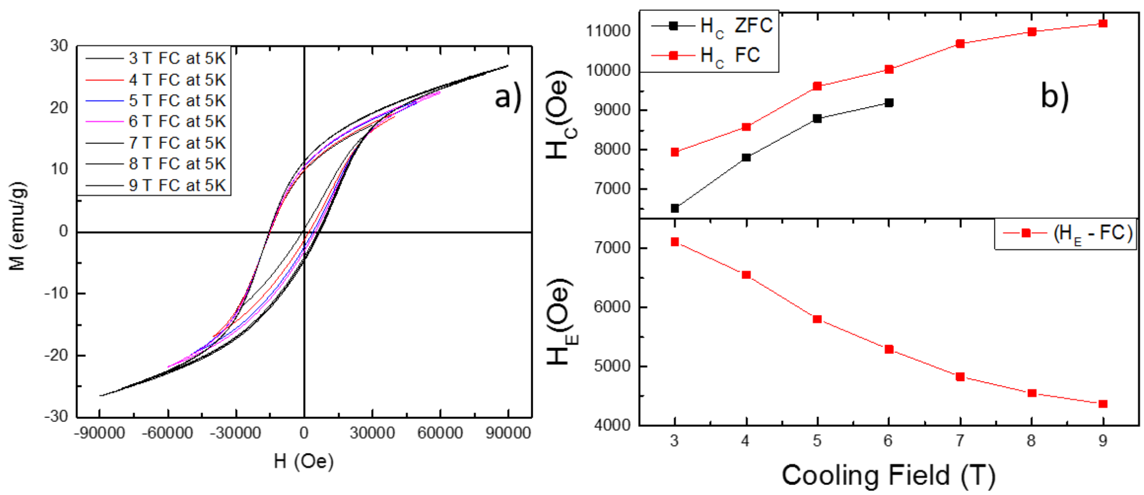

Figure 5-8: Cooling field effect on a) hysteresis loops for the Mn-oxide nanoparticles at 5 K temperature with different cooling fields, and b) coercive field and exchange bias field at different cooling fields.

Measured hysteresis loops at 5 K with various H_{CF} are shown in figure 5-8 a). The EB and the H_C measured for both the ZFC and FC cases as a function of the H_{CF} recorded at 5 K are presented in figure 5-8 b), where noticeable coercivity increase is also observed. H_C is seen to increase with increasing H_{CF}, while the EB decreases with increasing H_{CF}. H_C from the ZFC measurements, not explicitly shown here, exhibited smaller values compared to the FC measurements with the same increasing trend as a function of H_{CF}. Therefore, the degree of alignment of the FiM component improves on field cooling the sample. An increase from 7 kOe to 4.5 kOe for EB was observed by varying H_{CF} from 3 T to 9 T. Magnetization response of the system also revealed decrease in the overall shift of the loop towards the negative field axis. As the negative saturation field increases, the degree of alignment of the FiM spins and AFM/FiM interfacial spins increases, which leads to an increase in the negative remanent magnetization. A similar monotonic increase in the H_C has been observed for the loop recorded in H_{CF} condition, as shown in figure 5-8 b).

These large values, 7 kOe for EB and 11 kOe for H_C, can be explained in terms of the morphology of the nanoparticles as seen in the HRTEM studies. In general, nanoparticles exhibit large surface to volume ratio. For hollow nanoparticles, polycrystalline structure comes with random orientation of multiple crystallographic domains with local anisotropy axes being random as well [6,22]. Therefore, hollow and polycrystalline nanoparticles, like our prepared Mn-oxide nanoparticles, increase the FiM and AFM interface compared to the conventional core/shell nanoparticles which results in large horizontal and vertical shifts, observed in figures 5-7 and 5-9. The hollow structure, also, leads to the reduction of the saturation magnetization compare to the bulk values, as well as the presence of irreversibility in low temperature regime, figures 5-6 and 5-5, respectively. It is also well known that as the particle size decreases below a certain size, FiM becomes superparamagnetic (SPM) [9,44] and both the remanence and coercivity vanishes. However, even very small SPM nanoparticles exhibit non-zero coercivity and remanence when embedded in

AFM matrix [2,9]. Hence all the factors together result in the observed large value of coercivity.

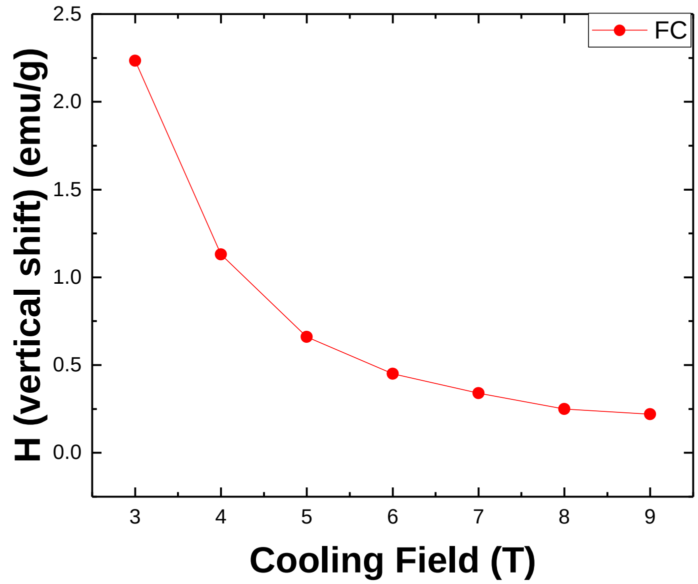

Figure 5-9: Vertical shift dependence on cooling field of the prepared Mn-oxide nanoparticles at 5 K.

5.6 Conclusion

A detailed magnetic study of polycrystalline hollow nanoparticles composed of FiM γMn_2O_3 and AFM MnO crystallites is presented. Both AC and DC magnetic responses in wide range of cooling fields and temperatures revealed strong coupling between the FiM and AFM phases. Decrease in the magnetic irreversibility below the FiM and AFM order temperatures was found to decrease as a function of cooling field. Field cooled (FC) loops exhibited noticeably larger coercivity compared to the zero field cooled (ZFC) loops. This indicates growth of the FiM component due to the presence of cooling field H_{CF} while cooling the sample from temperatures larger than the ordering temperature of the FiM. Compared to the core/shell counter parts, larger coercivity (H_C) and exchange bias (EB) fields up to 11 kOe and 7 kOe, respectively, were observed at low temperature. The large values can be explained in terms of the morphology of the particles as seen in the HRTEM studies. In general nanoparticles exhibit large surface to volume ratio. For hollow nanoparticles, polycrystalline structure comes with random orientation of multiple crystallographic domains with local anisotropy axes being random as well. Hence it increases the FiM and AFM interface compared to the conventional core/shell particles. Overall, it results in large horizontal and vertical shifts.

REFERENCES

[1] G.H. Jaffari, A. Ceylan, C. Ni, S.I. Shah, Enhancement of surface spin disorder in hollow $NiFe_2O_4$ nanoparticles, J. Appl. Phys. 107 (2010) 13910. doi:10.1063/1.3277041.

[2] M. Coskun, G. Hassnain Jaffari, S. Manzoor, M. Korkmaz, S. Ismat Shah, Synthesis and magnetic properties of Co–Cr_2O_3 nanocomposites, J. Magn. Magn. Mater. 322 (2010) 1731–1735. doi:10.1016/j.jmmm.2009.12.016.

[3] M. Coşkun, M. Korkmaz, T. Fırat, G.H. Jaffari, S.I. Shah, Synthesis of SiO_2 coated $NiFe_2O_4$ nanoparticles and the effect of SiO_2 shell thickness on the magnetic properties, J. Appl. Phys. 107 (2010) 09B523. doi:10.1063/1.3359426.

[4] G. Hassnain Jaffari, S. Rizwan Ali, S.K. Hasanain, G. Güntherodt, S. Ismat Shah, Stabilization of surface spin glass behavior in core-shell $Fe_{67}Co_{33}$–$CoFe_2O_4$ nanoparticles, J. Appl. Phys. 108 (2010) 63921. doi:10.1063/1.3478738.

[5] G. Hassnain Jaffari, T. Ekiert, K.M. Unruh, S. Ismat Shah, Effect of particle size distribution on the magnetic properties γ-Fe_2O_3 nanoparticles, Mater. Sci. Eng. B. 177 (2012) 935–941. doi:10.1016/j.mseb.2012.04.016.

[6] G.H. Jaffari, A. Ceylan, H.P. Bui, T.P. Beebe, S. Ozcan, S.I. Shah, Non-equilibrium cation distribution and enhanced spin disorder in hollow $CoFe_2O_4$ nanoparticles., J. Phys. Condens. Matter. 24 (2012) 336004. doi:10.1088/0953-8984/24/33/336004.

[7] I. Golosovsky, G. Salazar-Alvarez, A. López-Ortega, M. González, J. Sort, M. Estrader, S. Suriñach, M. Baró, J. Nogués, Magnetic Proximity Effect Features in Antiferromagnetic/Ferrimagnetic Core-Shell Nanoparticles, Phys. Rev. Lett. 102 (2009) 247201. doi:10.1103/PhysRevLett.102.247201.

[8] J. Nogués, J. Sort, V. Langlais, V. Skumryev, S. Suriñach, J.S. Muñoz, M. D. Baró, Exchange bias in nanostructures, Phys. Rep. 422 (2005) 65–117. doi:10.1016/j.physrep.2005.08.004.

[9] V. Skumryev, S. Stoyanov, Y. Zhang, Beating the superparamagnetic limit with exchange bias, Nature. 423 (2003) 19–22. doi:10.1038/nature01750.1.

[10] J. Sort, S. Suriñach, J. Muñoz, M. Baró, J. Nogués, G. Chouteau, V. Skumryev, G. Hadjipanayis, Improving the energy product of hard magnetic materials, Phys. Rev. B. 65 (2002) 174420. doi:10.1103/PhysRevB.65.174420.

[11] H. Zeng, J. Li, Z.L. Wang, J.P. Liu, S. Sun, Bimagnetic Core / Shell FePt / Fe_3O_4 Nanoparticles, (2004) 3–6.

[12] H. Zeng, J. Li, Z.L. Wang, J.P. Liu, S. Sun, Bimagnetic Core/Shell FePt/Fe3O4 Nanoparticles, Nano Lett. 4 (2004) 187–190. doi:10.1021/nl035004r.

[13] A. H. Habib, C.L. Ondeck, P. Chaudhary, M.R. Bockstaller, M.E. McHenry, Evaluation of iron-cobalt/ferrite core-shell nanoparticles for cancer thermotherapy, J. Appl. Phys. 103 (2008) 07A307. doi:10.1063/1.2830975.

[14] G. Salazar-Alvarez, J. Sort, S. Suriñach, M.D. Baró, J. Nogués, Synthesis and

size-dependent exchange bias in inverted core-shell MnO|Mn_3O_4 nanoparticles., J. Am. Chem. Soc. 129 (2007) 9102–8. doi:10.1021/ja0714282.
[15] A. Berkowitz, G. Rodriguez, J. Hong, K. An, T. Hyeon, N. Agarwal, D. Smith, E. Fullerton, Antiferromagnetic MnO nanoparticles with ferrimagnetic Mn_3O_4 shells: Doubly inverted core-shell system, Phys. Rev. B. 77 (2008) 24403. doi:10.1103/PhysRevB.77.024403.
[16] A. E. Berkowitz, G. F. Rodriguez, J. I. Hong, K. An, T. Hyeon, N. Agarwal, D. Smith, E. Fullerton, Monodispersed MnO nanoparticles with epitaxial Mn_3O_4 shells, J. Phys. D. Appl. Phys. 41 (2008) 134007. doi:10.1088/0022-3727/41/13/134007.
[17] L. Zhang, L. Shi, L. Huang, J. Zhang, R. Gao, D. Zhang, Rational Design of High-Performance $DeNO_x$ Catalysts Based on Mn x $Co_{3-x}O_4$ Nanocages Derived from Metal–Organic Frameworks, ACS Catal. 4 (2014) 1753–1763. doi:10.1021/cs401185c.
[18] D. Zhang, T. Yan, C. Pan, L. Shi, J. Zhang, Carbon nanotube-assisted synthesis and high catalytic activity of CeO_2 hollow nanobeads, Mater. Chem. Phys. 113 (2009) 527–530. doi:10.1016/j.matchemphys.2008.09.052.
[19] W. Liu, T. Deng, L. Feng, A. Xie, J. Zhang, S. Wang, et al., Designed synthesis and formation mechanism of CeO_2 hollow nanospheres and their facile functionalization with Au nanoparticles, CrystEngComm. 17 (2015) 4850–4858. doi:10.1039/C5CE00569H.
[20] S. Lee, J. Lee, S.H. Hwang, J. Yun, J. Jang, Enhanced Electroresponsive Performance of Double-Shell SiO_2/TiO_2 Hollow Nanoparticles, ACS Nano. 9 (2015) 4939–4949. doi:10.1021/nn5068495.
[21] H. Wang, L. Shi, T. Yan, J. Zhang, Q. Zhong, D. Zhang, Design of graphene-coated hollow mesoporous carbon spheres as high performance electrodes for capacitive deionization, J. Mater. Chem. A. 2 (2014) 4739. doi:10.1039/c3ta15152b.
[22] A. Cabot, A. Alivisatos, V. Puntes, L. Balcells, Ò. Iglesias, A. Labarta, Magnetic domains and surface effects in hollow maghemite nanoparticles, Phys. Rev. B. 79 (2009) 94419. doi:10.1103/PhysRevB.79.094419.
[23] G. Hassnain Jaffari, H.-Y. Lin, C. Ni, S. Ismat Shah, Physiochemical phase transformations in Co/CoO nanoparticles prepared by inert gas Condensation, Mater. Sci. Eng. B. 164 (2009) 23–29. doi:10.1016/j.mseb.2009.06.007.
[24] H.C.W. Skinner, R.W. Fitzpatrick, Biomineralization: processes of iron and manganese : modern and ancient environments, Catena Verlag, 1992. http://books.google.com/books/about/Biomineralization.html?id=-hsaAQAAIAAJ&pgis=1.
[25] W. Krauss, R. Birringer, Metastable phases synthesized by inert-gas condensation, Nanostructured Mater. 9 (1997) 109–112.
[26] E. Cockayne, I. Levin, H. Wu, A. Llobet, The magnetic structure of bixbyite a-Mn_2O_3: a combined density functional theory DFT+U and neutron diffraction study, (2012) 1–11. http://arxiv.org/abs/1211.6960v1.

[27] M. Oku, K. Hirokawa, S. Ikeda, X-ray photoelectron spectroscopy of manganese—oxygen systems, J. Electron Spectros. Relat. Phenomena. 7 (1975) 465–473. doi:10.1016/0368-2048(75)85010-9.
[28] H.W. Nesbitt, D. Banerjee, Interpretation of XPS Mn(2p) spectra of Mn oxyhydroxides and constraints on the mechanism of MnO_2 precipitation, Am. Mineral. 83 (1998) 305–315.
[29] Z.H. Wang, D.Y. Geng, Y.J. Zhang, Z.D. Zhang, Morphology, structure and magnetic properties of single-crystal Mn3O4 nanorods, J. Cryst. Growth. 310 (2008) 4148–4151. doi:10.1016/j.jcrysgro.2008.06.025.
[30] A.A. Audi, P.M. a. Sherwood, Valence-band x-ray photoelectron spectroscopic studies of manganese and its oxides interpreted by cluster and band structure calculations, Surf. Interface Anal. 33 (2002) 274–282. doi:10.1002/sia.1211.
[31] V. Di Castro, G. Polzonetti, XPS study of MnO oxidation, J. Electron Spectros. Relat. Phenomena. 48 (1989) 117–123. doi:10.1016/0368-2048(89)80009-X.
[32] X. Wang, Y. Li, Synthesis and formation mechanism of manganese dioxide nanowires/nanorods., Chemistry. 9 (2003) 300–6. doi:10.1002/chem.200390024.
[33] A. López-Ortega, D. Tobia, E. Winkler, I. V Golosovsky, G. Salazar-Alvarez, S. Estradé, M. Estrader, J. Sort, M. A. González, S. Suriñach, J. Arbiol, F. Peiró, R. Zysler, M. D. Baró, J. Nogués, Size-dependent passivation shell and magnetic properties in antiferromagnetic/ferrimagnetic core/shell MnO nanoparticles, J. Am. Chem. Soc. 132 (2010) 9398–407. doi:10.1021/ja1021798.
[34] T. Ahmad, K. V Ramanujachary, E. Lofland, A.K. Ganguli, Nanorods of manganese oxalate : a single source precursor to different manganese oxide nanoparticles (MnO , Mn_2O, (2004).
[35] M. Kim, X.M. Chen, X. Wang, C.S. Nelson, R. Budakian, P. Abbamonte, Pressure and field tuning the magnetostructural phases of Mn_3O_4: Raman scattering and x-ray diffraction studies, Phys. Rev. B. 84 (2011) 174424. doi:10.1103/PhysRevB.84.174424.
[36] W.S. Seo, H.H. Jo, K. Lee, B. Kim, S.J. Oh, J.T. Park, Size-dependent magnetic properties of colloidal Mn_3O_4 and MnO nanoparticles., Angew. Chem. Int. Ed. Engl. 43 (2004) 1115–7. doi:10.1002/anie.200352400.
[37] R.H. Kodama, A.E. Berkowitz, E.J. McNiff, Jr., S. Foner, Surface Spin Disorder in $NiFe_2O_4$ Nanoparticles, Phys. Rev. Lett. 77 (1996) 394–397. doi:10.1103/PhysRevLett.77.394.
[38] B. Martínez, X. Obradors, L. Balcells, A. Rouanet, C. Monty, Low Temperature Surface Spin-Glass Transition in γ- Fe_2O_3 Nanoparticles, Phys. Rev. Lett. 80 (1998) 181–184. doi:10.1103/PhysRevLett.80.181.
[39] X. Batlle, A. Labarta, Finite-size effects in fine particles: magnetic and transport properties, J. Phys. D. Appl. Phys. 35 (2002) R15–R42. doi:10.1088/0022-3727/35/6/201.
[40] A.H. Morrish, K. Haneda, P.J. Schurer, Surface magnetic strucutre of small γ-

Fe_2O_3 particles, Le J. Phys. Colloq. 37 (1976) C6-301-C6-305. doi:10.1051/jphyscol:1976663.
[41] T. Okada, H. Sekizawa, F. Ambe, S. Ambe, T. Yamadaya, Magnetic and Mossbauer studies of Co absorbed γ-Fe_2O_3, J. Magn. Magn. Mater. 31 (1983) 34–903.
[42] P. Z. Si, D. Li, J. W. Lee, C. J. Choi, Z.D. Zhang, D. Y. Geng, E. Brück, Unconventional exchange bias in oxide-coated manganese nanoparticles, Appl. Phys. Lett. 87 (2005) 133122. doi:10.1063/1.2072807.
[43] J. Du, Y. Gao, L. Chai, G. Zou, Y. Li, Y. Qian, Hausmannite Mn_3O_4 nanorods: synthesis, characterization and magnetic properties, Nanotechnology. 17 (2006) 4923–4928. doi:10.1088/0957-4484/17/19/024.
[44] P. Ayyub, M. Multani, M. Barma, Size-induced structural phase transitions and hyperfine properties of microcrystalline Fe_2O_3, J. Phys. C 21 (1988) 2229–2245. http://iopscience.iop.org/0022-3719/21/11/014 .

Chapter 6

POLYCRYSTALLINE HOLLOW CoO, Co_3O_4 and $CoFe_2O_4$ NANOPARTICLES: EFFECT of AFM PHASE IN ADDITION TO SURFACE EFFECT ON THE COECIVITY AND EXCHANGE BIAS

6.1 Abstract

We present magnetic response of polycrystalline hollow nanoparticles. Nanoparticles were composed of antiferromagnetic phase, which was mainly Co_3O_4 and ferromagnetic constituent phase, $CoFe_2O_4$. Initial Fe:Co ratio was varied to synthesize particles with different constituent phases in the nanocomposite upon post synthesis oxygen annealing. Increase in cobalt concentration resulted in relative increase of the AFM (Co_3O_4) phase compare to the FM ($CoFe_2O_4$) phase. Increase in AFM component led to lack of saturation as well as a large vertical and horizontal shift. Magnetic response is described in terms of FM crystal size, high field thermoremanent magnetization in AFM and increased average anisotropy due to AFM and surface spin glass phase. Even though FM crystallites were less than 7 nm in diameter, proximity of FM and AFM crystallites within nanoparticles led to strong coupling between the two phases.

6.2 Introduction

Exchange bias (EB) or exchange anisotropy was discovered six decades ago [1] and have been subject to intense research since then. It occurs in bilayers (or multilayers) composite of soft ferromagnetic (FM) films and hard antiferromagnetic (AFM) thin film, which causes a shift in the soft magnetization curve. Importantly, EB phenomenon has been successfully and practically utilized in magnetic recording [2–10]. In general, this phenomenon is complex and is affected by particle size [4,5,10–16], shell thickness [17–21], and the nature of interface coupling [12,22–27]. This phenomenon leads to an increase in coercivity (H_C) [9,22,28–30], training effect [31], asymmetry of the hysteresis loops [32]. The underlying mechanism of EB has been associated with the role of magnetic domains [24,33–38] to be aligned in field, uncompensated interfacial spins [9,12,15,39,40], pinned interfacial spins [41,42], domain size [43], and domain wall motion [24].

In addition to multilayers, EB has been commonly reported in core/shell [10,12,20,40,44–48], hollow [8,9,35,49] and solid [11,14,49–51] nanoparticles (NPs). Here, morphology of the particles brings in several complexities where the relative sizes of FM and AFM components, type of material (different phases) and inter/intra particle interactions affect magnetic properties [12,20,44,48,52,53]. Inverted core/shell (AFM/FM) NPs have revealed features such as extension of FiM order above the Currie temperature (T_C) of the shell, where the Néel temperature (T_N) is comparable with the bulk value [21,47,54], and nonmonotonic dependence on the core diameter of H_C and EB [12]. However, in the case of particles with solid and hollow morphologies that are crystalized in a single phase, surface spin glass (SG) transition is observed [5,8,55,56]. In case of hollow particles, additional contribution due to the surface SG phase arises attributed to the additional inner surface [8,35]. For example, in case of $NiFe_2O_4$ and γ-Fe_2O_3 hollow NPs, strikingly contrasting magnetic behavior compared to bulk and conventional solid particles have been reported [8,35]. In these cases, EB arises due to the coupling between surface SG phase with core FM phase.

Structurally, single phase hollow NPs exhibit polycrystallinity and are composed of the multiple crystallographic domains. Here, the polycrystallinity yields large interfacial area between randomly oriented crystallites. This random orientation leads to the random orientation of the local anisotropy axes. Hence, the overall effect of this morphology on the magnetic properties is manifested by the exhibition of high H_C, relatively high temperature magnetic irreversibility, lack of magnetic saturation, high blocking temperature (T_B) and EB, etc. [8,9,35,48]. So, EB arises in both cases where FM/AFM and FM/SG interface exist. However, the issue with all the reported systems i.e. $NiFe_2O_4$, γ-Fe_2O_3 and MnO/ γ-Mn_2O_3 hollow NPs is that post-synthesis annealing transforms magnetic phases or changes the morphology. γ-Fe_2O_3 transforms to α-Fe_2O_3 or Fe_3O_4 while in Mn oxide system, AFM MnO disappear on post annealing. In the case of $NiFe_2O_4$, post annealing leads to collapse of hollow morphology and hence a significant decrease in SG contribution [8]. Hence, in all the reported systems there is a limitation to play with either SG or AFM content. Therefore, our goal is to synthesize particles where both effects can be measured and compared. Hence, polycrystalline hollow nanoparticles have been prepared and investigated where crystallites of $CoFe_2O_4$ (FiM) and CoO/Co_3O_4 (AFM) phases with different weight ratio, depending upon initial Co:Fe ratio, exists and are randomly oriented. Furthermore, we looked at three effects, namely surface effects (surface SG phase), effect of AFM phase on FiM, and finite size effect where crystallites size are different for different initial compositions.

6.3 Experimental Section

Mixtures of different initial Co:Fe wires (50:50, 60:40, and 70:30) ratios were thermally evaporated in an inert gas condensation system (IGC) to obtained metallic NPs. Evaporation yielded FeCo NPs with different Fe:Co ratios. The resulting NPs were oxygen passivated by controllably bringing the chamber to atmospheric condition. The growth technique has been extensively discussed in chapter 2. Three samples with Co:Fe ratios of 50:50, 60:40, and 70:30, S0.5, S0.6, and S0.7, respectively, were evaporated. The resulting Core/shell NPs were then oxygen passivated at 400oC for an hour in an oxygen rich environment to obtained both desired compositions and morphology (e.g. hollow morphology) [49,57,58]. By intentionally varying the cobalt concentration, extra cobalt oxide phases are introduced into the NPs, yielding multiphase NPs. Cobalt has two oxide phases that are well known to be antiferromagnetic material (Co_3O_4 and CoO). The morphology of the resulting NPs was investigated with a Talos F200C transmission electron microscope (TEM), while the crystal structure was analyzed by the high resolution Bruker D8 x-ray powder diffractometer (XRD) that has a monochromatic Cu Kα1 source. The magnetic properties of the NPs were obtained by a physical properties measurement system from Quantum Design.

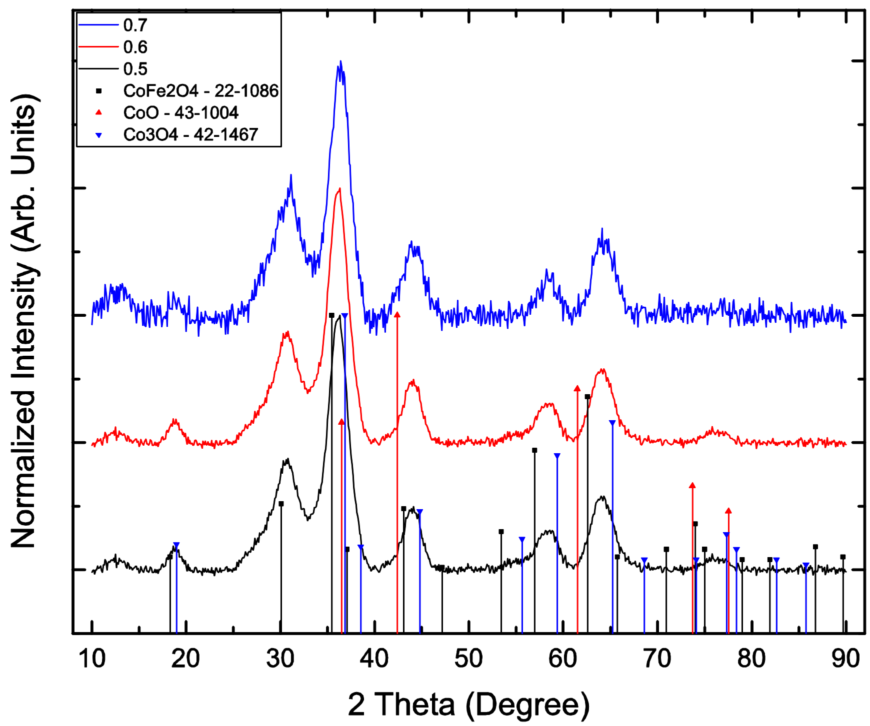

Figure 6-1: X-ray diffraction patterns of post-synthesis annealed NPs with different initial cobalt concentrations.

6.4 Structural and Morphological Studies

The resulting XRD patterns of the three samples S0.5, S0.6, and S0.7 are shown in figure 6-1. From figure 6-1, the patterns are seen to have very broad peaks, which is indicate that particles are composed of small crystal size. The breadth of the peaks of sample S0.7 are seen to be reduced compared to sample S0.5 and S0.6, which means that the crystallites are bigger for this sample. The peaks of sample S0.7 are also shifted to higher angles. To identify the phases present in the NPs particles, the patterns were matched to three possible standards, namely $CoFe_2O_4$ (JCPDS file no. 22-1086), CoO (JCPDS file no. 22-1004), and Co_3O_4 (JCPDS file no. 42-1467). Since both $CoFe_2O_4$ and Co_3O_4 are spinel structures, their peaks are very close to each other, with Co_3O_4 peaks having higher 2θ values. The broad nature of the peaks makes it very difficult to distinguished between these two phases. The most intense reflection of CoO occurs around 42.36^o and a weak corresponding peak is present in the pattern, as shown in figure 6-1. Even though as Co percentage increases, as we move from sample S0.5 to S0.6 to S0.7, this broad peal remains the same on relative intensity scale. Hence this shows that XRD patterns mainly correspond to spinel structure and majority of the constituent phases are $CoFe_2O_4$ and Co_3O_4. In addition to that, it is also intuitively clear that Co_3O_4 phase progressively increases for sample S0.5, S0.6 and S0.7. More direct evidence of presence of FM $CoFe_2O_4$, will be presented in the magnetic section.

The morphology of the NPs is presented in figure 6-2. HRTEM images for all the samples S0.5, S0.6 and S0.7, revealed that NPs are hollow and composed of multiple crystallites. In correlation with XRD, polycrystallinity within single particle is associated with the $CoFe_2O_4$, Co_3O_4 and CoO phases. Out of which the first two phases are dominant. Two different magnifications are shown for each of the samples, where the lower magnification shows that all the samples are agglomerated and have varying particle size as well as varying void of the NPs. The higher magnification revealed the nature of the crystallites and the voids of the NPs.

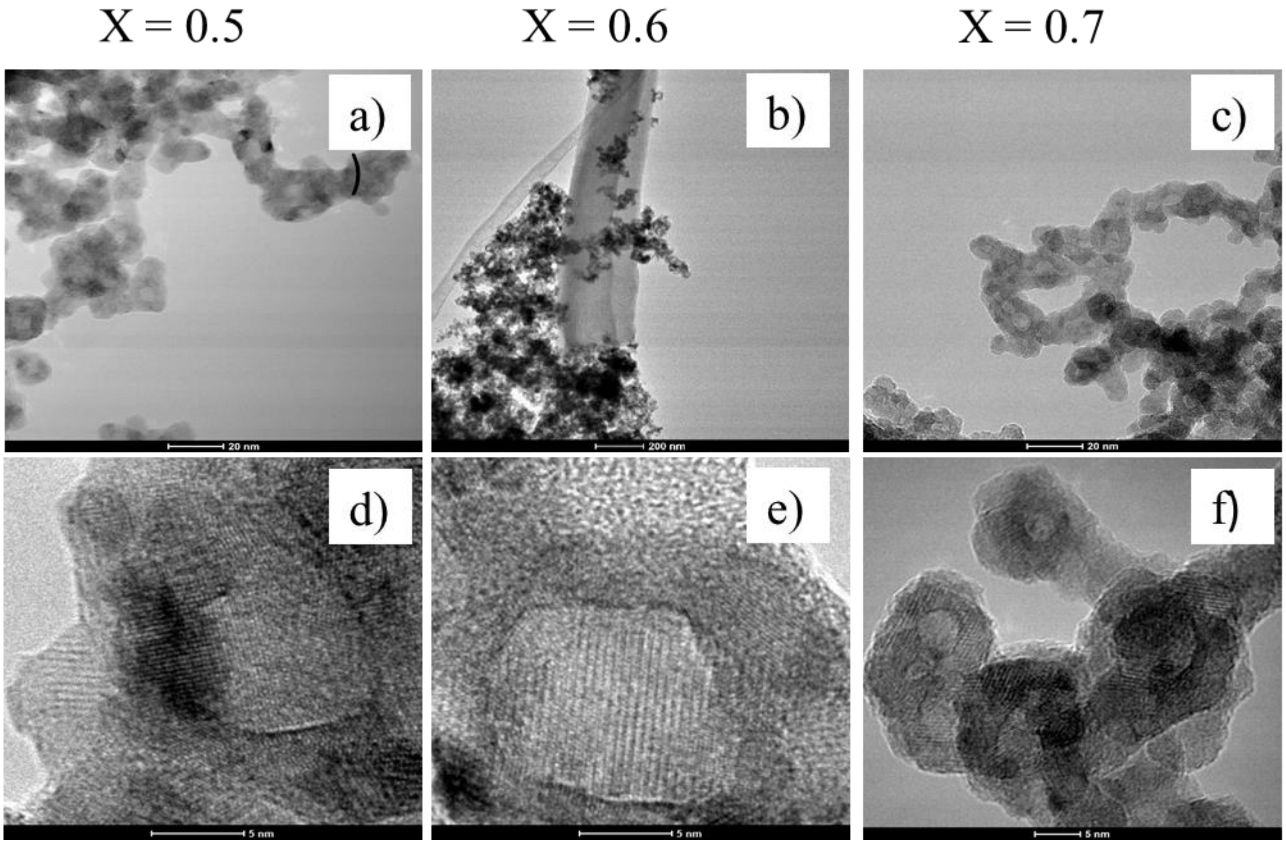

Figure 6-2: Bright-field TEM micrographs of post annealed samples of cobalt oxide and $CoFe_2O_4$ for different starting concentration of Co during growth, a – c) showing lower magnification and d-f) showing higher magnification.

Looking more closely on the higher magnification micrographs, the lattice spacing of the NPs was identified and measured, figure 6-3. In figure 6-3 a), three distinct lattice spacing (d_spacing) are identified, 0.47 nm, 0.3 nm and 0.27 nm. These values correspond to [111] spinel structure, [220] spinel structure, and [111] cubic, respectively [23,26,59–61]. Therefore, this confirms that sample S0.5 has CoO, as well as the $CoFe_2O_4$ spinel structure. Both phases are seen to lie next to each other.

In figure 6-3 b), similar thing is observed. However, the spinel structure (0.45 nm) crystallites are observed to have grown significantly. In figure 6-3 c), all the identified lattice spacings are around 0.45 nm, which as mentioned belong to the spinel structure. This support the claim that the higher 2θ shift of the patterns for the 0.7 samples means that more Co_3O_4 phase is present. It is known that lattice spacing of spinal structures are bigger than cubic structures [60]. Therefore, the observe lattice spacing of 0.45 nm for the S0.7 sample indicate that the CoO phase transformed to Co_3O_4 as the cobalt concentration was increased [23,59,60]. CoO phase could still be present in this sample, the ratio of the two peaks mention in the XRD section suggest this. In fact, Nam et al. showed using Mössbauer measurement that CoO is present in samples with higher cobalt concentration [59].

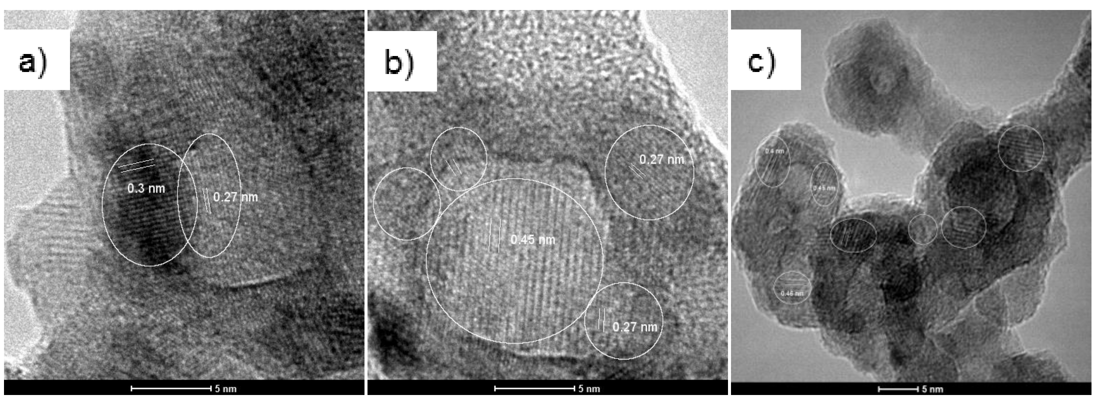

Figure 6-3: HRTEM micrographs of S0.5, S0.6, and S0.7 samples with lattice spacing markings.

From both XRD and HRTEM analysis, three oxides have been identified to be present in the samples, with sample S0.5 and S0.6 considered having CoO and $CoFe_2O_4$, while sample S0.7 having significantly higher Co_3O_4 concentration. Both

CoO and Co_3O_4 are AFM with Néel temperatures (T_N) at 290 - 298 K and 40 K, respectively [26,62,63]. $CoFe_2O_4$ on the other hand is hard FM material with a bulk saturation magnetization around 80 emu/g [64]. It has a very large coercivity and a square hysteresis loop, where both decrease with the size of the NPs [26]. However, it has been well established that magnetic properties of NPs can be enhanced by coupling two different magnetic materials, which results in a shift of the hysteresis loop. Therefore, the coupling of the AFM phases to the FM should lead to enhanced properties.

6.5 Magnetic Properties

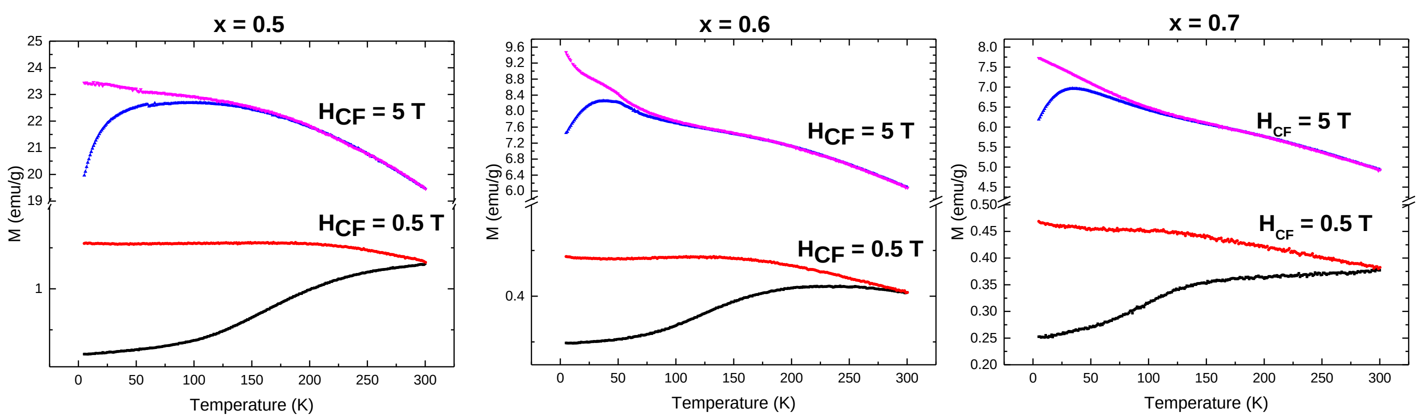

Figure 6-4: Zero Field Cooled and Field Cooled magnetization versus temperature curves at different cobalt concentration at 0.5 T and 5 T.

Figure 6-4 shows ZFC and FC curves for the magnetization as a function of temperature for sample S0.5, S0.6 and S0.7. FC curves were recorded in low (0.5 T) and high (5 T) cooling fields. For the low field case, magnetic reversibility for all the samples remains intact from 5 K to 300 K and is independent of the amount of the

AFM content i.e. Co_3O_4 and CoO phases. This is indicative of high magnetic anisotropy barrier due to the presence of AFM phases coupled to the FM $CoFe_2O_4$ crystallites whose mechanism is explainable in terms of EB [9,23,30,65]. In addition to that, even in pure single phase hollow nanoparticle systems, namely γ-Fe_2O_3 [66] and $CoFe_2O_4$ [49] low and high field magnetic irreversibility has been reported. In those case, AFM phase was absent to increase the anisotropy barrier. The anisotropy barrier increase was explained to be associated with the randomly oriented multiple crystallographic domains generating differentiated local anisotropy axes and high surface area. As it is known for the case of magnetic nanoparticles that surface anisotropy contributes to the overall effect anisotropy constant which results in magnetic irreversibility and loop shifts at low temperatures. In the present case, we have both these feature that presence of antiferromagnetic crystallites and hollow geometry. For both high and low field magnetization curves for all sample as shown in figure 6-4, a decrease in magnetization as cobalt content increases is revealed. Decrease in magnetization indicates a systematic decrease in the concentration of the FM component as the concentration of $CoFe_2O_4$ decreases while the AFM component increases.

Figure 6-4 shows FC and ZFC magnetization branches recorded for sample S0.5, S0.6 and S0.7. ZFC branch is broad for sample S0.5 while for the sample S0.6 and S0.7, its narrower and pushed to the lower temperatures. This indicates that for sample S0.6 and S0.7, crystal size of the $CoFe_2O_4$ decreases and pushes blocking peak towards lower temperatures as is typical case for magnetic nanoparticles [14,56,67]. As it was explained in XRD section, $CoFe_2O_4$ phase was highest in sample S0.5 compared to sample S0.6 and S0.7. it was also shown that relative concentration of

CoO phase highest for sample S0.5. Temperature dependent behavior of the magnetization also confirm both these structural findings. T_N of CoO (290 – 298 K) is significantly higher than the T_N (~40 K) of Co_3O_4. Hence, increase in Co_3O_4 concentration as we move from S0.5 to S0.6, irreversibility point has also been observed to decrease. Blocking temperature for S0.5, S0.6 and S0.7 is around 100 K, 40 and 40K, respectively. There is no drastic change in the temperature dependent shift for sample S0.7 in comparison with S0.6. However, as cobalt concentration increases, $CoFe_2O_4$ crystal size decreases and progressive decrease in the blocking temperature is expected which is in contradiction with the variation of blocking temperature. Hence, we can conclude that coupling between FM/AFM phase has been improved with cobalt concentration and overcome superparamagnetic fluctuation for S0.7.

Another noticeable aspect in the figure 6-4 is the low temperature rise in the FC curve. In general, one of the reasons to observe this rise is the presence of surface spin glass phase [26,55,56,68]. At low temperatures, when lesser thermal energy is available, spins lying on the surface undergoes SG phase transition [55,68]. This phenomena has been shown to be more pronounced in case of hollow particles [49,66]. In addition to SG like phase, up turn may occur due to defects in AFM [39,63,69,70]. On FC, in AFM, a domain state develops which yields an irreversible surplus thermoremanent magnetization and play a critical role to in observation of EB [34,71–73] . In a typical AFM, defects at the surface and in the bulk give rise to domain wall pinning yielding a metastable domain structure [70]. These defects can be structural or substitutional and reflect their presence in the high field FC magnetization behavior as rise in the low temperature regime [69]. In the present study, particles have larger surface area therefore presence of surface defects such as oxygen vacancies and structural strain due to lower coordination number, are expected to affect AFM crystallites. Hence, in the high field regime thermoremanent magnetization may contribute to the FC M(T) branch. In the present case, there is small rise in the FM magnetization curve for lowest cobalt concentration sample S0.5, as shown in figure 6-4. In this case, FM $CoFe_2O_4$ phase is highest in concentration and least AFM component. As the AFM component increase (for sample S0.6), the rise in the FM curve is more pronounced. While the rise is lower in magnitude for higher cobalt concentration sample i.e. S0.7. Hence, our results show that AFM phase (Co_3O_4) phase exhibited high thermoremanent magnetization for sample S0.6. As for sample S0.7, where Co_3O_4 phase increases further and crystallites are expected to grow in size and hence defect concentration reduces and rise in FC branch is suppressed in comparison with the sample S0.6.

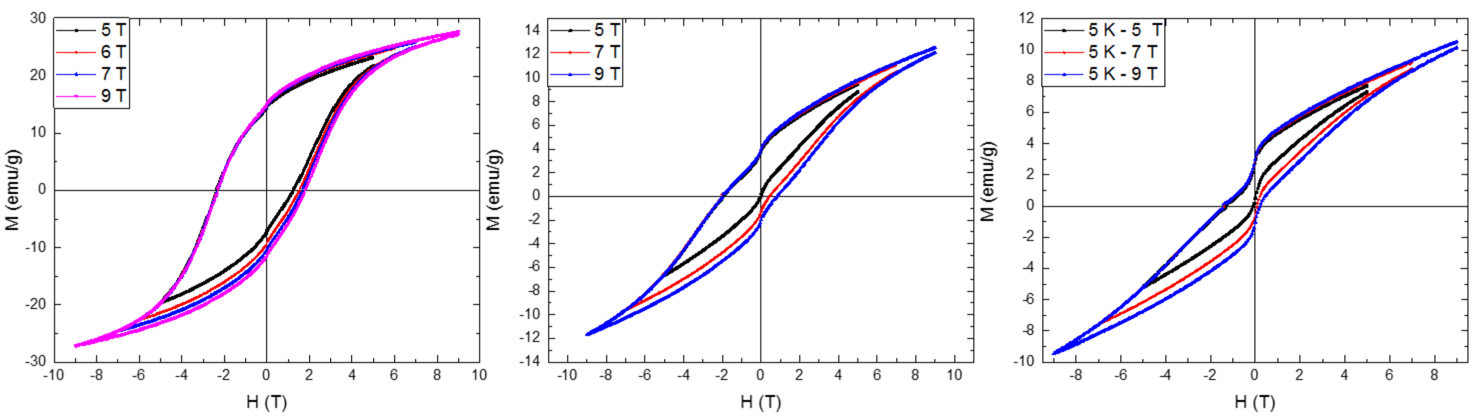

Figure 6-5: Magnetization versus field measurements as a function of H_{CF} at different cobalt concentration at 5 K.

Figure 6-5, shows magnetization versus field response for all the samples measured at 5 K under FC condition. Cooling fields were 5, 7 and 9 T. As the cobalt concentration increases, maximum value of the magnetization decreases, 27.8, 12.6, and 10.5 emu/g for sample S0.5, S0.6, and S0.7, respectively, at 9 T. It has been discussed above that with cobalt concentration increasing, the amount of Co_3O_4 increases while CoO concentration remains the same. Hence, decrease in maximum magnetization again reinforces the fact that with increasing cobalt concentration, AFM contribution from Co_3O_4 increases and FM contribution from $CoFe_2O_4$ decreases. Also with increase in Co_3O_4 concentration, the degree of saturation also becomes poor (see figure 6-5). The decrease in the degree of saturation is indicative of the enhancement of coupling between the FM and AFM components in the particles. Positive high field magnetization curves coincide well for sample S0.5, S0.6 and S0.7. This also confirms that loops are not minor. While on field reversal from negative high field overlapping of the magnetization curves becomes poor as we move from lowest concentration of cobalt (sample S0.5) to highest concentration of cobalt (sample S0.7). This is again manifestation of strong coupling of the FM spins lying proximity of AFM and FM spin pinning improves with increase of Co_3O_4 phase.

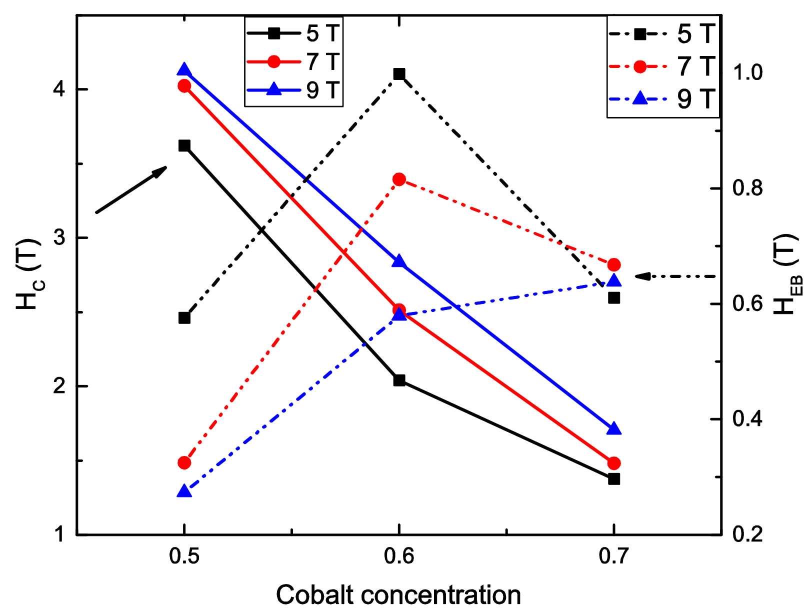

Figure 6-6: Magnetization versus field measurements as a function of HCF at different cobalt concentration at 5 K.

To further understand magnetic response of the system as a function of cobalt concentration (or Co_3O_4 concentration), coercive field and exchange bias has been plotted in figure 6-6. For all the cooling fields, H_C decreases with cobalt concentration. For example, the H_C values at 9 T were 4.13, 2.84, and 1.71 T, for sample S0.5, S0.6, and S0.7, respectively. As it was discussed in the structural section that CoO phase remained same while Co_3O_4 increased with cobalt concentration. Since H_C is proportional to anisotropy constant [16,49] whose value for Co_3O_4 is significantly lower in magnitude in comparison with CoO, hence with the relative increase in the

Co_3O_4, H_C decreases. In addition to this average, crystal size also effects H_C [11,15,50,74,75]. As cobalt concentration increases, $CoFe_2O_4$ concentration decreases with a corresponding decrease in the crystal size which also contributed to the decreasing trend of H_C.

Unlike coercivity, exchange bias variation is nonmonotonic as a function of cobalt concentration. Large values of vertical and horizontal shift for all the samples shows that system exhibit strong FM/AFM coupling. In cooling field of 7 T, EB is 0.33 T for sample S0.5 which increases to 0.82 T for sample S0.6 and then decrease to 0.67 for sample S0.7. As presented above relative CoO (Co_3O_4) decreases (increases) with cobalt concertation. Hence even though overall AFM component increases with Co concentration, hence it is expected that EB should increase. However due to lower anisotropy constant of Co_3O_4 phase in comparison with CoO phase, EB decreases for sample with highest Co_3O_4 concentration i.e. sample S0.7.

Pure $CoFe_2O_4$ hollow NPs prepared with same technique, exhibited EB of 0.73 T. In comparison with the pure $CoFe_2O_4$ hollow NPs, in the present study we have additional AFM component. Sample S0.5 and S0.7 exhibit lower value of the exchange bias in comparison with the single phase $CoFe_2O_4$ hollow nanoparticle system. While S0.6 exhibited EB, which is higher than the pure $CoFe_2O_4$ hollow NPs. In the present study, even though an extra source of anisotropy has been added which is the AFM phase, however EB has been at most comparable with the system where AFM phase is not present. In case of pure $CoFe_2O_4$ hollow NPs, extra contribution comes from the surface anisotropy. Hence, it shows that surface spin glass is more robust. This can be understood in terms of the size reduction of the $CoFe_2O_4$ constituent crystallites in the nanocomposite hollow nanoparticle presented in the present study. The size reduction of the FM $CoFe_2O_4$ lead to destabilization of the magnetic order and can be understood in the context of superparamagnetism. However, in the present study even though $CoFe_2O_4$ size has been reduced still high value of EB bias has been achieved which is due to improved effect FM/AFM coupling.

6.6 Conclusion

Synthesis of hollow polycrystalline particles composed of FM and AFM crystallites are presented. Major AFM phase identified to be Co_3O_4. Small contribution of CoO phase was observed, whose relative concentration was found to decrease with cobalt concentration. HRTEM studies revealed that crystallites where less 7 nm in size. For the low field case, magnetic reversibility for all the samples remains intact from 5 K to 300 K and is independent of the amount of the AFM content i.e. Co_3O_4 and CoO phases. This is indicative of high magnetic anisotropy barrier due to the presence of AFM phases coupled to the FM $CoFe_2O_4$ crystallites whose mechanism is explainable in terms of EB. As it is known for the case of magnetic NPs, surface anisotropy contributes to the overall effect anisotropy constant, which results in magnetic irreversibility and loop shifts to low temperatures. In the present case, we have both presence of antiferromagnetic crystallites and hollow geometry. Decrease in magnetization with cobalt concentration indicated a systematic decrease in the concentration of the FM component as the concentration of $CoFe_2O_4$ decreases while the AFM component (Co_3O_4) increases. As cobalt concentration increases, $CoFe_2O_4$ crystal size decreases and progressive decrease in the blocking temperature is expected which is in contradiction with the variation of blocking temperature. Hence, we can conclude that coupling between FM/AFM phase has been improved with cobalt concentration and overcome superparamagnetic fluctuation for high cobalt concentration sample for which FM $CoFe_2O_4$ phase is smallest in size.

Low temperature high field rise in FC magnetization curve have been discussed in terms of SG phase and irreversible surplus thermoremanent magnetization of AFM component. In a typical AFM, defects at the surface and in the bulk give rise to domain wall pinning yielding a metastable domain structure. For all the cooling fields, H_C decreases with cobalt concentration, which is consistent with the increase in the lower anisotropy constant AFM Co_3O_4 phase and decrease in the average size of the FM $CoFe_2O_4$ phase. Unlike coercivity, exchange bias variation is nonmonotonic as a function of cobalt concentration at a 7 T cooling field. Large values of vertical and horizontal shift for all the samples showed that system exhibit strong FM/AFM coupling. Hence, even though overall AFM component increases with cobalt concentration, it is expected that EB should increase. However due to lower anisotropy constant of Co_3O_4 phase in comparison with CoO phase, EB decreases for sample with highest Co_3O_4 concentration.

REFERENCES

[1] W.H. Meiklejohn, C.P. Bean, New magnetic anisotropy, Phys. Rev. 105 (1957) 904–913. doi:10.1103/PhysRev.105.904.

[2] S. Sun, C.B. Murray, D. Weller, L. Folks, A. Moser, Monodisperse FePt nanoparticles and ferromagnetic FePt nanocrystal superlattices, Science (80-.). 287 (2000) 1989–92. doi:10.1126/science.287.5460.1989.

[3] V. Skumryev, S. Stoyanov, Y. Zhang, Beating the superparamagnetic limit with exchange bias, Nature. 423 (2003) 19–22. doi:10.1038/nature01750.1.

[4] R.. Kodama, Magnetic nanoparticles, J. Magn. Magn. Mater. 200 (1999) 359–372. doi:10.1016/S0304-8853(99)00347-9.

[5] R.H. Kodama, A.E. Berkowitz, E.J. McNiff, Jr., S. Foner, Surface Spin Disorder in $NiFe_2O_4$ Nanoparticles, Phys. Rev. Lett. 77 (1996) 394–397. doi:10.1103/PhysRevLett.77.394.

[6] M.E. Mchenry, Nano-scale materials development for future, 48 (2000).

[7] S. Wei, Q. Wang, J. Zhu, L. Sun, H. Lin, Z. Guo, Multifunctional composite core-shell nanoparticles., Nanoscale. 3 (2011) 4474–502. doi:10.1039/c1nr11000d.

[8] G.H. Jaffari, A. Ceylan, C. Ni, S.I. Shah, Enhancement of surface spin disorder in hollow $NiFe_2O_4$ nanoparticles, J. Appl. Phys. 107 (2010) 13910. doi:10.1063/1.3277041.

[9] M.A. Bah, G.H. Jaffari, F.A. Khan, S.I. Shah, Surfaces and their effect on the magnetic properties of polycrystalline hollow γ-Mn_2O_3 and MnO nanoparticles, Appl. Surf. Sci. 375 (2016) 136–143. doi:10.1016/j.apsusc.2016.02.145.

[10] A. Ceylan, C.C. Baker, S.K. Hasanain, S. Ismat Shah, Effect of particle size on the magnetic properties of core-shell structured nanoparticles, J. Appl. Phys. 100 (2006) 34301. doi:10.1063/1.2219691.

[11] E.F. Kneller, F.E. Luborsky, Particle size dependence of coercivity and remanence of single-domain particles, J. Appl. Phys. 34 (1963) 656–658. doi:10.1063/1.1729324.

[12] G. Salazar-Alvarez, J. Sort, S. Suriñach, M.D. Baró, J. Nogués, Synthesis and size-dependent exchange bias in inverted core-shell MnO|Mn_3O_4 nanoparticles., J. Am. Chem. Soc. 129 (2007) 9102–8. doi:10.1021/ja0714282.

[13] G. Hassnain Jaffari, T. Ekiert, K.M. Unruh, S. Ismat Shah, Effect of particle size distribution on the magnetic properties γ-Fe_2O_3 nanoparticles, Mater. Sci. Eng. B. 177 (2012) 935–941. doi:10.1016/j.mseb.2012.04.016.

[14] P. Vavassori, E. Angeli, D. Bisero, F. Spizzo, F. Ronconi, Particle Size Distribution and Temperature Dependence of Coercivity and Remanence in Sputtered Co/Cu Granular Films, Phys. Status Solidi. 189 (2002) 423–427. doi:10.1002/1521-396X(200202)189:2<423::AID-PSSA423>3.0.CO;2-W.

[15] M.S. Seehra, A. Punnoose, Particle size dependence of exchange-bias and coercivity in CuO nanoparticles, Solid State Commun. 128 (2003) 299–302. doi:10.1016/j.ssc.2003.08.029.

[16] X. Batlle, A. Labarta, Finite-size effects in fine particles: magnetic and transport properties, J. Phys. D. Appl. Phys. 35 (2002) R15–R42. doi:10.1088/0022-3727/35/6/201.
[17] J.M. Soares, V.B. Galdino, O.L.A. Conceição, M.A. Morales, J.H. de Araújo, F.L.A. Machado, Critical dimension for magnetic exchange-spring coupled core/shell $CoFe_2O_4/CoFe_2$ nanoparticles, J. Magn. Magn. Mater. 326 (2013) 81–84. doi:10.1016/j.jmmm.2012.08.040.
[18] M. Coşkun, M. Korkmaz, T. Fırat, G.H. Jaffari, S.I. Shah, Synthesis of SiO_2 coated $NiFe_2O_4$ nanoparticles and the effect of SiO_2 shell thickness on the magnetic properties, J. Appl. Phys. 107 (2010) 09B523. doi:10.1063/1.3359426.
[19] G.C. Lavorato, D. Peddis, E. Lima, H.E. Troiani, E. Agostinelli, D. Fiorani, et al., Magnetic Interactions and Energy Barrier Enhancement in Core/Shell Bimagnetic Nanoparticles, J. Phys. Chem. C. 119 (2015) 15755–15762. doi:10.1021/acs.jpcc.5b04448.
[20] A. López-Ortega, D. Tobia, E. Winkler, I. V Golosovsky, G. Salazar-Alvarez, S. Estradé, M. Estrader, J. Sort, M. A. González, S. Suriñach, J. Arbiol, F. Peiró, R. Zysler, M. D. Baró, J. Nogués, Size-dependent passivation shell and magnetic properties in antiferromagnetic/ferrimagnetic core/shell MnO nanoparticles, J. Am. Chem. Soc. 132 (2010) 9398–407. doi:10.1021/ja1021798.
[21] I. Golosovsky, G. Salazar-Alvarez, A. López-Ortega, M. González, J. Sort, M. Estrader, S. Suriñach, M. Baró, J. Nogués, Magnetic Proximity Effect Features in Antiferromagnetic/Ferrimagnetic Core-Shell Nanoparticles, Phys. Rev. Lett. 102 (2009) 247201. doi:10.1103/PhysRevLett.102.247201.
[22] G. Vallejo-Fernandez, L. Fernandez-Outon, K. O'Grady, Interface Role in CoFe/IrMn Exchange Biased Systems, in: INTERMAG 2006 - IEEE Int. Magn. Conf., IEEE, 2006: pp. 952–952. doi:10.1109/INTMAG.2006.374983.
[23] G.C. Lavorato, E. Lima, H.E. Troiani, R.D. Zysler, E.L. Winkler, Exchange-coupling in thermal annealed bimagnetic core/shell nanoparticles, J. Alloys Compd. 633 (2015) 333–337. doi:10.1016/j.jallcom.2015.02.050.
[24] A. Benassi, M. a Marioni, D. Passerone, H.J. Hug, Role of interface coupling inhomogeneity in domain evolution in exchange bias., Sci. Rep. 4 (2014) 4508. doi:10.1038/srep04508.
[25] Y. Zhang, Z. Yang, B. Zhu, S. Chen, X. Yang, R. Xiong, et al., Exchange-spring effect in $CoFe_2O_4/CoFe_2$ composite nano-particles, J. Alloys Compd. 567 (2013) 73–76. doi:10.1016/j.jallcom.2013.03.078.
[26] E.L. Jr, E.L. Winkler, D. Tobia, H.E. Troiani, R.D. Zysler, E. Agostinelli, et al., Bimagnetic CoO Core/$CoFe_2O_4$ Shell Nanoparticles: Synthesis and Magnetic Properties, Chem. Mater. 24 (2012) 512−516. doi:10.1021/cm2028959.
[27] J. Xiang, X. Zhang, J. Li, Y. Chu, X. Shen, Fabrication, characterization, exchange coupling and magnetic behavior of $CoFe_2O_4/CoFe_2$ nanocomposite nanofibers, Chem. Phys. Lett. 576 (2013) 39–43.

doi:10.1016/j.cplett.2013.05.020.
[28] J.T. Elizalde Galindo, A.W. Bhuiya, F. Rivera Gómez, M. Aquino, C.E. Botez, Temperature dependence of magnetic properties and magnetic interactions in YCo_5/Y_2Co_{17} nanocomposite powders, J. Phys. D Appl. Phys. J. Phys. D Appl. Phys. 41 (2008) 95008–5. doi:10.1088/0022-3727/41/9/095008.
[29] N. Sharma, G.H. Jaffari, S.I. Shah, D.J. Pochan, Orientation-dependent magnetic behavior in aligned nanoparticle arrays constructed by coaxial electrospinning., Nanotechnology. 21 (2010) 85707. doi:10.1088/0957-4484/21/8/085707.
[30] G.C.P. Leite, E.F. Chagas, R. Pereira, R.J. Prado, A.J. Terezo, M. Alzamora, et al., Exchange coupling behavior in bimagnetic $CoFe_2O_4/CoFe_2$ nanocomposite, J. Magn. Magn. Mater. 324 (2012) 2711–2716. doi:10.1016/j.jmmm.2012.03.034.
[31] B. Martínez, X. Obradors, L. Balcells, A. Rouanet, C. Monty, Low Temperature Surface Spin-Glass Transition in γ-Fe_2O_3 Nanoparticles, 80 (1998).
[32] G.H. Jaffari, A.K. Rumaiz, J.C. Woicik, S.I. Shah, Influence of oxygen vacancies on the electronic structure and magnetic properties of $NiFe_2O_4$ thin films, J. Appl. Phys. 111 (2012) 93906. doi:10.1063/1.4704690.
[33] M. Kiwi, J. Mejia-Lopez, R.D. Portugal, R. Ramirez, Exchange bias theory: The role of interface structure and of domains in the ferromagnet, in: J.L. MoranLopez (Ed.), Phys. LOW Dimens. Syst., 2001: pp. 295–300. doi:0-306-46566-3.
[34] J. Keller, P. Miltényi, B. Beschoten, G. Güntherodt, U. Nowak, K. Usadel, Domain state model for exchange bias. II. Experiments, Phys. Rev. B. 66 (2002) 14431. doi:10.1103/PhysRevB.66.014431.
[35] A. Cabot, A. Alivisatos, V. Puntes, L. Balcells, Ò. Iglesias, A. Labarta, Magnetic domains and surface effects in hollow maghemite nanoparticles, Phys. Rev. B. 79 (2009) 94419. doi:10.1103/PhysRevB.79.094419.
[36] C. Kittel, Theory of the Structure of Ferromagnetic Domains in Films and Small Particles, Phys. Rev. 70 (1946) 965–971. doi:10.1103/PhysRev.70.965.
[37] U. Nowak, K. Usadel, J. Keller, P. Miltényi, B. Beschoten, G. Güntherodt, Domain state model for exchange bias. I. Theory, Phys. Rev. B. 66 (2002) 14430. doi:10.1103/PhysRevB.66.014430.
[38] J J. Nogués, J. Sort, V. Langlais, V. Skumryev, S. Suriñach, J.S. Muñoz, M. D. Baró, Exchange bias in nanostructures, Phys. Rep. 422 (2005) 65–117. doi:10.1016/j.physrep.2005.08.004.
[39] J. Geshev, T. Dias, S. Nicolodi, R. Cichelero, A. Harres, J.J.S. Acuña, Role of the uncompensated interface spins in polycrystalline exchange-biased systems, J. Phys. D. Appl. Phys. 44 (2011) 95002. doi:10.1088/0022-3727/44/9/095002.
[40] C. Liu, J. Cui, X. He, H. Shi, Large exchange bias with remarkable thermostability in an inverted quasi core/shell CoO/γ-Fe_2O_3 granular system, J. Nanoparticle Res. 16 (2014) 2320. doi:10.1007/s11051-014-2320-7.
[41] M.Y. Khan, C.-B. Wu, W. Kuch, Pinned magnetic moments in exchange bias:

Role of the antiferromagnetic bulk spin structure, Phys. Rev. B. 89 (2014) 94427. doi:10.1103/PhysRevB.89.094427.

[42] H. Ohldag, A. Scholl, F. Nolting, E. Arenholz, S. Maat, A. T. Young, Correlation between exchange bias and pinned interfacial spins., Phys. Rev. Lett. 91 (2003) 17203. doi:10.1103/PhysRevLett.91.017203.

[43] A. Scholl, F. Nolting, J.W. Seo, H. Ohldag, J. Stöhr, S. Raoux, et al., Domain-size-dependent exchange bias in Co/$LaFeO_3$, Appl. Phys. Lett. 85 (2004) 4085–4087. doi:10.1063/1.1813633.

[44] H. Zeng, J. Li, Z.L. Wang, J.P. Liu, S. Sun, Bimagnetic Core / Shell FePt / Fe_3O_4 Nanoparticles, (2004) 3–6.

[45] J.M. Soares, O.L.A. Conceição, F.L.A. Machado, A. Prakash, S. Radha, A.K. Nigam, Magnetic couplings in $CoFe_2O_4$/FeCo–FeO core–shell nanoparticles, J. Magn. Magn. Mater. 374 (2015) 192–196. doi:10.1016/j.jmmm.2014.08.015.

[46] P. Z. Si, D. Li, J. W. Lee, C. J. Choi, Z.D. Zhang, D. Y. Geng, E. Brück, Unconventional exchange bias in oxide-coated manganese nanoparticles, Appl. Phys. Lett. 87 (2005) 133122. doi:10.1063/1.2072807.

[47] A. Berkowitz, G. Rodriguez, J. Hong, K. An, T. Hyeon, N. Agarwal, D. Smith, E. Fullerton, Antiferromagnetic MnO nanoparticles with ferrimagnetic Mn_3O_4 shells: Doubly inverted core-shell system, Phys. Rev. B. 77 (2008) 24403. doi:10.1103/PhysRevB.77.024403.

[48] G. Hassnain Jaffari, S. Rizwan Ali, S. K. Hasanain, G. Güntherodt, S. Ismat Shah, Stabilization of surface spin glass behavior in core-shell $Fe_{67}Co_{33}$–$CoFe_2O_4$ nanoparticles, J. Appl. Phys. 108 (2010) 63921. doi:10.1063/1.3478738.

[49] G.H. Jaffari, a Ceylan, H.P. Bui, T.P. Beebe, S. Ozcan, S.I. Shah, Non-equilibrium cation distribution and enhanced spin disorder in hollow $CoFe_2O_4$ nanoparticles., J. Phys. Condens. Matter. 24 (2012) 336004. doi:10.1088/0953-8984/24/33/336004.

[50] A.J. Newell, R.T. Merrill, Single-domain critical sizes for coercivity and remanence, J. Geophys. Res. 104 (1999) 617. doi:10.1029/1998JB900039.

[51] L. Zhao, H. Zhang, Y. Xing, S. Song, S. Yu, W. Shi, et al., Studies on the magnetism of cobalt ferrite nanocrystals synthesized by hydrothermal method, J. Solid State Chem. 181 (2008) 245–252. doi:10.1016/j.jssc.2007.10.034.

[52] B. Lu, H. Huang, X.L. Dong, X.F. Zhang, J.P. Lei, J.P. Sun, et al., Influence of alloy components on electromagnetic characteristics of core/shell-type Fe–Ni nanoparticles, J. Appl. Phys. 104 (2008) 114313. doi:10.1063/1.3040006.

[53] A. H. Habib, C.L. Ondeck, P. Chaudhary, M.R. Bockstaller, M.E. McHenry, Evaluation of iron-cobalt/ferrite core-shell nanoparticles for cancer thermotherapy, J. Appl. Phys. 103 (2008) 07A307. doi:10.1063/1.2830975.

[54] A. E. Berkowitz, G. F. Rodriguez, J. I. Hong, K. An, T. Hyeon, N. Agarwal, D. Smith, E. Fullerton, Monodispersed MnO nanoparticles with epitaxial Mn_3O_4 shells, J. Phys. D. Appl. Phys. 41 (2008) 134007. doi:10.1088/0022-3727/41/13/134007.

[55] R.J. Tackett, A.W. Bhuiya, C.E. Botez, Dynamic susceptibility evidence of surface spin freezing in ultrafine $NiFe_2O$= nanoparticles., Nanotechnology. 20 (2009). doi:10.1088/0957-4484/20/44/445705.
[56] F.T. Parker, M.W. Foster, D.T. Margulies, A.E. Berkowitz, Spin canting, surface magnetization, and finite-size effects in γ-Fe_2O_3 particles, Phys. Rev. B. (1993). doi:10.1103/PhysRevB.47.7885.
[57] M.A. Bah, G.H. Jaffari, S.I. Shah, Surface effects on the exchange bias and magnetic irreversibility in hollow polycrystalline $NiFe_2O_4$ nanoparticles, Surf. Coatings Technol. (2017) 1–6. doi:10.1016/j.surfcoat.2017.01.018.
[58] Z. Nemati, H. Khurshid, J. Alonso, M. H. Phan, P. Mukherjee, H. Srikanth, From core/shell to hollow Fe/ γ-Fe_2O_3 nanoparticles: evolution of the magnetic behavior, Nanotechnology. 26 (2015) 405705. doi:10.1088/0957-4484/26/40/405705.
[59] K.M. Nam, J.H. Shim, D.W. Han, H.S. Kwon, Y.M. Kang, Y. Li, et al., Syntheses and characterization of wurtzite CoO, rocksalt CoO, and spinel Co_3O_4 nanocrystals: Their interconversion and tuning of phase and morphology, Chem. Mater. (2010). doi:10.1021/cm101138h.
[60] J. BERGSTRÖM, Oxidation of Cobalt Nanocrystals: Investigation of the Role of Nanocrystallinity, Self-Ordering and Nanocrystal Size, PhD Thesis. (2013). http://publications.lib.chalmers.se/records/fulltext/179402/179402.pdf.
[61] M. Li, Y.-X. Yin, C. Li, F. Zhang, L.-J. Wan, S. Xu, et al., Well-dispersed bi-component-active CoO/$CoFe_2O_4$ nanocomposites with tunable performances as anode materials for lithium-ion batteries, Chem. Commun. 48 (2012) 410. doi:10.1039/c1cc15322f.
[62] M. Ghosh, E. V. Sampathkumaran, C.N.R. Rao, Synthesis and magnetic properties of CoO nanoparticles, Chem. Mater. 17 (2005) 2348–2352. doi:10.1021/cm0478475.
[63] H. Ahmadvand, S.R. Safdari, A. Nozad Golikand, P. Dasgupta, A. Poddar, H. Salamati, Exchange bias in Co/CoO/Co_3O_4 nanostructures, J. Magn. Magn. Mater. 377 (2015) 19–23. doi:10.1016/j.jmmm.2014.10.021.
[64] a. López-Ortega, M. Estrader, G. Salazar-Alvarez, A.G. Roca, J. Nogués, Applications of exchange coupled bi-magnetic hard/soft and soft/hard magnetic core/shell nanoparticles, Phys. Rep. (2014). doi:10.1016/j.physrep.2014.09.007.
[65] J. Sort, S. Suriñach, J. Muñoz, M. Baró, J. Nogués, G. Chouteau, V. Skumryev, G. Hadjipanayis, Improving the energy product of hard magnetic materials, Phys. Rev. B. 65 (2002) 174420. doi:10.1103/PhysRevB.65.174420.
[66] H. Khurshid, P. Lampen-Kelley, Ò. Iglesias, J. Alonso, M.-H. Phan, C.-J. Sun, M.-L Saboungi, H. Srikanth, Spin-glass-like freezing of inner and outer surface layers in hollow γ-Fe_2O_3 nanoparticles., Sci. Rep. 5 (2015) 15054. doi:10.1038/srep15054.
[67] M. Hansen, C. Koch, S. Mørup, Magnetic dynamics of weakly and strongly interacting hematite nanoparticles, Phys. Rev. B. 62 (2000) 1124–1135. doi:10.1103/PhysRevB.62.1124.

[68] B. Martínez, X. Obradors, L. Balcells, A. Rouanet, C. Monty, Low Temperature Surface Spin-Glass Transition in γ- Fe_2O_3 Nanoparticles, Phys. Rev. Lett. 80 (1998) 181–184. doi:10.1103/PhysRevLett.80.181.
[69] S.R. Ali, M.R. Ghadimi, M. Fecioru-Morariu, B. Beschoten, G. Güntherodt, Training effect of the exchange bias in Co/CoO bilayers originates from the irreversible thermoremanent magnetization of the magnetically diluted antiferromagnet, Phys. Rev. B. 85 (2012) 12404. doi:10.1103/PhysRevB.85.012404.
[70] M.R. Ghadimi, B. Beschoten, G. Güntherodt, Role of structural defects on exchange bias in the epitaxial CoO⁄Co system, Appl. Phys. Lett. 87 (2005) 261903. doi:10.1063/1.2152111.
[71] M. Fecioru-Morariu, S.R. Ali, C. Papusoi, M. Sperlich, G. Güntherodt, Effects of Cu Dilution in IrMn on the Exchange Bias of CoFe/IrMn Bilayers, Phys. Rev. Lett. 99 (2007) 97206. doi:10.1103/PhysRevLett.99.097206.
[72] L.C. Sampaio, A. Mougin, J. Ferré, P. Georges, A. Brun, H. Bernas, Probing interface magnetism in the FeMn/NiFe exchange bias system using magnetic second-harmonic generation, Europhys. Lett. 63 (2003) 819–825. doi:10.1209/epl/i2003-00598-7.
[73] R. Morales, Z.-P. Li, J. Olamit, K. Liu, J.M. Alameda, I.K. Schuller, Role of the Antiferromagnetic Bulk Spin Structure on Exchange Bias, Phys. Rev. Lett. 102 (2009) 97201. doi:10.1103/PhysRevLett.102.097201.
[74] V. Šepelák, I. Bergmann, A. Feldhoff, P. Heitjans, F. Krumeich, D. Menzel, Nanocrystalline Nickel Ferrite , $NiFe_2O_4$: Mechanosynthesis , Nonequilibrium Cation Distribution , Canted Spin Arrangement , and Magnetic Behavior, J. Phys. Chem. C. 111 (2007) 5026–5033. doi:10.1021/jp067620s.
[75] A. E. BERKOWITZ AND W. J. SCHUELE, Influence of Crystallite Size on the magnetic Properties of Acicular γ-Fe_2O_3 Particles - Jofappliedphysics-39-1261-1968 DOI - 1-1656256, J. Appl. Phys. 39 (1968). doi:10.1063/1.1656256.

Chapter 7

CONCLUSIONS AND RECOMMENDATION

7.1 Conclusions

In this PhD study, detailed studies on the synthesis and characterization of polycrystalline hollow nanoparticles with different compositions are presented. Metallic nanoparticles were grown by inert gas condensation (IGC). A post-synthesis *ex situ* heat treatment, where necessary, was performed to obtained polycrystalline hollow morphology along with the desired composition where necessary. Extensive results on the magnetic properties of three different nanoparticles systems are presented:

1. Polycrystalline hollow $NiFe_2O_4$ nanoparticles
2. Polycrystalline hollow γ-Mn_2O_3 and MnO nanoparticles
3. Polycrystalline hollow $CoO/Co_3O_4/CoFe_2O_4$ nanoparticles

In the first system, examination of the magnetic properties of $NiFe_2O_4$ revealed the presence of large disordered spins located both at the inner and outer surfaces of the hollow nanoparticles and at the interfaces between crystallographic domains. The presence of the large disorder spins was found to have a strong effect on the exchange bias and overall effective anisotropy of the nanoparticles. Coercivity and exchange bias values from temperature and cooling field dependent hysteresis loops indicated strong ferrimagnetic and disordered surface spins coupling. Coercivity decreased as a function of temperature but never vanished up to the maximum temperature investigated. Coercivity did, however, increase with increasing cooling field.

Exchange bias was found to decrease in both the temperature and field dependent measurements where the trend was opposite to that of the change in coercivity. Magnetic irreversibility was found to persist at low temperatures as a function of cooling field. We have concluded that the strong coupling between the ferrimagnetic phase and the disordered surface spins is responsible for the observed behavior.

To explore the effect of having an antiferromagnetic phase along with a ferromagnetic phase in polycrystalline nanoparticles, we evaporated manganese palettes by IGC and studied the magnetic response of polycrystalline hollow multi oxide nanoparticles. Manganese was used to have multiple oxides in a single nanoparticle. Manganese is known for being easily oxidizable forming four stable oxide, among which two are antiferromagnetic (MnO and MnO_2) and two are ferrimagnetic (Mn_2O_3 and Mn_3O_4). Nanoparticles having both antiferromagnetic (MnO) and ferrimagnetic (γ-Mn_2O_3) phases with polycrystalline hollow morphology were successfully synthesized. Magnetic measurements of these nanoparticles revealed that coupling between the two magnetic phases along with coupling of the magnetic phase and the disordered surface spins has a significant effect on the coercivity and exchange bias, compared to behavior of conventional core/shell and solid nanoparticles. Coercivity increased and exchange bias decreased as a function of cooling field. However, as a function of temperature both decreased as the temperature approached the paramagnetic phase transition of the ferrimagnetic component. Magnetic irreversibility decreased as a function of the cooling field.

The relative ratios of the antiferromagnetic and ferrimagnetic phase cannot be easily controlled in the manganese oxide system. At higher annealing conditions (temperature and time) MnO phase vanishes. To probe the effect of the added antiferromagnetic phase, a cobalt oxide and cobalt iron oxide system was used. Polycrystalline hollow nanoparticles with various ratios of cobalt oxide and cobalt iron oxide were prepared and investigated. Cobalt has two stable oxides, CoO and Co_3O_4. Three different samples with increasing amount of Co_3O_4 phase revealed that magnetic reversibility was independent of the amount of the antiferromagnetic content. With the increase in Co_3O_4, it is understood that the relative amount of cobalt iron oxide phase, which is the magnetic ferrimagnetic phase, concentration decreases. The relative decrease of the cobalt iron oxide phase has been characterized by the decrease in the overall magnetization as a function of cobalt concentration. Therefore, the lack of correlation between the magnetic reversibility and the decrease in cobalt iron oxide phase indicates increase in coupling between the ferromagnetic phase and antiferromagnetic phase as a function of cobalt concentration. The observed decrease in coercivity confirms both the increase of the antiferromagnetic phase and the decrease in size of the ferrimagnetic phase. However, a nonmonotonic behavior of the exchange bias was observed with the change in the cobalt concentration, which is somewhat counterintuitive. Strong coupling typically leads to high exchange bias values. Therefore, it should be expected, since coupling increase with antiferromagnetic phase, that exchange bias should increase with cobalt concentration which it did not. This is most probably due to the lower anisotropy constant of Co_3O_4 compared to that of CoO phase that could lead to an overall decrease in the anisotropy as a function of cobalt concentration.

7.2 Recommendation

As one can notice in the last investigated system, mismatch between the anisotropy constant of Co_3O_4 and CoO could be the reason behind the nonmonotonic behavior of the exchange bias. Investigation of a system where a single antiferromagnetic oxide and ferromagnetic could help confirm this effect. Although speculations have been made in this thesis to the reason for the nonmonotonic behavior, confirming this could yield a greater understanding of the coupling effect of the two magnetic phases in polycrystalline hollow nanoparticles. Systems such as chromium oxide could be investigated, where stable CrO_2 (ferromagnetic) and Cr_2O_3 (antiferromagnetic) are obtained by the decomposition of CrO_3. However, very few studies exist on the synthesis of CrO_2 by oxidation of chromium metal although it has been suggested that CrO_2 synthesis is possible by heating chromium metal under high pressure of oxygen. Therefore, chromium metal nanoparticles could be obtained by the evaporation of bulk chromium in an Inert gas condensation (IGC) system. The obtained nanoparticles could then be annealed under high oxygen pressure conditions to obtain CrO_2. The challenge of this process could come from the annealing conditions. It has been shown that very high pressures are needed to obtain CrO_2. If the growth of such system is possible, a clear conclusion could be made regarding the exact influence of the antiferromagnetic phase coupling on the magnetic properties of polycrystalline hollow nanoparticles.

Appendix

LIST OF PUBLICATIONS

1. **Mohamed A. Bah**, G. Hassnain Jaffari, and S. Ismat Shah "Coercivity and exchange bias in polycrystalline hollow CoO, Co_3O_4 and $CoFe_2O_4$ nanoparticles." (To be submitted)
2. **Mohamed A. Bah**, G. Hassnain Jaffari, and S. Ismat Shah "Surface effects on the exchange bias and magnetic irreversibility in hollow polycrystalline $NiFe_2O_4$ nanoparticles"., Surface and Coatings Technology · January 2017, DOI: 10.1016/j.surfcoat.2017.01.018
3. G. Hassnain Jaffari, Ali Imran, **Mohamed A. Bah**, Awais Ali, Arshad S. Bhatti, Umar Saeed Qurashi and S. Ismat Shah "Identification and quantification of oxygen vacancies in CeO_2 nanocrystals and their role in formation of F-centers", Applied Surface Science · October 2016, DOI: 10.1016/j.apsusc.2016.10.193
4. Zuhal Onuk, Nopporn Rujisamphan, **Mohamed A. Bah**, Roy Murray, Tomakin Murat, and S. Ismat Shah "Controllable Growth and Characterization of Highly Aligned ZnO Nanocolumnar Thin Films" Applied Surface Science · November 2016, DOI: 10.1016/j.apsusc.2016.11.190
5. Anitha Ravikrishnan, Tugba Ozdemir, **Mohamed A. Bah**, Karen A Baskerville, Ismat Shah, Ayyappan K Rajasekaran, Xinqiao Jia "Fiber Diameter Meditates Epithelial-to-Mesenchymal Transition in Kidney

Epithelial Cells”, ACS Applied Materials & Interfaces · June 2016, DOI: 10.1021/acsami.6b05646

6. **Mohamed A. Bah**, G. Hassnain Jaffari, F. A. Khan, and S. Ismat Shah “Exchange bias in polycrystalline hollow nanoparticles composed of γ-Mn_2O_3 and MnO nanocrystallites”., Applied Surface Science (2016), DOI: 10.1016/j.apsusc.2016.02.145
7. K. Navaneetha, M.C. RamKumar, A. Arun Kumar, P.V.A. Padmanabhan, R.R. Deshmukh, **M. Bah**, S. Ismat Shah, P.-G. Su, A. S. Halim, “Tailoring the surface properties of polypropylene films through cold atmospheric pressure (CAPP) plasma assisted polymerization and immobilization of biomolecules for enhancement of anti-coagulation activity”, Applied Surface Science (2016), ttp://dx.doi.org/10.1016/j.apsusc.2016.02.137
8. G. Hassnain Jaffari, Adnan Tahir, **Mohamed A. Bah**, Awais Ali, Arshad S Bhatti, S Ismat Shah, “Study of Surface-Active Modes and Defects in Single-Phase Li-Incorporated MgO Nanoparticles” The Journal of Physical Chemistry C 119 (2015) 28182-28189
9. G. Hassnain Jaffari, Abdul K. Rumaiz, C. Ni, Emre Yassitepe, **M. Bah**, S. Ismat Shah “Observation of metastable phase separation and amorphous phase in $Fe_{67}Co_{33}$ alloy thin films synthesized by pulsed laser depositions”. Current Applied Physics 15 (2015) 717 – 721
10. Campanella A., Wool R.P., **Bah M. A.**, Fita S., Abuobaid A, (2013) “Composites from northern red oak (Quercus robur) leaves and plant oil-based resins”. Applied Polymer Science 127(1)18–26

REPRINT PERMISSION LETTERS

Permission letters attached.

JOHN WILEY AND SONS LICENSE
TERMS AND CONDITIONS

May 02, 2017

This Agreement between Mohamed A Bah ("You") and John Wiley and Sons ("John Wiley and Sons") consists of your license details and the terms and conditions provided by John Wiley and Sons and Copyright Clearance Center.

License Number	4100900109064
License date	
Licensed Content Publisher	John Wiley and Sons
Licensed Content Publication	Wiley oBooks
Licensed Content Title	Magnetic Relaxation in Fine-Particle Systems
Licensed Content Author	J. L. Dormann,D. Fiorani,E. Tronc
Licensed Content Date	Mar 14, 2007
Licensed Content Pages	212
Type of use	Dissertation/Thesis
Requestor type	University/Academic
Format	Print and electronic
Portion	Figure/table
Number of figures/tables	1
Original Wiley figure/table number(s)	Figure
Will you be translating?	No
Title of your thesis / dissertation	COERCIVITY AND EXCHANGE BIAS STUDY OF POLYCRYSTALLINE HOLLOW NANOPARTICLES
Expected completion date	May 2017
Expected size (number of pages)	130
Requestor Location	Mohamed A Bah 630 Capitol Trail Apt G4 NEWARK, DE 19711 United States Attn: Mohamed A Bah
Publisher Tax ID	EU826007151
Billing Type	Invoice
Billing Address	Mohamed A Bah 630 Capitol Trail Apt G4 NEWARK, DE 19711 United States Attn: Mohamed A Bah

Total 0.00 USD

Terms and Conditions

TERMS AND CONDITIONS

This copyrighted material is owned by or exclusively licensed to John Wiley & Sons, Inc. or one of its group companies (each a"Wiley Company") or handled on behalf of a society with which a Wiley Company has exclusive publishing rights in relation to a particular work (collectively "WILEY"). By clicking "accept" in connection with completing this licensing transaction, you agree that the following terms and conditions apply to this transaction (along with the billing and payment terms and conditions established by the Copyright Clearance Center Inc., ("CCC's Billing and Payment terms and conditions"), at the time that you opened your RightsLink account (these are available at any time at http://myaccount.copyright.com).

Terms and Conditions

- The materials you have requested permission to reproduce or reuse (the "Wiley Materials") are protected by copyright.

- You are hereby granted a personal, non-exclusive, non-sub licensable (on a stand-alone basis), non-transferable, worldwide, limited license to reproduce the Wiley Materials for the purpose specified in the licensing process. This license, **and any CONTENT (PDF or image file) purchased as part of your order,** is for a one-time use only and limited to any maximum distribution number specified in the license. The first instance of republication or reuse granted by this license must be completed within two years of the date of the grant of this license (although copies prepared before the end date may be distributed thereafter). The Wiley Materials shall not be used in any other manner or for any other purpose, beyond what is granted in the license. Permission is granted subject to an appropriate acknowledgement given to the author, title of the material/book/journal and the publisher. You shall also duplicate the copyright notice that appears in the Wiley publication in your use of the Wiley Material. Permission is also granted on the understanding that nowhere in the text is a previously published source acknowledged for all or part of this Wiley Material. Any third party content is expressly excluded from this permission.

- With respect to the Wiley Materials, all rights are reserved. Except as expressly granted by the terms of the license, no part of the Wiley Materials may be copied, modified, adapted (except for minor reformatting required by the new Publication), translated, reproduced, transferred or distributed, in any form or by any means, and no derivative works may be made based on the Wiley Materials without the prior permission of the respective copyright owner.**For STM Signatory Publishers clearing permission under the terms of the STM Permissions Guidelines only, the terms of the license are extended to include subsequent editions and for editions in other languages, provided such editions are for the work as a whole in situ and does not involve the separate exploitation of the permitted figures or extracts,** You may not alter, remove or suppress in any manner any copyright, trademark or other notices displayed by the Wiley Materials. You may not license, rent, sell, loan, lease, pledge, offer as security, transfer or assign the Wiley Materials on a stand-alone basis, or any of the rights granted to you hereunder to any other person.

- The Wiley Materials and all of the intellectual property rights therein shall at all times remain the exclusive property of John Wiley & Sons Inc, the Wiley Companies, or their respective licensors, and your interest therein is only that of having possession of and the right to reproduce the Wiley Materials pursuant to Section 2 herein during the continuance of this Agreement. You agree that you own no right, title or interest in or to the Wiley Materials or any of the intellectual property rights therein. You shall have no rights hereunder other than the license as provided for above in Section 2. No right, license or interest to any trademark, trade name, service mark or other branding ("Marks") of WILEY or its licensors is granted hereunder, and you agree that you shall not assert any such right, license or interest with respect thereto

- NEITHER WILEY NOR ITS LICENSORS MAKES ANY WARRANTY OR REPRESENTATION OF ANY KIND TO YOU OR ANY THIRD PARTY, EXPRESS, IMPLIED OR STATUTORY, WITH RESPECT TO THE MATERIALS OR THE ACCURACY OF ANY INFORMATION CONTAINED IN THE MATERIALS, INCLUDING, WITHOUT LIMITATION, ANY IMPLIED WARRANTY OF MERCHANTABILITY, ACCURACY, SATISFACTORY QUALITY, FITNESS FOR A PARTICULAR PURPOSE, USABILITY, INTEGRATION OR NON-INFRINGEMENT AND ALL SUCH WARRANTIES ARE HEREBY EXCLUDED BY WILEY AND ITS LICENSORS AND WAIVED BY YOU.

- WILEY shall have the right to terminate this Agreement immediately upon breach of this Agreement by you.

- You shall indemnify, defend and hold harmless WILEY, its Licensors and their respective directors, officers, agents and employees, from and against any actual or threatened claims, demands, causes of action or proceedings arising from any breach of this Agreement by you.

- IN NO EVENT SHALL WILEY OR ITS LICENSORS BE LIABLE TO YOU OR ANY OTHER PARTY OR ANY OTHER PERSON OR ENTITY FOR ANY SPECIAL, CONSEQUENTIAL, INCIDENTAL, INDIRECT, EXEMPLARY OR PUNITIVE DAMAGES, HOWEVER CAUSED, ARISING OUT OF OR IN CONNECTION WITH THE DOWNLOADING, PROVISIONING, VIEWING OR USE OF THE MATERIALS REGARDLESS OF THE FORM OF ACTION, WHETHER FOR BREACH OF CONTRACT, BREACH OF WARRANTY, TORT, NEGLIGENCE, INFRINGEMENT OR OTHERWISE (INCLUDING, WITHOUT LIMITATION, DAMAGES BASED ON LOSS OF PROFITS, DATA, FILES, USE, BUSINESS OPPORTUNITY OR CLAIMS OF THIRD PARTIES), AND WHETHER OR NOT THE PARTY HAS BEEN ADVISED OF THE POSSIBILITY OF SUCH DAMAGES. THIS LIMITATION SHALL APPLY NOTWITHSTANDING ANY FAILURE OF ESSENTIAL PURPOSE OF ANY LIMITED REMEDY PROVIDED HEREIN.

- Should any provision of this Agreement be held by a court of competent jurisdiction to be illegal, invalid, or unenforceable, that provision shall be deemed amended to achieve as nearly as possible the same economic effect as the original provision, and the legality, validity and enforceability of the remaining provisions of this Agreement shall not be affected or impaired thereby.

- The failure of either party to enforce any term or condition of this Agreement shall not constitute a waiver of either party's right to enforce each and every term and condition of this Agreement. No breach under this agreement shall be deemed waived or excused by either party unless such waiver or consent is in writing signed by the party granting such waiver or consent. The waiver by or consent of a party to a breach of any provision of this Agreement shall not operate or be construed as a waiver of or consent to any other or subsequent breach by such other party.

- This Agreement may not be assigned (including by operation of law or otherwise) by you without WILEY's prior written consent.

- Any fee required for this permission shall be non-refundable after thirty (30) days from receipt by the CCC.

- These terms and conditions together with CCC's Billing and Payment terms and conditions (which are incorporated herein) form the entire agreement between you and WILEY concerning this licensing transaction and (in the absence of fraud) supersedes all prior agreements and representations of the parties, oral or written. This Agreement may not be amended except in writing signed by both parties. This Agreement shall be binding upon and inure to the benefit of the parties' successors, legal representatives, and authorized assigns.

- In the event of any conflict between your obligations established by these terms and conditions and those established by CCC's Billing and Payment terms and conditions, these terms and conditions shall prevail.

- WILEY expressly reserves all rights not specifically granted in the combination of (i) the license details provided by you and accepted in the course of this licensing transaction, (ii) these terms and conditions and (iii) CCC's Billing and Payment terms and conditions.

- This Agreement will be void if the Type of Use, Format, Circulation, or Requestor Type was misrepresented during the licensing process.

- This Agreement shall be governed by and construed in accordance with the laws of the State of New York, USA, without regards to such state's conflict of law rules. Any legal action, suit or proceeding arising out of or relating to these Terms and Conditions or the breach thereof shall be instituted in a court of competent jurisdiction in New York County in the State of New York in the United States of America and each party hereby consents and submits to the personal jurisdiction of such court, waives any objection to venue in such court and consents to service of process by registered or

ELSEVIER LICENSE
TERMS AND CONDITIONS

May 02, 2017

This Agreement between Mohamed A Bah ("You") and Elsevier ("Elsevier") consists of your license details and the terms and conditions provided by Elsevier and Copyright Clearance Center.

License Number	4100891474261
License date	
Licensed Content Publisher	Elsevier
Licensed Content Publication	Journal of Magnetism and Magnetic Materials
Licensed Content Title	Exchange bias
Licensed Content Author	J Nogués,Ivan K Schuller
Licensed Content Date	15 February 1999
Licensed Content Volume	192
Licensed Content Issue	2
Licensed Content Pages	30
Start Page	203
End Page	232
Type of Use	reuse in a thesis/dissertation
Portion	figures/tables/illustrations
Number of figures/tables /illustrations	1
Format	both print and electronic
Are you the author of this Elsevier article?	No
Will you be translating?	No
Order reference number	
Original figure numbers	
Title of your thesis/dissertation	COERCIVITY AND EXCHANGE BIAS STUDY OF POLYCRYSTALLINE HOLLOW NANOPARTICLES
Expected completion date	May 2017
Estimated size (number of pages)	130
Elsevier VAT number	GB 494 6272 12
Requestor Location	Mohamed A Bah 630 Capitol Trail Apt G4 NEWARK, DE 19711 United States Attn: Mohamed A Bah

Publisher Tax ID	98-0397604
Total	0.00 USD

Terms and Conditions

INTRODUCTION

1. The publisher for this copyrighted material is Elsevier. By clicking "accept" in connection with completing this licensing transaction, you agree that the following terms and conditions apply to this transaction (along with the Billing and Payment terms and conditions established by Copyright Clearance Center, Inc. ("CCC"), at the time that you opened your Rightslink account and that are available at any time at http://myaccount.copyright.com).

GENERAL TERMS

2. Elsevier hereby grants you permission to reproduce the aforementioned material subject to the terms and conditions indicated.
3. Acknowledgement: If any part of the material to be used (for example, figures) has appeared in our publication with credit or acknowledgement to another source, permission must also be sought from that source. If such permission is not obtained then that material may not be included in your publication/copies. Suitable acknowledgement to the source must be made, either as a footnote or in a reference list at the end of your publication, as follows:
"Reprinted from Publication title, Vol /edition number, Author(s), Title of article / title of chapter, Pages No., Copyright (Year), with permission from Elsevier [OR APPLICABLE SOCIETY COPYRIGHT OWNER]." Also Lancet special credit - "Reprinted from The Lancet, Vol. number, Author(s), Title of article, Pages No., Copyright (Year), with permission from Elsevier."
4. Reproduction of this material is confined to the purpose and/or media for which permission is hereby given.
5. Altering/Modifying Material: Not Permitted. However figures and illustrations may be altered/adapted minimally to serve your work. Any other abbreviations, additions, deletions and/or any other alterations shall be made only with prior written authorization of Elsevier Ltd. (Please contact Elsevier at permissions@elsevier.com). No modifications can be made to any Lancet figures/tables and they must be reproduced in full.
6. If the permission fee for the requested use of our material is waived in this instance, please be advised that your future requests for Elsevier materials may attract a fee.
7. Reservation of Rights: Publisher reserves all rights not specifically granted in the combination of (i) the license details provided by you and accepted in the course of this licensing transaction, (ii) these terms and conditions and (iii) CCC's Billing and Payment terms and conditions.
8. License Contingent Upon Payment: While you may exercise the rights licensed immediately upon issuance of the license at the end of the licensing process for the transaction, provided that you have disclosed complete and accurate details of your proposed use, no license is finally effective unless and until full payment is received from you (either by publisher or by CCC) as provided in CCC's Billing and Payment terms and conditions. If full payment is not received on a timely basis, then any license preliminarily granted shall be deemed automatically revoked and shall be void as if never granted. Further, in the event that you breach any of these terms and conditions or any of CCC's Billing and Payment terms and conditions, the license is automatically revoked and shall be void as if never

granted. Use of materials as described in a revoked license, as well as any use of the materials beyond the scope of an unrevoked license, may constitute copyright infringement and publisher reserves the right to take any and all action to protect its copyright in the materials.

9. Warranties: Publisher makes no representations or warranties with respect to the licensed material.

10. Indemnity: You hereby indemnify and agree to hold harmless publisher and CCC, and their respective officers, directors, employees and agents, from and against any and all claims arising out of your use of the licensed material other than as specifically authorized pursuant to this license.

11. No Transfer of License: This license is personal to you and may not be sublicensed, assigned, or transferred by you to any other person without publisher's written permission.

12. No Amendment Except in Writing: This license may not be amended except in a writing signed by both parties (or, in the case of publisher, by CCC on publisher's behalf).

13. Objection to Contrary Terms: Publisher hereby objects to any terms contained in any purchase order, acknowledgment, check endorsement or other writing prepared by you, which terms are inconsistent with these terms and conditions or CCC's Billing and Payment terms and conditions. These terms and conditions, together with CCC's Billing and Payment terms and conditions (which are incorporated herein), comprise the entire agreement between you and publisher (and CCC) concerning this licensing transaction. In the event of any conflict between your obligations established by these terms and conditions and those established by CCC's Billing and Payment terms and conditions, these terms and conditions shall control.

14. Revocation: Elsevier or Copyright Clearance Center may deny the permissions described in this License at their sole discretion, for any reason or no reason, with a full refund payable to you. Notice of such denial will be made using the contact information provided by you. Failure to receive such notice will not alter or invalidate the denial. In no event will Elsevier or Copyright Clearance Center be responsible or liable for any costs, expenses or damage incurred by you as a result of a denial of your permission request, other than a refund of the amount(s) paid by you to Elsevier and/or Copyright Clearance Center for denied permissions.

LIMITED LICENSE

The following terms and conditions apply only to specific license types:

15. **Translation**: This permission is granted for non-exclusive world **English** rights only unless your license was granted for translation rights. If you licensed translation rights you may only translate this content into the languages you requested. A professional translator must perform all translations and reproduce the content word for word preserving the integrity of the article.

16. **Posting licensed content on any Website**: The following terms and conditions apply as follows: Licensing material from an Elsevier journal: All content posted to the web site must maintain the copyright information line on the bottom of each image; A hyper-text must be included to the Homepage of the journal from which you are licensing at http://www.sciencedirect.com/science/journal/xxxxx or the Elsevier homepage for books at http://www.elsevier.com; Central Storage: This license does not include permission for a scanned version of the material to be stored in a central repository such as that provided by Heron/XanEdu.

Licensing material from an Elsevier book: A hyper-text link must be included to the Elsevier homepage at http://www.elsevier.com . All content posted to the web site must maintain the copyright information line on the bottom of each image.

Posting licensed content on Electronic reserve: In addition to the above the following clauses are applicable: The web site must be password-protected and made available only to bona fide students registered on a relevant course. This permission is granted for 1 year only. You may obtain a new license for future website posting.
17. **For journal authors:** the following clauses are applicable in addition to the above:
Preprints:
A preprint is an author's own write-up of research results and analysis, it has not been peer-reviewed, nor has it had any other value added to it by a publisher (such as formatting, copyright, technical enhancement etc.).
Authors can share their preprints anywhere at any time. Preprints should not be added to or enhanced in any way in order to appear more like, or to substitute for, the final versions of articles however authors can update their preprints on arXiv or RePEc with their Accepted Author Manuscript (see below).
If accepted for publication, we encourage authors to link from the preprint to their formal publication via its DOI. Millions of researchers have access to the formal publications on ScienceDirect, and so links will help users to find, access, cite and use the best available version. Please note that Cell Press, The Lancet and some society-owned have different preprint policies. Information on these policies is available on the journal homepage.
Accepted Author Manuscripts: An accepted author manuscript is the manuscript of an article that has been accepted for publication and which typically includes author-incorporated changes suggested during submission, peer review and editor-author communications.
Authors can share their accepted author manuscript:

- immediately
  - via their non-commercial person homepage or blog
  - by updating a preprint in arXiv or RePEc with the accepted manuscript
  - via their research institute or institutional repository for internal institutional uses or as part of an invitation-only research collaboration work-group
  - directly by providing copies to their students or to research collaborators for their personal use
  - for private scholarly sharing as part of an invitation-only work group on commercial sites with which Elsevier has an agreement
- After the embargo period
  - via non-commercial hosting platforms such as their institutional repository
  - via commercial sites with which Elsevier has an agreement

In all cases accepted manuscripts should:

- link to the formal publication via its DOI
- bear a CC-BY-NC-ND license - this is easy to do
- if aggregated with other manuscripts, for example in a repository or other site, be shared in alignment with our hosting policy not be added to or enhanced in any way to appear more like, or to substitute for, the published journal article.

Published journal article (JPA): A published journal article (PJA) is the definitive final record of published research that appears or will appear in the journal and embodies all value-adding publishing activities including peer review co-ordination, copy-editing, formatting, (if relevant) pagination and online enrichment.
Policies for sharing publishing journal articles differ for subscription and gold open access articles:
Subscription Articles: If you are an author, please share a link to your article rather than the full-text. Millions of researchers have access to the formal publications on ScienceDirect, and so links will help your users to find, access, cite, and use the best available version.
Theses and dissertations which contain embedded PJAs as part of the formal submission can be posted publicly by the awarding institution with DOI links back to the formal publications on ScienceDirect.
If you are affiliated with a library that subscribes to ScienceDirect you have additional private sharing rights for others' research accessed under that agreement. This includes use for classroom teaching and internal training at the institution (including use in course packs and courseware programs), and inclusion of the article for grant funding purposes.
Gold Open Access Articles: May be shared according to the author-selected end-user license and should contain a CrossMark logo, the end user license, and a DOI link to the formal publication on ScienceDirect.
Please refer to Elsevier's posting policy for further information.
18. **For book authors** the following clauses are applicable in addition to the above: Authors are permitted to place a brief summary of their work online only. You are not allowed to download and post the published electronic version of your chapter, nor may you scan the printed edition to create an electronic version. **Posting to a repository:** Authors are permitted to post a summary of their chapter only in their institution's repository.
19. **Thesis/Dissertation**: If your license is for use in a thesis/dissertation your thesis may be submitted to your institution in either print or electronic form. Should your thesis be published commercially, please reapply for permission. These requirements include permission for the Library and Archives of Canada to supply single copies, on demand, of the complete thesis and include permission for Proquest/UMI to supply single copies, on demand, of the complete thesis. Should your thesis be published commercially, please reapply for permission. Theses and dissertations which contain embedded PJAs as part of the formal submission can be posted publicly by the awarding institution with DOI links back to the formal publications on ScienceDirect.

Elsevier Open Access Terms and Conditions
You can publish open access with Elsevier in hundreds of open access journals or in nearly 2000 established subscription journals that support open access publishing. Permitted third party re-use of these open access articles is defined by the author's choice of Creative Commons user license. See our open access license policy for more information.
Terms & Conditions applicable to all Open Access articles published with Elsevier:
Any reuse of the article must not represent the author as endorsing the adaptation of the article nor should the article be modified in such a way as to damage the author's honour or reputation. If any changes have been made, such changes must be clearly indicated.
The author(s) must be appropriately credited and we ask that you include the end user license and a DOI link to the formal publication on ScienceDirect.
If any part of the material to be used (for example, figures) has appeared in our publication

ELSEVIER LICENSE
TERMS AND CONDITIONS

May 02, 2017

This Agreement between Mohamed A Bah ("You") and Elsevier ("Elsevier") consists of your license details and the terms and conditions provided by Elsevier and Copyright Clearance Center.

License Number	4100800442844
License date	
Licensed Content Publisher	Elsevier
Licensed Content Publication	Surface and Coatings Technology
Licensed Content Title	Surface effects on the exchange bias and magnetic irreversibility in hollow polycrystalline NiFe2O4 nanoparticles
Licensed Content Author	Mohamed A. Bah,G. Hassnain Jaffari,S. Ismat Shah
Licensed Content Date	25 March 2017
Licensed Content Volume	314
Licensed Content Issue	n/a
Licensed Content Pages	6
Start Page	35
End Page	40
Type of Use	reuse in a thesis/dissertation
Portion	full article
Format	both print and electronic
Are you the author of this Elsevier article?	Yes
Will you be translating?	No
Order reference number	
Title of your thesis/dissertation	COERCIVITY AND EXCHANGE BIAS STUDY OF POLYCRYSTALLINE HOLLOW NANOPARTICLES
Expected completion date	May 2017
Estimated size (number of pages)	130
Elsevier VAT number	GB 494 6272 12
Requestor Location	Mohamed A Bah 630 Capitol Trail Apt G4 NEWARK, DE 19711 United States Attn: Mohamed A Bah
Publisher Tax ID	98-0397604
Total	0.00 USD

materials.
9. Warranties: Publisher makes no representations or warranties with respect to the licensed material.
10. Indemnity: You hereby indemnify and agree to hold harmless publisher and CCC, and their respective officers, directors, employees and agents, from and against any and all claims arising out of your use of the licensed material other than as specifically authorized pursuant to this license.
11. No Transfer of License: This license is personal to you and may not be sublicensed, assigned, or transferred by you to any other person without publisher's written permission.
12. No Amendment Except in Writing: This license may not be amended except in a writing signed by both parties (or, in the case of publisher, by CCC on publisher's behalf).
13. Objection to Contrary Terms: Publisher hereby objects to any terms contained in any purchase order, acknowledgment, check endorsement or other writing prepared by you, which terms are inconsistent with these terms and conditions or CCC's Billing and Payment terms and conditions. These terms and conditions, together with CCC's Billing and Payment terms and conditions (which are incorporated herein), comprise the entire agreement between you and publisher (and CCC) concerning this licensing transaction. In the event of any conflict between your obligations established by these terms and conditions and those established by CCC's Billing and Payment terms and conditions, these terms and conditions shall control.
14. Revocation: Elsevier or Copyright Clearance Center may deny the permissions described in this License at their sole discretion, for any reason or no reason, with a full refund payable to you. Notice of such denial will be made using the contact information provided by you. Failure to receive such notice will not alter or invalidate the denial. In no event will Elsevier or Copyright Clearance Center be responsible or liable for any costs, expenses or damage incurred by you as a result of a denial of your permission request, other than a refund of the amount(s) paid by you to Elsevier and/or Copyright Clearance Center for denied permissions.

LIMITED LICENSE

The following terms and conditions apply only to specific license types:
15. **Translation**: This permission is granted for non-exclusive world **English** rights only unless your license was granted for translation rights. If you licensed translation rights you may only translate this content into the languages you requested. A professional translator must perform all translations and reproduce the content word for word preserving the integrity of the article.
16. **Posting licensed content on any Website**: The following terms and conditions apply as follows: Licensing material from an Elsevier journal: All content posted to the web site must maintain the copyright information line on the bottom of each image; A hyper-text must be included to the Homepage of the journal from which you are licensing at http://www.sciencedirect.com/science/journal/xxxxx or the Elsevier homepage for books at http://www.elsevier.com; Central Storage: This license does not include permission for a scanned version of the material to be stored in a central repository such as that provided by Heron/XanEdu.
Licensing material from an Elsevier book: A hyper-text link must be included to the Elsevier homepage at http://www.elsevier.com . All content posted to the web site must maintain the copyright information line on the bottom of each image.

Posting licensed content on Electronic reserve: In addition to the above the following clauses are applicable: The web site must be password-protected and made available only to bona fide students registered on a relevant course. This permission is granted for 1 year only. You may obtain a new license for future website posting.
17. **For journal authors:** the following clauses are applicable in addition to the above:
Preprints:
A preprint is an author's own write-up of research results and analysis, it has not been peer-reviewed, nor has it had any other value added to it by a publisher (such as formatting, copyright, technical enhancement etc.).
Authors can share their preprints anywhere at any time. Preprints should not be added to or enhanced in any way in order to appear more like, or to substitute for, the final versions of articles however authors can update their preprints on arXiv or RePEc with their Accepted Author Manuscript (see below).
If accepted for publication, we encourage authors to link from the preprint to their formal publication via its DOI. Millions of researchers have access to the formal publications on ScienceDirect, and so links will help users to find, access, cite and use the best available version. Please note that Cell Press, The Lancet and some society-owned have different preprint policies. Information on these policies is available on the journal homepage.
Accepted Author Manuscripts: An accepted author manuscript is the manuscript of an article that has been accepted for publication and which typically includes author-incorporated changes suggested during submission, peer review and editor-author communications.
Authors can share their accepted author manuscript:

- immediately
  - via their non-commercial person homepage or blog
  - by updating a preprint in arXiv or RePEc with the accepted manuscript
  - via their research institute or institutional repository for internal institutional uses or as part of an invitation-only research collaboration work-group
  - directly by providing copies to their students or to research collaborators for their personal use
  - for private scholarly sharing as part of an invitation-only work group on commercial sites with which Elsevier has an agreement
- After the embargo period
  - via non-commercial hosting platforms such as their institutional repository
  - via commercial sites with which Elsevier has an agreement

In all cases accepted manuscripts should:

- link to the formal publication via its DOI
- bear a CC-BY-NC-ND license - this is easy to do
- if aggregated with other manuscripts, for example in a repository or other site, be shared in alignment with our hosting policy not be added to or enhanced in any way to appear more like, or to substitute for, the published journal article.

Published journal article (JPA): A published journal article (PJA) is the definitive final record of published research that appears or will appear in the journal and embodies all value-adding publishing activities including peer review co-ordination, copy-editing,

formatting, (if relevant) pagination and online enrichment.
Policies for sharing publishing journal articles differ for subscription and gold open access articles:
Subscription Articles: If you are an author, please share a link to your article rather than the full-text. Millions of researchers have access to the formal publications on ScienceDirect, and so links will help your users to find, access, cite, and use the best available version. Theses and dissertations which contain embedded PJAs as part of the formal submission can be posted publicly by the awarding institution with DOI links back to the formal publications on ScienceDirect.
If you are affiliated with a library that subscribes to ScienceDirect you have additional private sharing rights for others' research accessed under that agreement. This includes use for classroom teaching and internal training at the institution (including use in course packs and courseware programs), and inclusion of the article for grant funding purposes.
Gold Open Access Articles: May be shared according to the author-selected end-user license and should contain a CrossMark logo, the end user license, and a DOI link to the formal publication on ScienceDirect.
Please refer to Elsevier's posting policy for further information.
18. **For book authors** the following clauses are applicable in addition to the above: Authors are permitted to place a brief summary of their work online only. You are not allowed to download and post the published electronic version of your chapter, nor may you scan the printed edition to create an electronic version. **Posting to a repository:** Authors are permitted to post a summary of their chapter only in their institution's repository.
19. **Thesis/Dissertation**: If your license is for use in a thesis/dissertation your thesis may be submitted to your institution in either print or electronic form. Should your thesis be published commercially, please reapply for permission. These requirements include permission for the Library and Archives of Canada to supply single copies, on demand, of the complete thesis and include permission for Proquest/UMI to supply single copies, on demand, of the complete thesis. Should your thesis be published commercially, please reapply for permission. Theses and dissertations which contain embedded PJAs as part of the formal submission can be posted publicly by the awarding institution with DOI links back to the formal publications on ScienceDirect.

Elsevier Open Access Terms and Conditions
You can publish open access with Elsevier in hundreds of open access journals or in nearly 2000 established subscription journals that support open access publishing. Permitted third party re-use of these open access articles is defined by the author's choice of Creative Commons user license. See our open access license policy for more information.
Terms & Conditions applicable to all Open Access articles published with Elsevier:
Any reuse of the article must not represent the author as endorsing the adaptation of the article nor should the article be modified in such a way as to damage the author's honour or reputation. If any changes have been made, such changes must be clearly indicated.
The author(s) must be appropriately credited and we ask that you include the end user license and a DOI link to the formal publication on ScienceDirect.
If any part of the material to be used (for example, figures) has appeared in our publication with credit or acknowledgement to another source it is the responsibility of the user to ensure their reuse complies with the terms and conditions determined by the rights holder.
Additional Terms & Conditions applicable to each Creative Commons user license:

ELSEVIER LICENSE
TERMS AND CONDITIONS

May 02, 2017

This Agreement between Mohamed A Bah ("You") and Elsevier ("Elsevier") consists of your license details and the terms and conditions provided by Elsevier and Copyright Clearance Center.

License Number	4100800805975
License date	
Licensed Content Publisher	Elsevier
Licensed Content Publication	Applied Surface Science
Licensed Content Title	Surfaces and their effect on the magnetic properties of polycrystalline hollow γ-Mn2O3 and MnO nanoparticles
Licensed Content Author	Mohamed A. Bah,G. Hassnain Jaffari,F.A. Khan,S. Ismat Shah
Licensed Content Date	1 July 2016
Licensed Content Volume	375
Licensed Content Issue	n/a
Licensed Content Pages	8
Start Page	136
End Page	143
Type of Use	reuse in a thesis/dissertation
Intended publisher of new work	other
Portion	full article
Format	both print and electronic
Are you the author of this Elsevier article?	Yes
Will you be translating?	No
Order reference number	
Title of your thesis/dissertation	COERCIVITY AND EXCHANGE BIAS STUDY OF POLYCRYSTALLINE HOLLOW NANOPARTICLES
Expected completion date	May 2017
Estimated size (number of pages)	130
Elsevier VAT number	GB 494 6272 12
Requestor Location	Mohamed A Bah 630 Capitol Trail Apt G4 NEWARK, DE 19711 United States Attn: Mohamed A Bah

Publisher Tax ID	98-0397604
Total	0.00 USD

Terms and Conditions

INTRODUCTION

1. The publisher for this copyrighted material is Elsevier. By clicking "accept" in connection with completing this licensing transaction, you agree that the following terms and conditions apply to this transaction (along with the Billing and Payment terms and conditions established by Copyright Clearance Center, Inc. ("CCC"), at the time that you opened your Rightslink account and that are available at any time at http://myaccount.copyright.com).

GENERAL TERMS

2. Elsevier hereby grants you permission to reproduce the aforementioned material subject to the terms and conditions indicated.
3. Acknowledgement: If any part of the material to be used (for example, figures) has appeared in our publication with credit or acknowledgement to another source, permission must also be sought from that source. If such permission is not obtained then that material may not be included in your publication/copies. Suitable acknowledgement to the source must be made, either as a footnote or in a reference list at the end of your publication, as follows:
"Reprinted from Publication title, Vol /edition number, Author(s), Title of article / title of chapter, Pages No., Copyright (Year), with permission from Elsevier [OR APPLICABLE SOCIETY COPYRIGHT OWNER]." Also Lancet special credit - "Reprinted from The Lancet, Vol. number, Author(s), Title of article, Pages No., Copyright (Year), with permission from Elsevier."
4. Reproduction of this material is confined to the purpose and/or media for which permission is hereby given.
5. Altering/Modifying Material: Not Permitted. However figures and illustrations may be altered/adapted minimally to serve your work. Any other abbreviations, additions, deletions and/or any other alterations shall be made only with prior written authorization of Elsevier Ltd. (Please contact Elsevier at permissions@elsevier.com). No modifications can be made to any Lancet figures/tables and they must be reproduced in full.
6. If the permission fee for the requested use of our material is waived in this instance, please be advised that your future requests for Elsevier materials may attract a fee.
7. Reservation of Rights: Publisher reserves all rights not specifically granted in the combination of (i) the license details provided by you and accepted in the course of this licensing transaction, (ii) these terms and conditions and (iii) CCC's Billing and Payment terms and conditions.
8. License Contingent Upon Payment: While you may exercise the rights licensed immediately upon issuance of the license at the end of the licensing process for the transaction, provided that you have disclosed complete and accurate details of your proposed use, no license is finally effective unless and until full payment is received from you (either by publisher or by CCC) as provided in CCC's Billing and Payment terms and conditions. If full payment is not received on a timely basis, then any license preliminarily granted shall be deemed automatically revoked and shall be void as if never granted. Further, in the event that you breach any of these terms and conditions or any of CCC's Billing and Payment terms and conditions, the license is automatically revoked and shall be void as if never

granted. Use of materials as described in a revoked license, as well as any use of the materials beyond the scope of an unrevoked license, may constitute copyright infringement and publisher reserves the right to take any and all action to protect its copyright in the materials.
9. Warranties: Publisher makes no representations or warranties with respect to the licensed material.
10. Indemnity: You hereby indemnify and agree to hold harmless publisher and CCC, and their respective officers, directors, employees and agents, from and against any and all claims arising out of your use of the licensed material other than as specifically authorized pursuant to this license.
11. No Transfer of License: This license is personal to you and may not be sublicensed, assigned, or transferred by you to any other person without publisher's written permission.
12. No Amendment Except in Writing: This license may not be amended except in a writing signed by both parties (or, in the case of publisher, by CCC on publisher's behalf).
13. Objection to Contrary Terms: Publisher hereby objects to any terms contained in any purchase order, acknowledgment, check endorsement or other writing prepared by you, which terms are inconsistent with these terms and conditions or CCC's Billing and Payment terms and conditions. These terms and conditions, together with CCC's Billing and Payment terms and conditions (which are incorporated herein), comprise the entire agreement between you and publisher (and CCC) concerning this licensing transaction. In the event of any conflict between your obligations established by these terms and conditions and those established by CCC's Billing and Payment terms and conditions, these terms and conditions shall control.
14. Revocation: Elsevier or Copyright Clearance Center may deny the permissions described in this License at their sole discretion, for any reason or no reason, with a full refund payable to you. Notice of such denial will be made using the contact information provided by you. Failure to receive such notice will not alter or invalidate the denial. In no event will Elsevier or Copyright Clearance Center be responsible or liable for any costs, expenses or damage incurred by you as a result of a denial of your permission request, other than a refund of the amount(s) paid by you to Elsevier and/or Copyright Clearance Center for denied permissions.

LIMITED LICENSE

The following terms and conditions apply only to specific license types:
15. **Translation**: This permission is granted for non-exclusive world **English** rights only unless your license was granted for translation rights. If you licensed translation rights you may only translate this content into the languages you requested. A professional translator must perform all translations and reproduce the content word for word preserving the integrity of the article.
16. **Posting licensed content on any Website**: The following terms and conditions apply as follows: Licensing material from an Elsevier journal: All content posted to the web site must maintain the copyright information line on the bottom of each image; A hyper-text must be included to the Homepage of the journal from which you are licensing at http://www.sciencedirect.com/science/journal/xxxxx or the Elsevier homepage for books at http://www.elsevier.com; Central Storage: This license does not include permission for a scanned version of the material to be stored in a central repository such as that provided by Heron/XanEdu.
Licensing material from an Elsevier book: A hyper-text link must be included to the Elsevier

homepage at http://www.elsevier.com . All content posted to the web site must maintain the copyright information line on the bottom of each image.

Posting licensed content on Electronic reserve: In addition to the above the following clauses are applicable: The web site must be password-protected and made available only to bona fide students registered on a relevant course. This permission is granted for 1 year only. You may obtain a new license for future website posting.
17. **For journal authors:** the following clauses are applicable in addition to the above:
Preprints:
A preprint is an author's own write-up of research results and analysis, it has not been peer-reviewed, nor has it had any other value added to it by a publisher (such as formatting, copyright, technical enhancement etc.).
Authors can share their preprints anywhere at any time. Preprints should not be added to or enhanced in any way in order to appear more like, or to substitute for, the final versions of articles however authors can update their preprints on arXiv or RePEc with their Accepted Author Manuscript (see below).
If accepted for publication, we encourage authors to link from the preprint to their formal publication via its DOI. Millions of researchers have access to the formal publications on ScienceDirect, and so links will help users to find, access, cite and use the best available version. Please note that Cell Press, The Lancet and some society-owned have different preprint policies. Information on these policies is available on the journal homepage.
Accepted Author Manuscripts: An accepted author manuscript is the manuscript of an article that has been accepted for publication and which typically includes author-incorporated changes suggested during submission, peer review and editor-author communications.
Authors can share their accepted author manuscript:

- immediately
    - via their non-commercial person homepage or blog
    - by updating a preprint in arXiv or RePEc with the accepted manuscript
    - via their research institute or institutional repository for internal institutional uses or as part of an invitation-only research collaboration work-group
    - directly by providing copies to their students or to research collaborators for their personal use
    - for private scholarly sharing as part of an invitation-only work group on commercial sites with which Elsevier has an agreement
- After the embargo period
    - via non-commercial hosting platforms such as their institutional repository
    - via commercial sites with which Elsevier has an agreement

In all cases accepted manuscripts should:

- link to the formal publication via its DOI
- bear a CC-BY-NC-ND license - this is easy to do
- if aggregated with other manuscripts, for example in a repository or other site, be shared in alignment with our hosting policy not be added to or enhanced in any way to appear more like, or to substitute for, the published journal article.

Published journal article (JPA): A published journal article (PJA) is the definitive final record of published research that appears or will appear in the journal and embodies all value-adding publishing activities including peer review co-ordination, copy-editing, formatting, (if relevant) pagination and online enrichment.
Policies for sharing publishing journal articles differ for subscription and gold open access articles:
Subscription Articles: If you are an author, please share a link to your article rather than the full-text. Millions of researchers have access to the formal publications on ScienceDirect, and so links will help your users to find, access, cite, and use the best available version. Theses and dissertations which contain embedded PJAs as part of the formal submission can be posted publicly by the awarding institution with DOI links back to the formal publications on ScienceDirect.
If you are affiliated with a library that subscribes to ScienceDirect you have additional private sharing rights for others' research accessed under that agreement. This includes use for classroom teaching and internal training at the institution (including use in course packs and courseware programs), and inclusion of the article for grant funding purposes.
Gold Open Access Articles: May be shared according to the author-selected end-user license and should contain a CrossMark logo, the end user license, and a DOI link to the formal publication on ScienceDirect.
Please refer to Elsevier's posting policy for further information.
18. **For book authors** the following clauses are applicable in addition to the above: Authors are permitted to place a brief summary of their work online only. You are not allowed to download and post the published electronic version of your chapter, nor may you scan the printed edition to create an electronic version. **Posting to a repository:** Authors are permitted to post a summary of their chapter only in their institution's repository.
19. **Thesis/Dissertation**: If your license is for use in a thesis/dissertation your thesis may be submitted to your institution in either print or electronic form. Should your thesis be published commercially, please reapply for permission. These requirements include permission for the Library and Archives of Canada to supply single copies, on demand, of the complete thesis and include permission for Proquest/UMI to supply single copies, on demand, of the complete thesis. Should your thesis be published commercially, please reapply for permission. Theses and dissertations which contain embedded PJAs as part of the formal submission can be posted publicly by the awarding institution with DOI links back to the formal publications on ScienceDirect.

Elsevier Open Access Terms and Conditions
You can publish open access with Elsevier in hundreds of open access journals or in nearly 2000 established subscription journals that support open access publishing. Permitted third party re-use of these open access articles is defined by the author's choice of Creative Commons user license. See our open access license policy for more information.
Terms & Conditions applicable to all Open Access articles published with Elsevier:
Any reuse of the article must not represent the author as endorsing the adaptation of the article nor should the article be modified in such a way as to damage the author's honour or reputation. If any changes have been made, such changes must be clearly indicated.
The author(s) must be appropriately credited and we ask that you include the end user license and a DOI link to the formal publication on ScienceDirect.
If any part of the material to be used (for example, figures) has appeared in our publication